Politecnico di Torino

Corso di Laurea Magistrale in Ingegneria Biomedica
A.a. 2022/2023
Sessione di Laurea Marzo 2023

Layer-by-Layer nanotheranostics loading docetaxel and enzalutamide with improved targeting, imaging and therapeutic effects for prostate cancer

Supervisors:
Prof.ssa Chiara Tonda Turo
Dr. Irene Carmagnola
Prof. Piergiorgio Gentile

Candidate:
Botrugno Veronique Maria
s282755

DECLARATION OF WORK

I declare that this thesis is based on my own work and has not been submitted in any form or for any other degree at this university. Except where otherwise noted in the text or the acknowledgements below, this is the sole work of Veronique Maria Botrugno. I am aware of the penalties for plagiarism, fabrication, and unacknowledged syndication, and declare that this report is free of these

ACKNOWLEDGEMENTS

I would like to express my sincere gratitude to my supervisor Piergiorgio Gentile for his guidance, support, and mentorship. His willingness to go above and beyond to help me achieve my goals was inspiring. I am grateful for the time and energy he invested in me and the lessons I learned under his tutelage. Thank you for helping me achieve this milestone.

TABLE OF CONTENTS

LIST OF FIGURES

LIST OF TABLES

ABSTRACT

Prostate cancer (PCa) is the most common malignant tumor in men and, after lung cancer, the second leading cause of cancer death. Over 1.4 million new PCa cases were diagnosed worldwide in 2020. When the disease progresses to an advanced stage, invasion and metastasis increase mortality. Currently, androgen deprivation therapy (ADT) has become the standard of care for men with locally advanced or metastatic prostate cancer. However, after undergoing ADT for 18 to 24 months, most patients develop castration-resistant prostate cancer (CRPC). Depending on the stage of CRPC, the recommended first-line treatment regimens include chemotherapy with docetaxel (DTX) and novel hormonal agents, such as enzalutamide (ENZ). Combination therapy with DTX and ENZ for CRPC is expected to be successful in the future. To achieve this goal, it is critical to design a drug delivery system with distinct pharmacokinetic actions for both drugs.

Owing to advances in materials science, nanoparticle (NP) technology is a proved strategy for developing an efficient a cancer treatment regimen. Indeed, NPs can safely and efficiently deliver drugs to specific locations, resulting in greater benefits at lower dosages. The wide range of currently available nanomaterials, such as liposomes, polymer NPs, inorganic NPs, allows their selection and adaptation to various types of drugs, providing additional material selection flexibility.

In this thesis, PSMA-targeted, DTX and ENZ co-loaded nanotheranostics for both PCa imaging and therapy were designed and conceptually validated. Particularly, the system's ability to perform bioimaging is related to the use of quantum dots (QDs), that consist in fluorescent probes with unique optical and chemical properties. QDs are an extremely helpful tool for the early detection and diagnosis of PCa and have significantly changed bioimaging, drug research, and diagnostics. The primary issue with the application of QDs in biological applications is their toxicity. In this study, carbon QDs (CQDs) derived from natural sources (chitin) were used to ensure their cytocompatibility. High-resolution transmission electron microscopy (HRTEM), UV-Vis, and fluorescence analyses have been performed to examine the physicochemical and morphological characteristics of the CQDs. The results showed a size of the CQDs between 2 and 10 nm, a positive charge, and an emission peak at 400 nm. Then, the cytotoxicity of CQDs on neo-dermal fibroblasts was evaluated by using Presto Blue and Live/Dead assays. The results showed high cellular viability-up up to a concentration of CQDs 500 μg/mL.

Following that, the nanotheranostic systems were designed and manufactured with a nanocore composed of calcium phosphate (CaP) containing DTX and stabilized by PAH deposition via a pumping method. Using the layer-by-layer assembly technique, successive layers of two oppositely charged natural polysaccharides were deposited on the core of the system via electrostatic interactions. In this study, chitosan (CHI) and furcellaran (FUR) were used as natural polysaccharides for the deposition of four layers.

Three systems have been developed to assess the individual and synergistic effects of DTX and ENZ. The first system was characterized by the presence of DTX in the core, while in the second and third systems, DTX and ENZ were encapsulated into the layers; specifically, in the second one, only ENZ was encapsulated into the layers, whereas in the third system, both DTX and ENZ were encapsulated in the resulting nanocoating. Moreover, prostate-specific membrane antigen (PSMA) is overexpressed on the surfaces of PCa cells. Consequently, the treatment of PCa has made effective use of PSMA as a target antigen for targeted drug delivery. Thus, a small-molecule PSMA ligand (PSMA-617) was grafted on the outermost layer of nanotheranostics to enhance cancer cell-specific targeting, uptake, and retention.

The final system was characterized through chemical-physical and morphological studies. Using Presto Blue and Live/Dead assays the efficacy and cytotoxicity of the proposed treatment were evaluated. In particular, cellular tests were conducted on two different types of prostate cancer cells, LNCap and VCap. The results showed that the concentrations of DTX and ENZ used in various formulations were too low to have a significant cytotoxic effect on cells. Therefore, increasing the concentration of both drugs was required. Furthermore, the presence of polysaccharides in the system resulted in high biocompatibility for both cell lines, but with a greater effect in the case of LNCaps. Finally, 3D models of VCap tumor cells were created to assess the proposed system’s efficacy in the most biomimetic and reliable manner possible.

1 INTRODUCTION

1.1 Prostate gland

1.1.1 Anatomy

The prostate is part of the male reproductive system and includes the penis, prostate, seminal vesicles, and testicles. It is a fibromuscular and glandular organ that lies inferior to the bladder (Fig.1) In an adult man, without significant prostatic hyperplasia, the prostate is shaped as an inverted cone, weighing proximately 30 - 40 g, and it is encapsulated by a fibroelastic tissue layer.

The prostatic urethra, which is approximately 2.5 cm in length, is the portion of the urethra that crosses the prostate. It is lined with the inner longitudinal layer of the muscle. A considerable amount of smooth muscle, most of which is derived from the outer longitudinal muscle of the bladder, is incorporated into the prostate. This musculature constitutes the involuntary smooth muscle sphincter of the posterior urethra of the male. The puboprostatic ligaments support the prostate in the anterior direction, while the diaphragm urogenital supports it in the inferior direction. The ejaculatory ducts penetrate the prostate posteriorly, via the verumontanum on the floor of the prostatic urethra, near the striated external urethral sphincter (Fig.2,3) (McAninch & Lue, 2020).

The main male hormone is testosterone, which is produced in the testicles. The prostate is regulated by dihydrotestosterone, which is synthesized from testosterone in peripheral tissues (“Rajal B. Shah” & “Ming Zhou,” 2019).

1.1.2 Function

The primary job of the prostate is to produce a fluid that, together with secretions from other glands and sperm from the testicles, forms semen. During ejaculation, the semen is forced into the urethra by the muscles of the prostate and then forced forth. The semen is alkaline, which allows for the neutralization of the vaginal tract and allows the sperm to remain viable (https://www.cdc.gov/cancer/prostate/basic_info/what-is-prostate-cancer.htm).

1.1.3 Structure

There are two methods to categorize the prostate: by lobe and by zone.

Lobe classification: The five-lobe categorization, which includes the anterior, posterior, middle, right lateral, and left lateral, is frequently used in cystourethroscopic exams.

Zone classification: McNeal *et al.* (McNeal, 1984) demonstrated that the human prostate is a composite organ composed of three glandular zones and a fourth non-glandular zone, termed the anterior fibromuscular zone. These different zones are tightly fused within a common sheath of fibromuscular tissue, the “capsule”. McNeal further defined the relationship between these zones and the prostatic urethra and specified their locations along the prostatic urethra.

- The *central zone* (CZ) (about 25% of the prostate volume) is an inverted cone surrounding the ejaculatory ducts and forms a part of the prostate base. The incidence of prostate cancer (PCa) in the CZ is only ~ 1-5% (https://www.urologymatch.com/node/2638). Tumors in the central zone tend to be more aggressive than those in other zones (Vargas et al., 2012).
- The *transition zone* (TZ) (about 10% of the prostate volume) surrounds a portion of the urethra between the urinary bladder and the verumontanum. The incidence of PCa in the TZ is approximately 20%. TZ increases steadily with age, and this increase is particularly marked in the presence of benign prostatic hyperplasia (BPH) (Greene, Fitzpatrick, and Scardino 1995).
- The peripheral zone (PZ) (about 70% of the prostate volume) extends posterolaterally around the central zone and the distal prostatic urethra. The incidence of PCa in the PZ is approximately 70%.

The peripheral and central zones are collectively referred to as the *outer prostate*, whereas the transition zone and the anterior fibromuscular layer are collectively referred to as the *inner prostate* (“Rajal B. Shah” & “Ming Zhou,” 2019). This classification is often used in pathology.

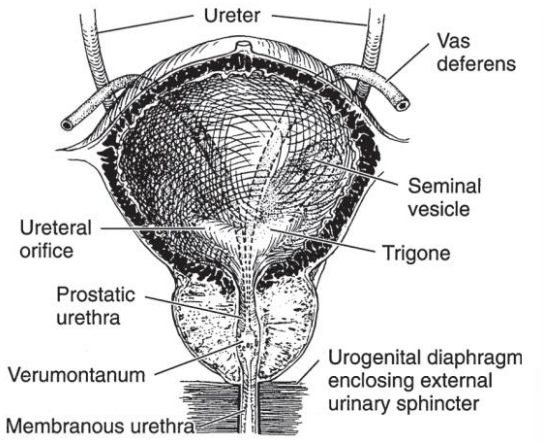

Fig.1: Anatomy and relations between the ureters, bladder, prostate, seminal vesicles, and vasa deferentia (Smith & Tanagho's General Urology, Nineteenth Edition)

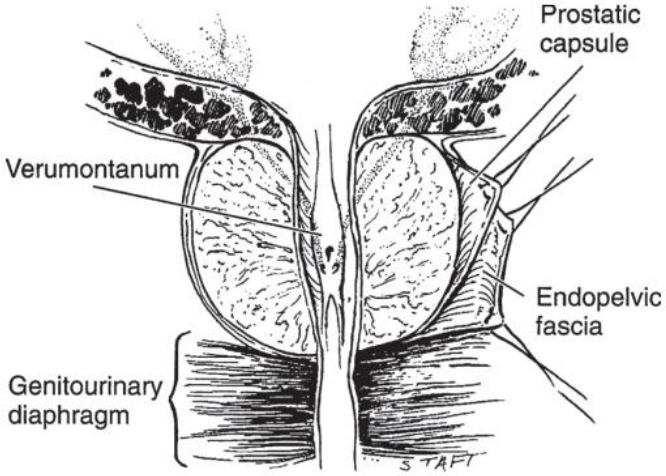

Fig.2: Section of the prostate glandshows the prostatic urethra, veumontanum, and crista urethralis, in addition to the opening of the prostatic utricle and the two ejaculatoy ducts in the midline. (Smith & Tanagho's General Urology, Nineteenth Edition)

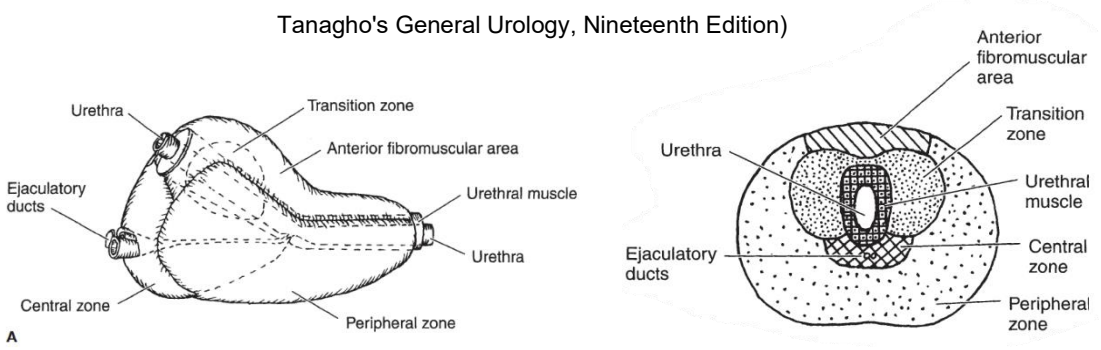

Fig.3: (Left) Schematic transverse view pf the prostate. (Right) Schematic lateral view of the prostate (Smith & Tanagho's General Urology, Nineteenth Edition)

1.2 Prostate cancer (PCa)

1.2.1 PCa epidemiology

PCa is the most common non-cutaneous cancer in America, where more than 174,000 cases are detected annually. Over 31,000 men die of the disease annually, which is the second highest burden among malignancies affecting men (Rawla, 2019). However, age-adjusted PCa mortality at the population level has declined by roughly 50% since the mid–1990s, during a time in which men have been living longer and therefore have been more likely to reach older ages at which prostate cancer mortality would be expected to increase (Taitt, 2018). The explanation is controversial but likely multifactorial, reflecting in large part a combination of early detection programs and improvements in treatment. These improvements in mortality have come at the cost of significant overdiagnosis and overtreatment.

In 2020, more than 1.4 million new PCa cases were diagnosed globally. The crude incidence rate was 36.0 per 100,000 males and the age-standardized incidence rate (ASIR) was 30.7 per 100,00 males. Data by continent showed that ASIRs in Europe, Latin America, the Caribbean, Northern America, and Oceania exceeded 59 per 100,000 males, while ASIRs in Africa and Asia were lower than 30 per 100,000 males. However, the regional distribution of the age-standardized mortality rate (ASMR) (Fig.4,5) was quite different, with the highest rate in Africa, followed by Latin America, the Caribbean, Europe, Oceania, Northern America, and Asia (L. Wang et al., 2022) .

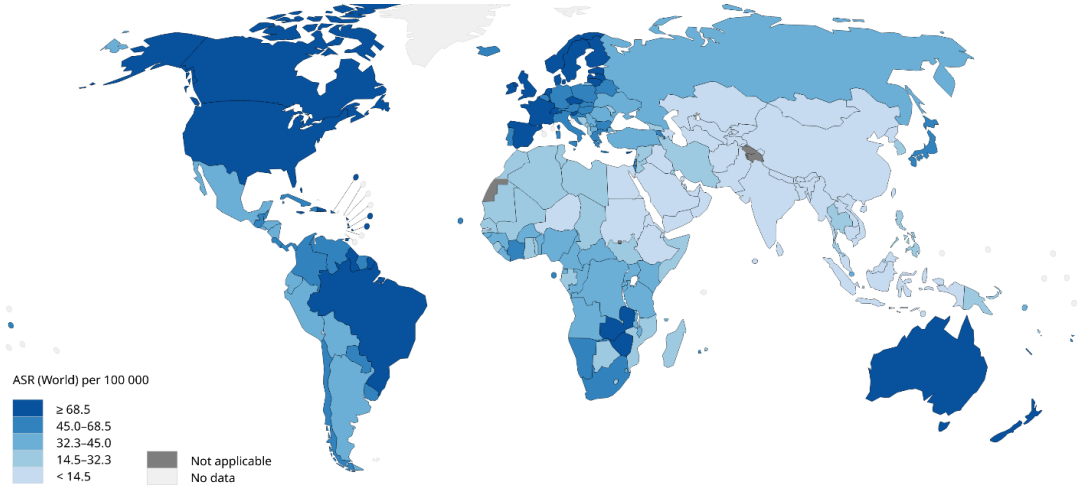

Fig.4: Estimated age-standardized incidence rates (world) in 2020 of prostate cancer in males, all ages (Global Cancer Observatory, https://gco.iarc.fr/).

LeWang et al., with the support of ecological correlation analysis shown in Figure 6, discovered a positive correlation between the incidence of PCa and the Human Development Index (HDI), with ASIRs in nations with a very high HDI being more than twice as high as those in nations with a low HDI, and a negative correlation between the ASMRs of prostate cancer and HDI (Fig. 6)(Wang et al. 2022).

The burden of PCa is expected to increase due to population ageing and economic growth. It is predicted that by 2035, there will be more than 75,000 new cases of PCa annually, making it the most common cancer overall (Fig.7). The increased incidence of PCa is mainly due to the introduction of prostate-specific antigen (PSA) blood tests and the increased use of transurethral resection of the prostate (TURP) as a treatment for benign prostatic hyperplasia (BPH). This has resulted in earlier detection of PCa and in the diagnosis of diseases that may not have become clinically apparent during the patient's lifetime.

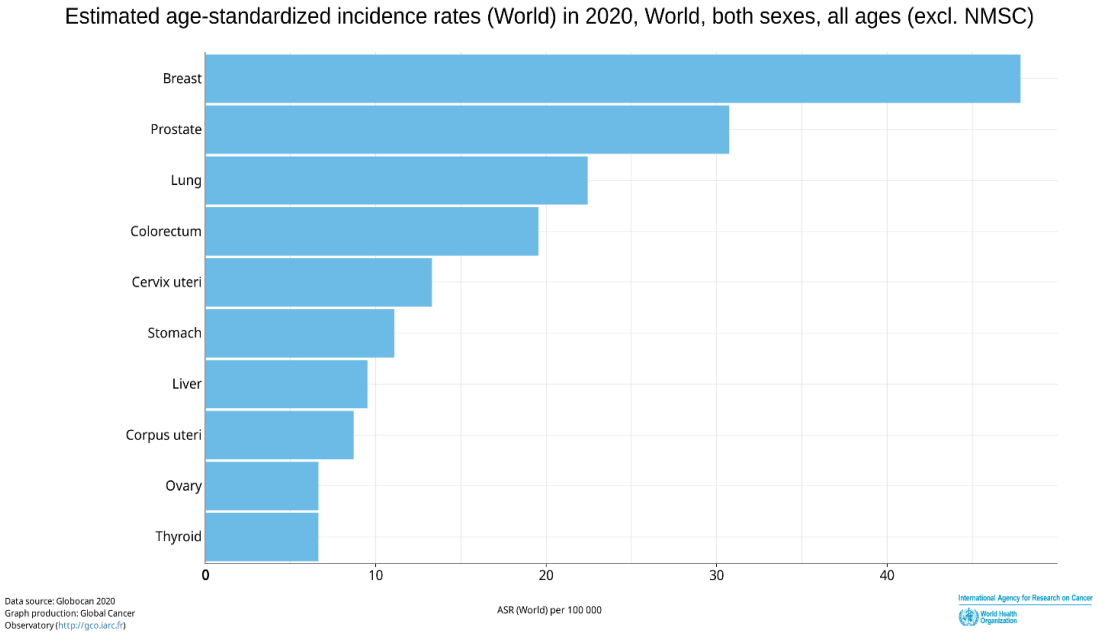

Fig.5: Estimated age-standardized incidence rates (world) in 2020 of different type of cancer in both sexes, all ages (Global Cancer Observatory, https://gco.iarc.fr/).

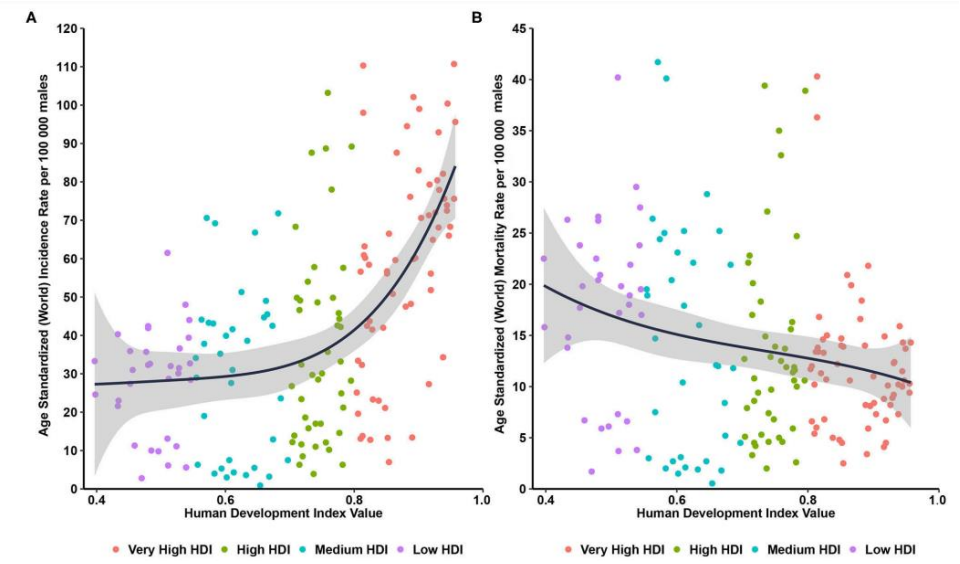

Fig.6: Correlations between age-standardized incidence and mortality of PCa and human development index. (A) Age-standardized incidence rate; (B) Age-standardized mortality rate (Wang et al. 2022).

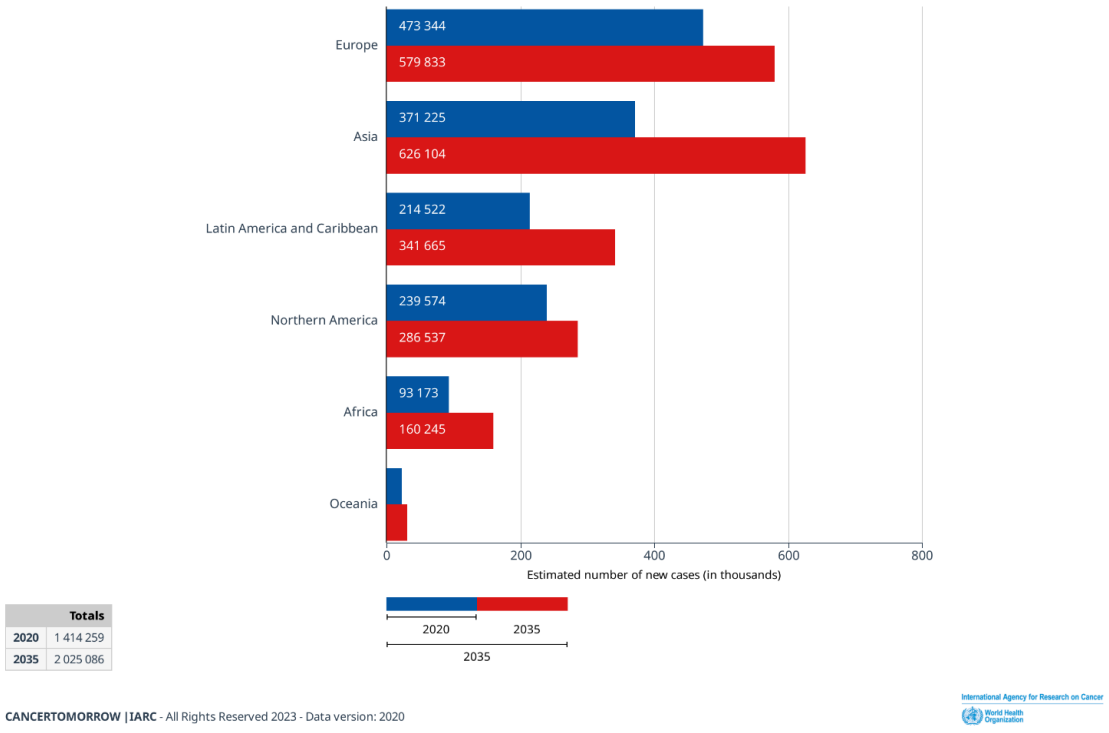

Fig.7: Estimated number of new cases of PCa from 2020 to 2035, males, age [0-85+] (Global Cancer Observatory, https://gco.iarc.fr/).

1.2.2 PCa aetiology

The aetiology of PCa is multifactorial, with numerous modifiable and unmodifiable risk factors associated with its development. Some well-established risk factors include the following:

- *Age*: PCa rates increase faster with age than in many other cancers. The incidence of PCa increases with age. A systematic review of autopsy studies reported a 5% prevalence of PCa at age < 30 years (95% confidence interval [CI]: 3–8%), increasing by an odds ratio (OR) of 1.7 (1.6–1.8) per decade, to a prevalence of 59% (48–71%) by age > 79 years (Bell et al., 2015).
- *Family history and genetic predisposition*: PCa has an increased heritability. Up to 20% of men, who are diagnosed with PCa, have a father or brother who has had the illness. Any affected family member present increases the risk of developing PCa by roughly a factor of two. One first-degree relative who is under 60 years old, at the time of diagnosis, increases PCa risk by 2.5 times (vs 1.6 times for first-degree relatives who are over 60 years old). The relative risk is 5.7

if two or more relatives are under 60 years old, and 3.5 if they were over 60 at the time of the diagnosis.

A hereditary disease, which can be present in up to 10% of cases, is defined by the presence of three or more first-degree relatives PCa diagnosed in three successive generations of the same lineage, or two first-degree relatives both diagnosed with early-onset disease (55 years). Family predisposition and hereditary cancer syndromes linked to PCa have complicated genetic causes. Men with a genetic mutation of HOXB13 had a higher lifetime chance of developing PCa than men without such a mutation. However, other cancer-predisposing genes, such as BRCA1, BRCA2, and the MSH2 gene linked to Lynch syndrome, also influence PCa risk. Additionally, it has been demonstrated that over 200 single nucleotide polymorphisms enhance the chance of developing PCa (Gandaglia et al., 2021).

- *Ethnicity*: The incidence of PCa diagnosis varies widely between different geographical areas, being highest in Australia/New Zealand, the United States, Canada, and Northern and Western Europe, largely due to the use of prostate-specific antigen (PSA) testing and the ageing population. The incidence is low in Eastern and South-Central Asia but is rising. Rates in Eastern and Southern Europe are low but have also shown a steady increase (Gandaglia et al., 2021).

- *Smoking and alcohol consumption:* Among the modifiable risk factors for PCa, smoking has been associated with an increased likelihood of developing the disease. According to a meta-analysis of 24 cohort studies by Huncharek *et al.*, there is no increased risk or incidence of PCa among current smokers, but the risk increased with increasing amount smoked. Additionally, heavy smokers had a 24–30% higher chance of dying from prostate cancer, while ex-smokers had an elevated risk of the disease.

  Previous research on alcohol use and the risk of PCa has not been proven conclusive. In a comprehensive review and meta-analysis of 340 studies, alcohol use and the chance of developing PCa were found to have a substantial dose-response association. A systematic review and meta-analysis of 340 studies noted a significant dose-response relationship between alcohol consumption and PCa risk. Compared to non-drinkers, the risk rises as alcohol intake increases(Lim Ng, 2021).

- *Obesity:* The impact of obesity on PCa is controversial. According to a meta-analysis by Cao and Ma, an increase in BMI of 5 kg/m^2 led to a 20% higher risk of prostate cancer mortality [11]. In addition, dietary lycopene, selenium, omega-3 fatty acids, and vitamin E intake are protective, whereas vitamin D and calcium intake increase risk. However, no dietary supplementation study has yet shown a tangible benefit in terms of reducing the risk of diagnosis or mortality, and some supplements increase the risk of PCa mortality (Kenfield et al., 2014).

1.2.3 PCa pathology

More than 95% of PCa cases are adenocarcinomas arising from the prostatic epithelial cells. The term "prostate adenocarcinoma," when used without qualification, does refer to the acinar variant of the neoplasm, which represents more than 95% of PCa, so named because it derives from the prostatic acini (McAninch & Lue, 2020).

The histology of the remaining 5% of PCa cases is heterogeneous, arising from stromal, epithelial, or ectopic cells. According to their cellular origin, non-adenocarcinoma variations can be divided into two groups: epithelial and non-epithelial. Some examples of non-adenocarcinoma variations include the following:

- *ductal adenocarcinoma*, which arises from the prostatic duct epithelium and can be sieve, papillary, or solid, does not always impact PSA levels, making it potentially more difficult to detect. In addition, ductal adenocarcinomas spread faster than acinar adenocarcinomas (https://www.cancerresearchuk.org/about-cancer/prostate-cancer/stages; Baig et al., 2015; http://www.cancerresearchuk.org/about-cancer/soft-tissue-sarcoma/about; https://prostatecanceruk.org/prostate-information/further-help/rare-prostate-cancer);

- *transitional cell carcinoma*, which arises from the cells lining the urethra or bladder, is also known as urothelial cancer. PCa can develop when the primary tumor breaks off and spreads locally. Rarely, this type of cancer can begin in the prostate and then spread to the bladder (https://www.crs-src.ca/page.aspx?pid=1801;https://www.cancerresearchuk.org/about-

cancer/prostate-cancer/stages;http://www.cancerresearchuk.org/about-cancer/soft-tissue-sarcoma/about);

- *squamous cell carcinoma* develops from flat cells that cover the prostate. This type of tumor is very aggressive; the cells tend to grow and spread more quickly than adenocarcinomas of the prostate. (https://www.crs-src.ca/page.aspx?pid=1801;https://www.cancerresearchuk.org/about-cancer/prostate-cancer/stages;http://www.cancerresearchuk.org/about-cancer/soft-tissue-sarcoma/about);

- *neuroendocrine tumors*, such as carcinoid, paraganglioma, neuroblastoma, and small cell tumor, which represent the most aggressive histotypes, are present in the neuroendocrine system, which is comprised of nerve and gland cells, responsible for producing and releasing hormones into the bloodstream. They grow slowly and most often start in the digestive system before moving to other places, such as the prostate **(**http://www.cancerresearchuk.org/about-cancer/carcinoid/about**)**.

- *neoplasms mesenchymal diseases*, such as sarcomas or lymphomas, are uncommon, accounting for less than 0.1% of all primary prostate cancer cases. These types of tumors develop in soft tissues, such as the muscles and nerves. Since soft tissue can be found all over the body, these cancers can develop and spread anywhere. Although sarcomas can grow in the lymphatic vessels, blood vessels, and smooth muscles of the prostate, the most common location to find them once they break away and spread is the lungs (https://prostatecanceruk.org/prostate-information/further-help/rare-prostate-cancer. http://www.cancerresearchuk.org/about-cancer/soft-tissue-sarcoma/about;https://www.crs-src.ca/page.aspx?pid=1801)

1.2.4 Precursor of PCa

Prostatic intraepithelial neoplasia (PIN) is thought to be a possible precursor lesion of PCa. It is a multicentric condition defined as the “neoplastic growth of epithelial cells within pre-existing benign prostatic acini or ducts”; it consists of an inversion of the normal orientation of epithelial proliferation from the basal cell compartment to the luminal surface. Four main patterns of PIN have been described: tufting, micropapillary,

cribriform, and flat. There are no known clinically important differences between these architectural patterns, and their recognition appears to be only of diagnostic utility.

PIN can be divided into two grades, low (LGPIN) and high (HGPIN). HGPIN is characterized by cellular proliferation within preexisting ducts and glands, with nuclear and nucleolar enlargement similar to PCa. Multiple studies have found HGPIN to be a significant predictor of PCa (22-58%) (Murray, 2021)

In addition to PIN, several different histological lesions have been proposed as potential precursors of PCa, such as adenosis (atypical adenomatous hyperplasia, AAH) and proliferative inflammatory atrophy (PIA). Adenosis may be a potential precursor to carcinomas arising in the TZ, lesions that are often low-grade and not thought to possess strong malignant potential. PIA, consisting of simple atrophy and post-atrophic hyperplasia, is often associated with inflammation, and it has been observed to merge directly with small adenocarcinoma lesions in the PZ, but this seems to be relatively uncommon. If PIA is a precursor (or "risk factor lesion") for PCa, it may do so indirectly by progressing to carcinoma via PIN, as PIA merging with PIN is extremely common (Fig.8) (De Marzo et al., 2016).

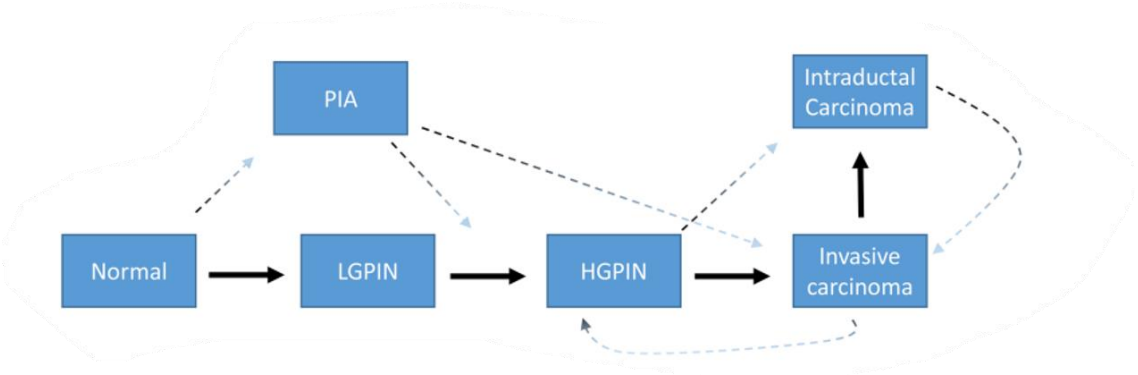

Fig.8: Model of progression from normal to low-grade PIN (LGPIN) to high-grade (HGPIN) to carcinoma (De Marzo et al., 2016).

1.2.5 Clinical strategies for PCa diagnosis

A. Prostate-Specific Antigen (PSA)

Traditionally, diagnosis is made by monitoring PSA levels. PSA is a serine protease in the human kallikrein (HK) family, that may be elevated in a variety of benign and malignant conditions. It circulates in the serum in uncomplexed (free or unbound) or

complexed (bound) forms. It is used as a diagnostic tool, for risk-stratifying known PCa, and for following cancers after treatment.

PSA is *prostate-specific*, not *prostate-cancer-specific*. There may be other conditions characterized by high PSA values, such as BPH and prostatitis, that produce false-positive results. Initially, a PSA level lower than 4ng/ml was considered a “normal” level in men aged 50-70 years, but over time, it has been demonstrated that there is no single “normal” threshold for PSA, as this is a variable dependent on several factors, such as age, prostate size, and the risk of prostate cancer.

Following the TRUS (transrectal ultrasonography) and needle biopsy procedure, patients with an abnormal PSA level (4ng/mL) typically undergo additional digital rectal examination (DRE) to evaluate the texture and size of tumours (McAninch & Lue, 2020).

B. Digital Rectal Examination (DRE)

Due to the unreliability of PSA, urologists must consider additional examinations to determine if the patient has PCa, such as the DRE. DRE can be used to assess prostate volume. It can detect PCa with a volume greater than 0.2 mL if situated in the posterior peripheral zone. However, there is a high degree of inter-observer variability, and a normal DRE does not eliminate the risk of significant PCa. A positive DRE suggests a prostate biopsy (McAninch & Lue, 2020).

C. Prostate Biopsy

A prostate biopsy should be considered for men with an elevated serum PSA, abnormal DRE, or a combination of the two, depending also on the patient’s overall health, comorbidities, life expectancy, levels of anxiety and risk aversion, age, and information preferences. Prostate biopsy is performed under transrectal ultrasonography (TRUS) guidance using a spring-loaded biopsy device coupled to the imaging probe (McAninch & Lue, 2020).

D. *Imaging*

Rapid technological advances over the last few years have allowed the mainstream use of prostate imaging for the clinical management of PCa. Imaging modalities such as multiparametric magnetic resonance imaging (mpMRI), computed tomography (CT), and positron emission tomography (PET) imaging are now being used for all facets of PCa diagnosis and localization, whole-gland and focal therapy, staging, active surveillance,

and recurrence monitoring. The choice of imaging modality depends on the biological behavior of the underlying tumor (Sarkar & Das, 2016).

1.2.5.1 Local staging with mpMRI

Multiparametric MRI (mpMRI) assessment of the prostate has been gaining a lot of popularity lately. This exam includes T2-weighted anatomic imaging that is combined with at least two functional MRI sequences, diffusion-weighted imaging (DWI) and dynamic contrast-enhanced (DCE) imaging, for imaging the different biological characteristics of the tumor. The DWI reflects the increased cell membrane density and resulting drop in water (hydrogen) density of cancer compared to normal tissue, whereas DCE is generally not included in all protocols as it adds time and cost with a relatively low incremental benefit.

Prostate mpMRI interpretation is standardized using the Prostate Imaging Reporting and Data System (PIRADS), under which T2, DWI, and DCE results are summarized in a 1-5 score. PIRADS 1 and 2 exclude high-grade cancer, 3 is indicative of possible high-grade cancer, and 4 and 5 indicate probable high-grade cancer.

Imaging accuracy may be improved by using magnetic resonance spectroscopy (MRS) in addition to magnetic resonance imaging (MRI). In comparison to BPH or normal prostate tissue, PCa is associated with proportionately lower levels of citrate and higher amounts of choline and creatine. A multiparametric MRI exam and MRS's combined metabolic and anatomic data may provide a more precise evaluation of the presence and stage of cancer (McAninch & Lue, 2020; Sarkar & Das, 2016).

1.2.5.2 Systemic assessment of PCA with cross-sectional conventional imaging (CT and MRI)

The incidence of metastatic disease is extremely rare in low-risk diseases (stages T1-T2, serum PSA < 10ng/mL and Gleason score < 7); therefore, metastatic imaging work-up can be avoided for these patients. For patients with intermediate (PSA 10-20ng/mL or Gleason score 7) or high-risk disease (PSA >20ng/mL or Gleason score >7) the risk of nodal or bone involvement can range between 3% and 10% and 20% and 40%, respectively, and a systematic assessment is required before treatment.

Cross-sectional imaging of the pelvis is performed in intermediate- and high-risk patients to exclude lymph node metastases. For this purpose, both CT and body-coil-based MRI are used.

At cross-sectional imaging, nodal assessment is based on size and morphological criteria. Other criteria frequently used are the loss of nodal hilum fat and the clustering and enhancement characteristics. However, conventional imaging techniques are not accurate enough to distinguish hyperplastic benign nodes from malignant nodes or to identify nodal micrometastases. Hovels *et al.* discovered that CT scans have a sensitivity of 42% and a specificity of 82% in a meta-analysis. The poor performance of CT for the detection of nodal metastases has been confirmed in other recent studies MRI, on the other hand, is more sensitive than CT because it detects small metastases in the bone marrow (where metastases begin) before remodelling (Sarkar & Das, 2016).

1.2.5.3 Staging of PCa with molecular imaging

PET involves the imaging of radiolabeled tracers inside the prostate after intravenous administration using gamma cameras. These tracers have been evaluated in various clinical settings, including use at the time of initial diagnosis, as part of active surveillance, and during the workup, for potential metastatic disease to determine the optimal timing of usage. PET imaging highlights the metabolic, molecular, or cellular activity of prostate cells and is used in conjunction with anatomical imaging in the form of PET/MRI or PET/CT. Different methods of PET imaging are characterized by the choice of the tracer and the targeted biological process, e.g, metabolism, cellular proliferation, and receptor binding (Schiavina et al., 2019).

18F-fluorodeoxyglucose (18-FDG). The most common radiotracer used to monitor glucose metabolism in tumor cells is 18-FDG. However, it is not currently used in clinical practice for PCa, and it will remain marginal in the future because of the relatively weak glucose metabolism in small, growing PCa cells and the proximity of the prostate to the urinary bladder, which confounds the uptake readings. The weak glucose metabolism results in a low uptake level of the radiotracer in tumor cells, with significant overlap with normal tissue and BPH. Moreover, conditions such as prostatitis may even demonstrate higher FDG uptake than PCa cells (Sarkar & Das, 2016).

1-Amino-3-fluorine-18-fluorocyclobutane-1-carboxylic acid (18-F ACBC). The 18-F ACBC is an L-leucine analogue that has recently been applied in PCa imaging, which exploits the fact that amino acid transport is upregulated in PCa cells. The advantages of using this tracer on a large scale are yet to be fully shown, and the contemporaneous development of other tracers might limit its use in the future.

11C-Choline (C-11) and 18F-fluorocholine (F-18). Prostate cancer cells are found to preferentially concentrate phosphocholine compared to normal prostate cells. Utilizing this knowledge, radiotracers bound to C-11 and F-18 can localize metastatic lesions.

11C-acetate. Similarly, cancer cells have an increased cellular membrane lipid requirement, and acetate remains the single carbon source used by cancer cells for fatty acid and cholesterol production.

Prostate-specific membrane antigen (PSMA). PSMA is a glutamate carboxypeptidase II with an extensive extracellular domain, a transmembrane segment, and an intracellular domain. PSMA is normally expressed in epithelial cells within the prostate and is strongly upregulated by all stages of PCa. An increase in PSMA expression is normally associated with tumor aggressiveness, metastasis, and disease recurrence, thus providing a rational target for ligand-receptor-based imaging and therapy.

A PSMA small-molecule ligand is radiolabeled with ^{68}Ga and used as a radiotracer to identify potential foci of nodal disease. In addition to GA-based tracers, other PSMA-based radiotracers include ^{64}Cu-labeled aptamers and ^{11}C-, ^{18}F and ^{86}Y- labelled low-molecular-weight inhibitors of PSMA.

1.2.6 PCa grades and stages

To determine the best treatment option for PCa, it is important to determine the extent of PCa. Staging is a way of describing where cancer is located, whether or where it has spread, and whether it affects other parts of the body. There are two types of PCa staging.

- *Clinical staging*. It is based on the results of the DRE, PSA values, biopsy findings, and imaging study results.

- *Pathologic staging*. It is determined following prostatectomy and depends on factors such as tumor burden, the status of surgical margins, extracapsular disease, and seminal vesicle and pelvic lymph node involvement. Pathological staging is a more accurate measure of the extent of disease and allows for better prediction of outcomes.

The most widely used staging system to describe the stage of PCa is the AJCC (American Committee on Cancer) TNM system, which was most recently updated in 2018. TNM refers to the tumor (T), node (N), and metastasis (M) to address the size and

location of the tumor (T), spreading of the tumor to lymph nodes (N), and metastasis to other parts of the body (M). The results were combined to determine the cancer stage for each individual. Five stages are used to assess the extent of cancer, in which 0 refers to no cancer and stages 1 to 4 describe the extent of cancer progression. The TNM classification for PCa is provided in Table 1(Mohler et al., 2019).

Table 5: TNM staging system for PCa (**McAninch & Lue, 2020)**.

T—Primary tumor	
Tx	Cannot be assessed
T0	No evidence of primary tumor
Tis	Carcinoma in situ (PIN)
T1a	≤5% of tissue in resection for benign disease has cancer, normal DRE
T1b	>5% of tissue in resection for benign disease has cancer, normal DRE
T1c	Detected from elevated PSA alone, normal DRE and imaging
T2a	Tumor palpable by DRE or visible by imaging, involving less than half of one lobe of the prostate
T2b	Tumor palpable by DRE or visible by imaging, involving more than half of one lobe of the prostate
T2c	Tumor palpable by DRE or visible by imaging, involving both lobes of the prostate
T3a	Extracapsular extension on one or both sides
T3b	Seminal vesicle involvement on one or both sides
T4	Tumor directly extends into bladder neck, sphincter, rectum, levator muscles, or into pelvic sidewall
N—Regional lymph nodes (obturator, internal iliac, external iliac, presacral lymph nodes)	
Nx	Cannot be assessed
N0	No regional lymph node metastasis
N1	Metastasis in a regional lymph node or nodes
M—Distant metastasis	
Mx	Cannot be assessed
M0	No distant metastasis
M1a	Distant metastasis in nonregional lymph nodes
M1b	Distant metastasis to bone
M1c	Distant metastasis to other sites

DRE, digital rectal examination; PIN, prostatic intraepithelial neoplasia; PSA, prostate-specific antigen; TRUS, transrectal ultrasound.

Used with the permission of the American College of Surgeons. Amin MB, Edge SB, Greene FL, et al. (Eds.) *AJCC Cancer Staging Manual*, 8th Ed. Springer New York, 2017.

Until recently, the Gleason scoring system (Fig.9) was the most common PCa grading system; the system relies on the low-magnification appearance of the glandular architecture under the microscope. In determining the grade of a given tumor, the pathologist looks at how the cancer cells are arranged in the prostate and assigns a score on a scale of 1 to 5 based on the two predominant patterns. The two grades are then added to determine the Gleason score or Gleason sum. Cancer cells that look similar to healthy cells receive a low score, whereas cancer cells that look less like healthy cells or look more aggressive receive a higher score.

A Gleason score of 6 or lower indicates that cells are well differentiated and do not have a pathological appearance compared to healthy cells, while a Gleason score of 8, 9, or 10 indicates that cells are poorly differentiated or undifferentiated and have an abnormal appearance compared to healthy cells. It has currently adopted a Gleason grouping system, which simplifies the groups as follows: Gleason Group 1 = Former Gleason 3 +3 or lower; Gleason Group 2 = Former Gleason 3 + 4; Gleason Group 3 = Former Gleason 4 + 3; Gleason Group 4 = Former Gleason 8; Gleason Group 5 = Former Gleason 9-10 (McAninch & Lue, 2020; Schatten, 2018);

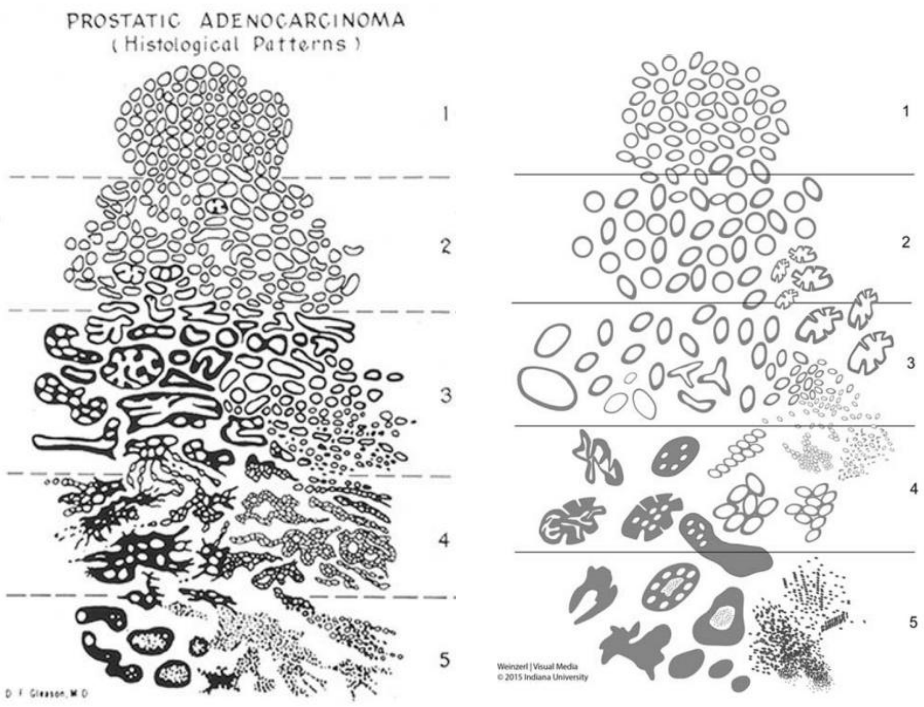

Fig. 9: (Left) Original Gleason schematic grading diagram. (Right) Current modifies schematic Gleason diagram (Epstein, J. I. (2018). Prostate cancer grading: a decade after the 2005 modified system. Modern Pathology, 31(1), 47-63).

1.2.7 Treatments

1.2.7.1 General consideration

It is currently impossible to identify the optimal therapeutic strategy for all the different stages of PCa. The choice of the type of treatment to follow is based on the tumor's risk, the patient's life expectancy, the ability of each therapy to guarantee survival without disease and its associated morbidity, and patient and physician preferences.

After several trials and studies conducted on men with PCa, what is certain is that many men with low-risk disease are candidates for active surveillance; those with low- to intermediate- risk disease should receive local monotherapy (surgery or radiation), and those with higher- risk often need multimodal therapy, either radiation with hormonal therapy or surgery followed selectively by radiation, depending on the pathology and early PSA outcomes(McAninch & Lue, 2020).

1.2.7.2 Localised PCa

When cancer is located only within the prostate and has not yet spread to other organs in the body, it is termed "localized" or "organ-confined" PCa.

Treatments may never be required for low-risk cancers of this type, and only careful observation may be appropriate. Some men will have clinically significant localized PCa, which, if left untreated, could progress to be locally advanced or metastasize. For these men, treatments aimed at cures are recommended. Table 2 illustrates the current risk stratification of localised PCa suggested by the National Institute for Health and Care Excellence (NICE) (McAninch & Lue, 2020).

Table 6: Prostate cancer risk stratification, adapted from NICE (https://www.nice.org.uk/guidance/ng131)

	PSA	Gleason score	Clinical stage
Low risk*	<10ng/ml	6	T1–T2a
Intermediate risk**	10–20ng/ml	7	T2b/c
High risk**	>20ng/ml	8–10	T3/4
* All of; ** One of; PSA = prostate-specific antigen			

1.2.7.3 Watchful waiting and active surveillance

For low-risk patients, watchful waiting (WW) and active surveillance (AS) are increasingly used alternatives to definitive radiation therapy or radical prostatectomy, and national guidelines began advocating their use in 2010.

WW denotes no or minimal monitoring for PCa. It indicates a less intense type of follow-up, that requires fewer tests and relies more on changes in the patient's symptoms to decide whether treatment is needed. WW's goal is to control the symptoms of cancer, but not cure it. If men on WW experience significant progression, androgen deprivation therapy (ADT) is usually initiated. This treatment is most commonly used in elderly men and co-morbid men with a life expectancy of 10 years or less, as well as men who refuse to undergo treatments.

AS is a more contemporary strategy for PCa and is quite different from WW in several different ways. Men on AS with very well-characterized, early-stage, and low- to intermediate-grade cancer are monitored regularly with PSA tests, DRE, and core biopsies to only proceed with treatment if tests show that the PCa is growing rapidly in size, and progressing risk status. Unlikely WW, AS is part of a curative treatment strategy aimed at curing. Table 3 depicts the current NICE-recommended AS protocol. Although AS is likely to produce a very modest decline in PCa-specific survival among men diagnosed with low-risk PCa but could lead to significant benefits in terms of quality of life.

Table 7: Active surveillance schedule from NICE (https://www.nice.org.uk/guidance/ng131)

Timing	Tests[a]
Year 1 of active surveillance	• Every 3 to 4 months: measure prostate-specific antigen (PSA)[b] • Throughout active surveillance: monitor PSA kinetics[c] • At 12 months: digital rectal examination (DRE)[d] • At 12 to 18 months: multiparametric MRI
Year 2 and every year thereafter until active surveillance ends	• Every 6 months: measure PSA[b] • Throughout active surveillance: monitor PSA kinetics[c] • Every 12 months: DRE[d]
[a] If there is concern about clinical or PSA changes at any time during active surveillance, reassess with multiparametric MRI and/or re-biopsy [b] Could be carried out in primary care if there are agreed shared-care protocols and recall systems [c] Could include PSA density and velocity [d] Should be performed by a healthcare professional with expertise and confidence in performing DRE. In a large UK trial that informed this protocol, DREs were carried out by a urologist or a nurse specialist	

1.2.7.4 Active treatment

While WW and AS are the ideal treatments for men with low-risk PCa, there are several additional options for localized illnesses.

1.2.7.4.1 Surgery

Radical prostatectomy (RP) is a surgical procedure to remove the entire prostate gland and seminal vesicles. RP's goal is to completely remove the tumor and avoid surgical morbidity, for example, urinary incontinence and decreased sexual function. Initially described using a perineal approach, the procedure was later popularized using a retropubic one. The open surgical method has now been supplanted by the minimally invasive robot-assisted method, which may offer the advantage of a lower risk of transfusion and a shorter re-convalescence.

After a successful RP, the patient's PSA should be undetectable (< 0.1 ng/mL) within six to eight weeks. Patients who have undergone surgery should have regular PSA tests (McAninch & Lue, 2020; Vernooij et al., 2020; Ridgway & Aning, 2021)

The long-term specific survival rates of PCa following RP, especially when performed by experienced surgeons, are excellent. In a study conducted by Gerald W. Hull *et al.* on 1000 patients (median age: 62.9 years) with localized PCa, the probability of dying of cancer at 10 years postoperatively is 2.4%, and the probability of developing distant metastases is 15.8%, while the probability of remaining free of evidence of cancer progression at 5 and 10 years is 78 and 75%, respectively(Hull et al., 2002).

1.2.7.4.2 Radiotherapy

External beam radiotherapy, brachytherapy, and high-dose brachytherapy are methods of delivering radiation to the prostate. These techniques are aimed at curing PCa without removing the prostate gland. Several investigations have shown that the results of radiotherapy may be improved with the use of androgen deprivation therapy (ADT). Patients undergoing radiotherapy may experience side effects, especially those related to urinary, bowel, and erectile dysfunction. The sexual effects of radiotherapy combined with ADT may be exacerbated, especially if used long-term. In addition, there is a doubled risk of rectal and bladder cancer starting 10 years after prostate radiation, even though the absolute risk of these uncommon cancers remains low (Bhojani et al., 2010).

After radiotherapy, the patient's PSA may fall more slowly, taking up to three years to reach its clinically significant nadir of <0.5 ng/mL. A rise of > 2ng/mL from the nadir is the currently accepted definition of radiation failure.

It should be noted, however, that the majority of men with the low-risk disease should be managed with active surveillance rather than radiation or surgery . To date, surgery and radiotherapy remain the first line of defence against localized PCa (Figure 11).

1.2.7.4.3 Cryotherapy

Cryotherapy is a procedure where freezing of the prostate is carried out by using a multiprobe cryosurgical device. As temperatures reach extreme lows, several events occur, resulting in cancer cell death (McAninch & Lue, 2020; Ridgway & Aning, 2021).

Typically, cryotherapy is used in patients with relapsed cancer or those with low-risk PCa who cannot have surgery or RT. It is frequently effective for men with biopsy-confirmed, locally persistent disease after RT. Side effects of cryotherapy tend to be worse in patients who have already had RT compared to those who have it as their first form of treatment. Most patients experience erectile dysfunction and urinary incontinence, while less than 1% of them develop rectourethral fistulas between the rectum and bladder. The last case represents a severe complication that often requires surgery to be resolved (https://www.cancer.org/cancer/prostate-cancer/treating/cryosurgery.html**;** McAninch & Lue, 2020).

1.2.7.5 Metastatic PCa

When PCa has spread from the prostate to other parts of the body, it is termed “metastatic” PCa. In this case, the treatment of PCa is not aimed at curing the disease. A systematic approach to treatment is adopted to control cancer for as long as possible.

Most PCa are initially androgen-dependent, and the majority of men with metastatic PCa respond initially to various forms of androgen deprivation.

The androgen receptor (AR) signalling axis (Fig.10) is critical for normal prostatic development and maintenance and is the major driver of PCa growth and disease progression. The most abundant circulating androgen is testosterone, which is produced by Leydig cells in the testes (95%), while a smaller amount (5%) is produced by peripheral conversion of other steroids. Free testosterone enters the prostate cells, where it is converted to dihydrotestosterone (DHT), the major intracellular androgen. DHT binds to the AR in the cytoplasm of prostate cells, and the complex moves into the nucleus, where it regulates transcription. Ligan-activated AR binds to specific DNA sequences termed AR response elements (AREs) in the regulatory regions of targeted genes, resulting in transcriptional activation or, less commonly, repression. In malignant

prostate cells, an aberrant AR transcriptional programme promotes cell proliferation and survival.

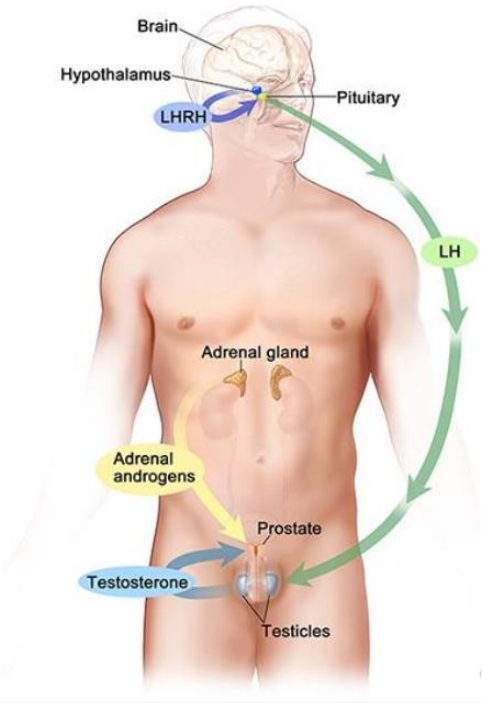

Fig. 10: Androgen receptor (AR) signalling axis.

Hormone therapies work by blocking the production or use of androgens to prevent the growth of such PCa. Currently available treatments can achieve this in several ways:

I. *Reducing androgen production by the testicles:* these are the most commonly used hormone therapies for PCa and the first type of hormone therapy that most men with PCa receive. This form of hormone therapy is known as androgen-deprivation therapy (ADT) and includes:

- Orchiectomy, a surgical procedure to remove one or both testicles. In this way, it is possible to reduce testosterone levels in the blood by 90 to 95%.

- Luteinizing hormone-releasing hormone (LHRH) agonists. These are a class of drugs that prevent the pituitary gland from secreting a hormone called luteinizing hormone (LH). Normally, when testosterone levels in the body are low, the hypothalamus releases LHRH. This stimulates the pituitary gland to produce LH, which in turn stimulates the testicles to produce testosterone. LHRH agonists, like the body's own LHRH, initially stimulate the production

of LH, but the continued presence of high levels of LHRH agonists causes the pituitary gland to stop producing LH. As a consequence, the testicles are not stimulated to produce testosterone (https://www.cancer.gov/types/prostate/prostate-hormone-therapy-fact-sheet#:~:text=LHRH%20agonists%2C%20like%20the%20body's,not%20stimulated%20to%20produce%20androgens).

- Patients undergoing this therapy can experience a phenomenon called “testosterone flare”, which consists of an initial increased level of testosterone, which then decreases rapidly, resulting in medical or chemical castration. However, even after an unlikely surgical castration (orchiectomy), the effects are reversible. There are four LHRH agonists currently approved by the FDA for the treatment of PCa: goserelin acetate (Zoladex), triptorelin pamoate (Trelstar), histrelin acetate (Vantas), and leuprolide acetate (Lupron). Among the most frequent side effects are hot flashes, anaemia, loss of libido and sexual function, loss of bone mineral density, increased weight and body fat, and cognitive changes (https://www.cancer.org/cancer/prostate-cancer/treating/cryosurgery.html**;** McAninch & Lue, 2020).

- LHRH antagonists, which are another form of medical castration. LHRH antagonists (also known as GnHR agonists) do not allow LHRH to bind to its receptors in the pituitary gland. This prevents LH from being secreted and will block the testicles from producing testosterone.

II. *Blocking the action of androgens throughout the body:* this hormone therapy is known as antiandrogen therapy. Such treatments include androgen receptor blockers, which are drugs that compete with androgens for binding to the AR.

III. *Blocking androgen production (synthesis) throughout the body:* including the androgen synthesis inhibitors, which are drugs that prevent the production of androgens by all tissues that produce them.

1.2.7.6 Castration-Resistant PCa (CRPC)

Despite a good initial response to hormone therapies, especially ADT, remission lasts on average 2-3 years, with eventual progression occurring despite castration. At this point, PCa will progress to a castration-insensitive phase of the disease (Castration-Resistant Prostate Cancer, CRPC), which involves a worsening of the prognosis and a life expectancy of 16-18 months, on average, from the beginning of the progression. Conventional treatments may be an option for treating these patients. However, for example, chemotherapy is often not well tolerated by all CRPC patients, who are often elderly men with limited bone marrow reserve and concurrent medical conditions.

The current palliative treatment options for patients with CRPC can be divided into different groups, such as:

1. Hormonal therapy: the AR pathway is often found to be activated in CRPC; consequently, it remains a target of therapeutic strategies to block tumor growth. All of the new treatments for CRPC are used in combination with ADT or surgical castration to keep testosterone levels low, as an increase could lead to tumor progression in some men (McAninch & Lue, 2020; https://www.cancer.gov/types/prostate/prostate-hormone-therapy-fact sheet#:~:text=LHRH%20agonists%2C%20like%20the%20body's,not%20stimulated%20to%20produce%20androgens).

   Hormonal therapies include:

   a. Suppression of androgen biosynthesis. One of the drugs approved by the FDA for this purpose is abiraterone acetate, a prodrug of abiraterone, which is a potent and highly selective inhibitor of androgen biosynthesis that blocks cytochrome P450 c17 (CYP 17), an important enzyme in the synthesis of testosterone. Thus, it prevents the synthesis of androgens in the adrenal glands and within prostate tumors. Abiraterone was approved by the European Medicines Agency (EMA) and the Food and Drug Administration (FDA) for the treatment of men with CRPC after docetaxel chemotherapy in 2011 and men with CRPC without previous chemotherapy in 2013 (Amaral et al., 2012).

b. AR blockade. It involves the use of second-generation antiandrogens that noncompetitively bind the AR and prevent its nuclear translocation. Enzalutamide is a nonsteroidal AR capable of inhibiting the AR pathway in three ways: it binds to the receptor, reduces the efficiency of nuclear translocation of AR, and prevents DNA binding to AREs and recruitment of coactivators(Nuhn et al., 2019).

2. Chemotherapy agents: Docetaxel is the only approved chemotherapy that has been shown to improve overall survival among men with CRPC, as demonstrated in two independent phases III trials reported in 2004 (Galsky & Vogelzang, 2010). It is a taxane-family second-generation chemotherapeutic drug capable of binding to -tubulin with high affinity, disrupting microtubule dynamics, and affecting cytoskeleton functions during mitosis. As a result, the normal progression of the cell cycle is compromised, resulting in G2/M arrest, leading to inhibition of proliferation and cell death (Rizzo, 2021).

3. Immunotherapy: active immune escape strategies protect prostate tumors from detection and destruction by the immune system. Escape mechanisms include immune-suppressive cells, soluble factors, and signalling pathways. Immunotherapeutic approaches, such as Sipuleucel-T, are designed to reactivate or enhance antitumor immunity. Currently, it represents the first and only immunotherapeutic that has shown a survival benefit among men with asymptomatic or minimally symptomatic CRPC. It consists of autologous peripheral blood mononuclear cells (PBMCs), including antigen-presenting cells (APCs), that have been activated ex vivo with a recombinant fusion protein (PA2021) (Nuhn et al., 2019).

4. Bone-targeted therapy: in patients with advanced prostate cancer, bisphosphonate can prevent or delay skeletal disorders in men with bone metastases, as well as reduce bone pain. Bisphosphonates may also have a role in reducing osteopenia, which commonly accompanies the use of androgen deprivation therapy (Amaral et al., 2012).

The therapeutic approaches presented up to this point belong to the category of so-called "conventional" therapies (Fig.11). The limitations these therapeutic strategies present are different, such as their inability to detect distant micrometastases and prognostic

tumor aggressiveness; non-specific and non-selective drug delivery; no differentiation between indolent tumors and tumors exhibiting metastatic potential; real-time monitoring and predictive treatment response, which allow physicians to adjust dosimetry to prevent overtreatment, and avoid harmful side effects; or undertreatment that would instead lead to an incomplete remission from cancer (Freitas et al., 2021a).

Considering all of these details, the demand for the advancement of novel strategies for seeking precise cancer therapy has gained momentum in recent years and has promoted the emergence of cancer medicine, an area focused on the use of well-defined nanostructures to modify a drug's pharmacokinetic profile for improved treatment. The objectives of this strategy are to improve specificity in drug delivery to target sites, reduce side effects, and also to avoid the possible drug resistance mechanisms that tumor cells can develop in the course of treatment.

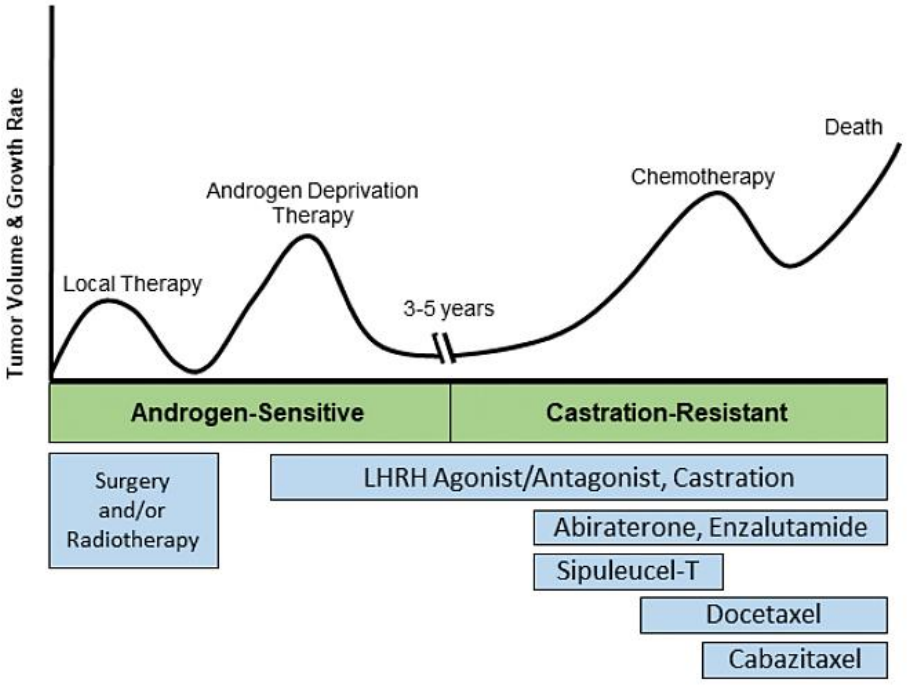

Fig. 11: Prostate cancer progression and treatment options.

2 NANOTHERANOSTICS

2.1 Introduction

One potential possibility in cancer medicine is the concomitant use of diagnostic and therapeutic agents for personalized cancer treatments. This type of system is known as a “theranostic” system. The term was coined in 2002 by Funkhouser. It is interpreted as a synergistic combination of therapeutic and diagnostic capabilities to enable simultaneous *in vivo* diagnostic, imaging and drug or gene delivery, followed by real-time screening at every stage of cancer treatment. Indeed, using the single nanoformulation it is possible to deliver different therapeutic agents, obtaining a synergistic effect in targeting multiple molecular markers involved in tumor heterogeneity (Ho et al., 2012).

Many theranostic systems have achieved impressive goals in the past years, showing great potential for future developments; some of them have been advanced to clinical trials in different phases and have been approved by the FDA for clinical use, exhibiting satisfactory performance (Ang et al., 2021; Zhou et al., 2021).

A theranostic system must allow for simple biological probing while maintaining physiological conditions at the time of delivery. Furthermore, the system must be able to penetrate any biological membrane it might encounter on its way to the target tissue or organ without undergoing toxic side effects. It is usually composed of: a therapeutic drug (a nucleic acid such as miRNA or siRNA, a therapeutic protein, or other chemotherapeutic agents), a carrier for the therapeutic cargo, ligands for targeting, and signal emitters (with unique radioactive, magnetic, or optical properties). Indeed, these elements can be covalently or non-covalently conjugated with a delivery platform (Roy Chowdhury et al., 2016).

One of the most promising strategies in designing a theranostic approach is "nanotheranostic" (nanotechnology-based theranostic). The approach is based on manipulating nanoparticles (NPs), technically defined by the International Unit of Pure and Applied Chemistry as particles with one dimension less than 100nm, which exhibit uniquely enhanced physical, chemical, and biological properties compared to their respective bulk material counterparts(Khan & Hossain, 2022) . A NP's basic composition includes the surface layer, the shell layer, and the core, which represents the NP's central part (Gavas et al., 2021a).

2.2 Characteristics of an ideal drug delivery system (DDS)

NPs are an example of a drug delivery system. Ideally, DDSs should improve the drug's stability, absorption, and therapeutic action in the target tissue and allow for its long-term release. Furthermore, it should be able to deliver various drugs with different release kinetics to reduce the frequency of drug administration to the patient and improve patient comfort. Moreover, the DDS should be able to correctly deliver the drug to the target tissue and maintain its concentration at the site for a sufficient period for therapeutic action to take effect(Parveen & Sahoo, 2008).

Table 8: Different roles of the physiochemical characteristics of NPs in their biodistribution and internalization (Zhou et al., 2021).

Physiochemical Characteristics	**Parameters**	**Outcomes**
Size	<10nm	Systemic distribution, rapid metabolism, less tumor enrichment, large tumor penetration
	100-200nm	Optimal for drug delivery, long blood circulation time, broad cellular uptake
	>200nm	Weak EPR effect, poor tumor enrichment, difficulty in penetrating a deep interior tumor
Surface charge	Cation	High cellular uptake, high toxicity, strong hemolytic activity
	Anionic	Difficult endocytosis by tumor cells, low cytotoxicity, long circulation time
	Neutral	Great steric prevention, low plasma protein adsorption, long blood circulation time, broad cellular uptake
	Zwitterionic	Long blood circulation time, less efficient uptake by tumor cells
Shape	Sphere	Fast internalization rate, deformability, avoidance of spleen filtration
	Rod	Less cellular uptake, relatively little perturbation on cell function
	Disc	Great cellular uptake
	Star	High drug loading and encapsulation efficiency, enhanced cellular uptake

The physicochemical characteristics of NPs (such as size, surface charges, shapes, and surface coating) play major roles in both tissue biodistribution and tumor uptake; rigorous efforts have been made to optimize them to improve the pharmaceutical and pharmacokinetic functions of NPs by bypassing RES. Table 4 summarizes the various roles of the physiochemical properties of NPs (Zhou et al., 2021).

2.3 Application of NPs in the treatment of PCa

Nanomaterials have been used extensively over the last decade for several applications, especially for the treatment and targeting of diseases. A carrier system, such as NP, must be biocompatible, inert, and capable of effectively transporting a high concentration of the drug. However, currently, many carrier systems are not able to satisfy the last condition.

As shown in Fig. 12, both organic and inorganic nanoparticles have appeared to be highly effective as drug delivery vehicles for a variety of medications to target PCa (Barani et al., 2020).

2.3.1 Mesoporous Silica Nanoparticles (MSNs)

MSNs are a class of materials that have received a lot of interest from researchers, mainly due to their unique characteristics, such as their easy large-scale production, adjustable uniform pore size, large surface area, and high pore volume. They can also be superficially decorated with active targeting groups to improve tumor targeting and chemotherapy selectivity. These properties give MSNs good drug encapsulation and delivery (Y. Gao et al., 2020).

Surface-ligated Ga-Au encapsulated MSNs are one of the most important nanomaterials for the treatment and diagnosis of PCa. A study by Chuanlam Gu and coworkers was based on using Ga-Au-loaded MSNs for the photothermal treatment of prostate cell lines. They demonstrated how these NPs were able to inhibit the growth of cancer cells and showed a significant anti-tumour effect in an in vitro cell line study (Gu et al., 2020).

Also Huan Wang and coworkers exploited the high selectivity, sensitivity, and the possibility of using MSNs as electrochemical immunosensors for targeting PCa (L. Wang et al., 2022).

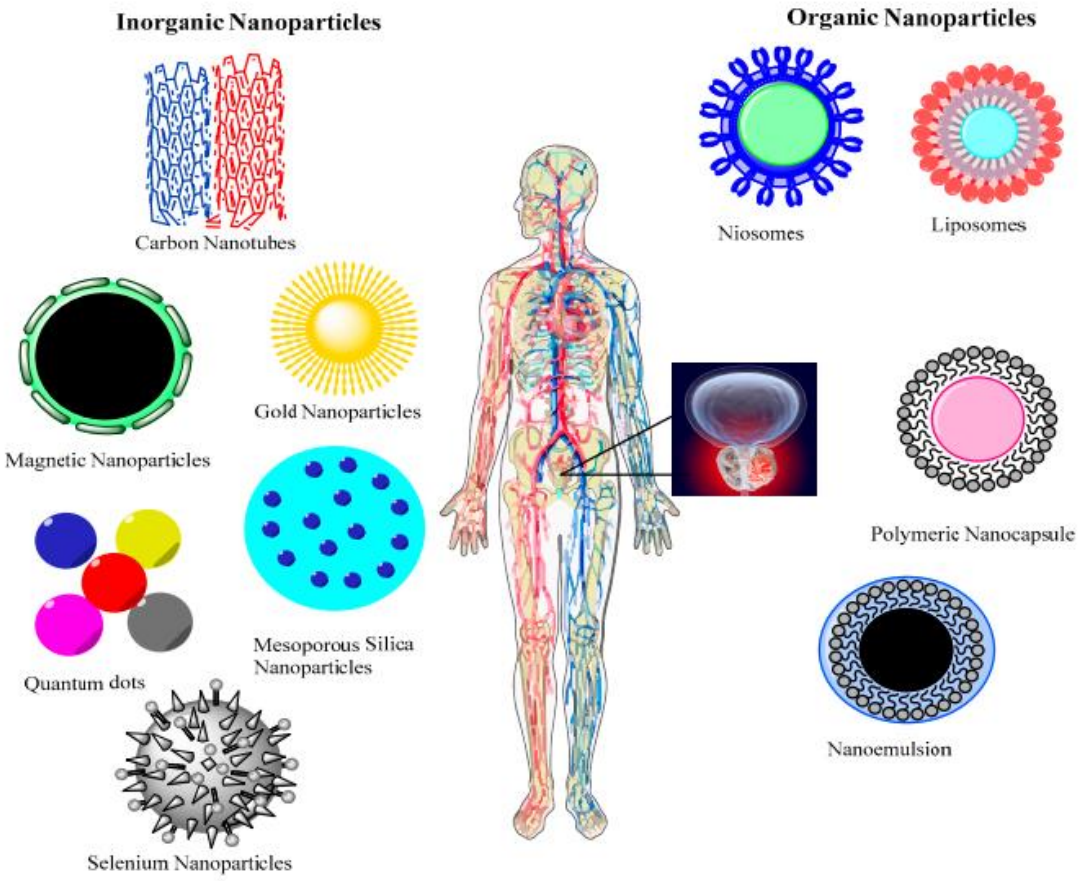

Fig. 12: Application of inorganic and organic nanomaterials in the treatment of PCa (Barani et al., 2020).

2.3.2 Gold Nanoparticles

The nanotheranostic application of AuNPs has turned out to be very promising, thanks to the unique combination of their optical and thermal properties. They possess adjustable size, shape, and surface chemistry and can have different forms, such as spheres, cubes, rods, clusters to threads. The different shapes influence their physical properties and their use in theranostic applications. Moreover, they can be functionalized to direct and release drugs to specific cell sites or groups.

One of the most important properties of AuNPs derives from their interaction with an electromagnetic field, which, at specific frequencies, can induce resonance and coherent oscillation of free electrons on the surface of the nanoparticles. This effect is called surface plasmon resonance (SPR). AuNPs can absorb this energy and convert it into heat, which leads to tumor ablation (Freitas et al., 2021b).

Hu and colleagues created surface-modified glucose nanoparticles (GLU-AuNPs) and showed how the presence of glucose may enhance the absorption of GLU-AuNPs by

cells, as well as how AuNPs can change the radiation cytotoxicity in PCa (Chen et al., 2015).

Zhang and colleagues developed and evaluated thioglucose-coated or capped AuNPs to inhibit growth and improve radiation sensitivity in prostate cancer cells. The experiments were conducted on the human prostate cancer cell line DU-145 and showed increased radiation and toxicity in prostate cancer cells (X. Zhang et al., 2008).

Rastinehad et al. developed Au-silica NPs to take advantage of gold nanoparticles' ability to lead to tumor ablation. They can absorb near-infrared light at highly transparent wavelengths and offer a highly localized light-based strategy for treating prostate cancer with few side effects (Taneja, 2020).

2.3.3 Selenium and Magnetic Nanoparticles

Selenium nanoparticles represent excellent anticancer agents; they have an important effect in reducing oxidative stress. The major advantage of SeNPs is the zero-oxidation state, which results in a significant increase in bioavailability and low toxicity compared to other oxidative states. SeNPs are capable of inhibiting the growth of highly proliferative cells by interrupting the cell cycle. Moreover, the small size of these nanoparticles guarantees a more efficient and selective cellular uptake (Barani et al., 2020).

Magnetic nanoparticles represent another class of nanoparticles used in the treatment of PCa. They can accumulate in PCa sites and, after electromagnetic stimulation, produce heat.

Yu et al. cross-linked superparamagnetic iron oxide nanoparticles to treat PCa. They are theranostic systems capable of both diagnosing PCa via MRI and releasing drugs at the tumor. The surface functionalization of these nanoparticles with prostate-specific membrane antigens (PSMAs) made the cellular uptake more selective (Khramtsov et al., 2019).

2.3.4 Liposomes

Liposomes consist of bilayer vesicles made of unilamellar or multilamellar phospholipids, which allow therapeutic drugs to be encapsulated within them. A typical liposome structure is composed of a "hydrophilic core" and a "hydrophobic phospholipid bilayer". They range in size from a few nanometers to many microns. Considering their unique architecture, liposomes can entrap hydrophobic substances in their membranes and load hydrophilic cargoes into the central aqueous hollow.

Liposomes present several advantages, such as low intrinsic toxicity, weak immunogenicity, biological inertness, high agent-loading efficiency, and controllable release kinetics. Additionally, lipids can be chemically modified to introduce theranostic functions into the liposomes. However, the application of liposome-based NPs is limited due to shortcomings like decreased encapsulation efficacy, speedy removal by MP, cell adsorption, and short shelf life(Aghebati-Maleki et al., 2020; Gavas et al., 2021b).

Thangapazhem et al. developed PCa-targeting liposomes that were surface functionalized with PMSA-specific antibodies and loaded with curcumin. The results demonstrated how this system can inhibit cell division without having any effect on cell viability (Thangapazham et al., 2008).

Narayanan et al. evaluated the effects on PEN-CAP8 cancer cells caused by the use of liposomes loaded with two different therapeutic agents: curcumin and resveratrol. Both of these phytochemicals efficiently inhibited cell growth and produced apoptosis (Narayanan et al., 2009).

2.3.5 Polymeric Nanoparticles

Polymer nanoparticles (PNPs) are defined as "colloidal macromolecules" with various structural architectures made up of different monomers. In PNPs, the drug can be either trapped inside or bound on the surface, depending on the type of drug release to be obtained.

PNPs are considered one of the most promising tools for theranostic application. This is mainly due to their important characteristics, such as biocompatibility, biodegradability, and stability against degradation. They can also be easily customised to include various specific functionalities. PNPs can be synthesised using both synthetic and natural polymers, but in both cases, they should first be modified so that they possess imaging ability and therapeutic activity. Initially, PNPs were obtained using non-biodegradable polymers, such as polyacrylamide, polymethylmethacrylate (PMMA), and polystyrene. However, their accumulation induced toxicity. PNPs are instead made from biodegradable polymers such as polylactic acid, poly(amino acids), chitosan, alginate, and albumin, which have low intrinsic toxicity and improve drug release and biocompatibility After drug release, the polymer matrix is degraded into harmless molecules, such as hydrogen, nitrogen, and water, and excreted from the body (Gavas et al., 2021b; Kundu et al., 2020).

There are currently several approaches available to produce PNPs that incorporate a variety of drugs via the chemical process for PCa treatment. For instance, Sanna et al. developed NPs with biodegradable block copolymers of PLGAPCL and PLA-PCL and loaded them with docetaxel (Fig.13). Studies conducted on PCa cell lines have shown a high antiproliferative activity of NPs compared to the free drug (Sanna et al., 2011).

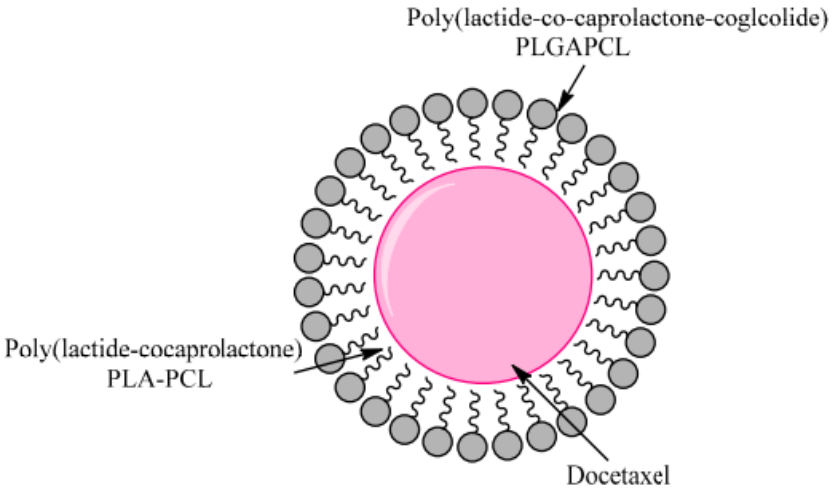

Fig. 13: Polymeric PLGA-PCL and PLA-PCL biodegradable nanoparticles loaded with Docetaxel for targeting PCa (Sanna et al., 2011).

Dhar et al. have developed nanoparticles of PLGA-b-PEG, with PSMA targeting aptamers on the surface as a carrier for the platinum compound, to deliver cisplatin to prostate cancer. The results showed that, also in this case, the antiproliferative activity of the overall system is better than that of free cisplatin (Dhar et al., 2008).

2.3.5.1 Stimuli-Responsive Polymeric Nanoparticles

PNPs potentially represent an efficient DDS able to respond to external stimuli. For this reason, efficient methodologies are used to synthesize stimuli-sensitive polymer nanoparticles, which demonstrate a response to prostate tumour-containing stimuli reactions.

Several possible stimuli can be used to trigger the release of drugs from nanoparticles (Fig. 14) . For example, the literature reports that the altered pH characteristic of the tumor environment is widely used as a stimulus to encourage the release of therapeutic agents in a biological or intracellular target organ of prostate cancer. Similarly, in the case of temperature, temperature-sensitive polymers have been extensively investigated

for intelligent drug delivery in cancer management. In this case, the temperature is used both as an internal and external stimulus.

PCa is one of the most aggressive tumors and is distinguished from other tumor forms by the overexpression of various enzymatic forms. For this reason, it could be advantageous to use enzymes as triggers to activate the release of anticancer molecules, weakening some bonds and dissociating the structure of the polymeric nanoparticles (Nangare et al., 2022).

pH-Responsive Polymeric Nanoparticles

pH is an endogenous stimulus with great potential for drug delivery. Along with tumor progression, pH in both lysosomes and endosomes is lower than in the ECM. Exploiting this feature, it is possible to develop nanoplatforms characterised by the presence of pH-sensitive bonds; these bonds are sensitive to the significant difference in pH present between the tumor microenvironment and the normal physiological state. The pH-sensitive polymer nanocarriers can be divided into two categories: 1) polymers crosslinked through electrostatic interactions of protonic groups, and 2) polymers crosslinked through acid-labile bonds (He et al., 2019).

For instance, in 2017, Yan et al. investigated the synergistic effect of epidermal growth factor receptor peptide, also known as GE11 targeted, and pH-responsive co-delivery of docetaxel and curcumin for PCa treatment. In this case, the nanoparticles demonstrated 85.2% of the cumulative release of curcumin, which followed a sustained release at pH 5. Docetaxel, on the other hand, is mildly pH-dependent (Yan et al., 2017).

Enzyme-Responsive Polymeric Nanoparticles

Enzymes are essential elements for the physiological activities of PCa. During the development of PCa, there are pathological changes in the expression of specific enzymes, such as, for example, an increase in the levels of matrix metalloproteinases (MMPs) and proteinases. Consequently, it is possible to develop enzyme-responsive polymer nanoparticles able to distinguish the different statuses of specific enzymes between the TEM and healthy tissue and realise enzyme-mediated release (He et al., 2019).

For instance, to improve the efficacy of polymeric nanoparticles against tumor tissue, Dube et al. developed a protease-responsive 3-helix micelle nanocarrier based on amphiphilic peptide- PEG conjugates with DOX. The results showed how the micelles,

after being permeated into the tumor tissue, were accurately cleaved by proteinase K present in the tumor site (Dube et al., 2013).

In some cases, tumor growth marker enzymes are used as enzyme-sensitive stimuli. MMPs, especially MMP-2 and MMP-9, play a major role in the invasion, metastasis, and angiogenesis of tumors. Usually, they are overexpressed in the extracellular matrix of the tumor microenvironment and represent an optimal endogenous stimuli-responsive strategy. Peng et al. designed an MMP-2 responsive HPMA copolymer and tumour-penetrating peptide conjugate nanocarrier (P-DOX-PLGLAG-iRGD). The overall system demonstrated a high capacity for tumour accumulation and inhibition of the cancer cell lines DU145 PCa (Peng & Kopeček, 2015).

In addition to MMPs, PSA could be a good endogenous enzyme for stimuli-responsive polymer nanocarriers. PSA is one of the most important biomarkers of PCa prognosis and indicates the degree of tumor development since excessive PSA is detected in the peripheral blood of PCa patients. Furthermore, PSA is only found in the extracellular fluid within the prostate and PCa metastatic sites. Levi et al. developed PSA-responsive peptide-conjugated polymer-carriers that were internalized by mesenchymal stem cells (MSCs). This system constitutes the so-called "Trojan horse" model. MSCs can penetrate more deeply into tumor tissue than a free drug; the high concentration of PSA induces the toxicity of the PSA-responsive peptide and selectively causes cell death of PSA-secreting PCa cells in vivo (Levy et al., 2016).

Reduction-Responsive Polymeric Nanoparticles

As the tumor progresses, the intracellular redox status tends to increase. Glutathione (GSH), one of the most important anti-oxidants *in vivo*, is present in significantly different concentrations in the intracellular (about 10mM) and extracellular (about 2mM) domains of tumor cells. As a result, reduction-responsive polymer nanocarriers hold great promise in the treatment of PCa.

These systems usually involve the introduction of disulfide bonds in the polymer nanocarriers, which are sensitive to the presence of reductive substances such as GSH. It can degrade the disulfide bond and trigger the release of the pharmacological load in the tumor region (He et al., 2019).

Becker et al. have developed layer-by-layer (LbL) assembled polymer nanocarriers containing disulfide bonds to deliver siRNA and anti-apoptotic factors. This system

demonstrated indirectly that reductio-responsive polymer nanoparticles have great potential for treating PCA (Becker et al., 2011).

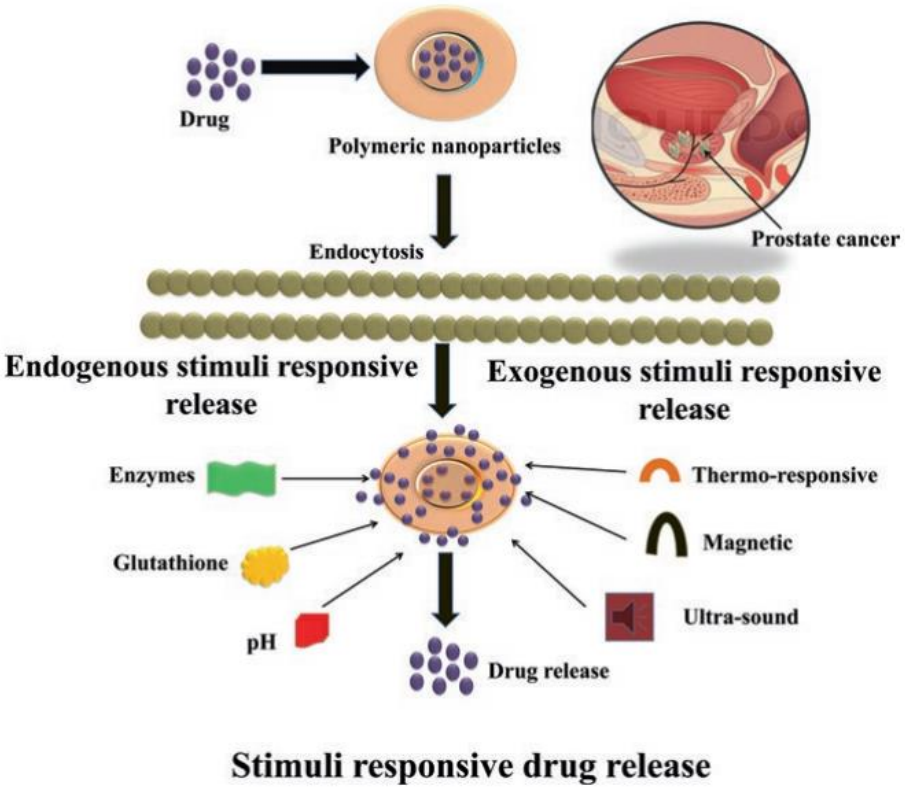

Fig. 14: Endogenous and exogenous stimuli-responsive polymeric nanoparticles for PCa management (Nangare et al., 2022).

2.4 Application of NPs in the molecular imaging of PCa

2.4.1 Quantum dots (QDs)

Initially discovered in 1989 by Alexei Ekimov, QDs are engineered fluorescent nanoparticles with unique optical and chemical properties and promising potential in several biomedical applications. The use of QDs has brought about a significant change in bioimaging, drug research, and diagnostics and represents a very useful tool for the early detection and diagnosis of PCa (Farzin & Abdoos, 2021).

QDs often described as “artificial atoms”, are fluorescent semiconductor nanocrystals mostly made up of chemicals ranging from groups II-VI, III-V or IV. In the core crystal of a single QD, there are approximately 100-100,000 atoms. They are extremely small in size (typically ranging between 2-10nm in diameter), which affects their electronic and

optical properties differently than those of bulk materials (H. Zhang et al., 2008). Structurally, QDs are characterised by a semiconductor core overcoated by a shell to improve biocompatibility, photoluminescence (PL), quantum yield (QY) of fluorescence, and stability (Fig.15) . It is possible to alter PLQY via passivation of the surface of QD by a shell of a larger bandgap semiconductor and the leaching of the metal ions from the core of QD (Bruno, 2022).

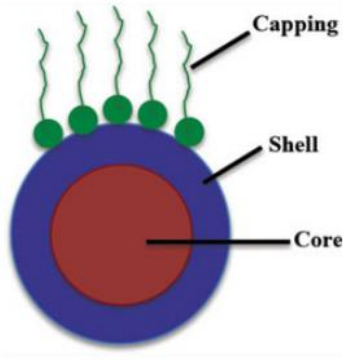

Fig. 15: Schematic representation of core-shell QDs; a core in the centre (brown), over it a shell (blue), above a QD is functionalized by different molecules (Bruno, 2022)

QDs are fluorophore nanocrystals whose excitation and emission differ from traditional organic fluorophores. Instead of electronic transitions from one valence orbital to another, QDs are characterised by the transition of an electron (Fig.16) , from the valence to the conduction band, overcoming an energy gap, generating a conduction electron and leaving a hole in the valence band. The electron-hole pair is quantum-confined by the small size of the nanocrystal. Fluorescence occurs when an excited electron returns to its ground state, emitting a photon of a specific wavelength. Changes to the size of the confining crystal alter the energy bandgap, resulting in a different colour of the fluorescent photon. Generally, the smaller the QD, the greater the energy gap between the bands, and consequently, the shorter the wavelength of the emitted fluorescence, and there will be a colour shift from red to blue in the light emitted (Calatayud et al., 2022).

QDs can be made of metallic or semiconductor materials (Ni, Co, Pt, and Au). Most QDs are binary semiconductors, meaning they are composed of two different materials, such as cadmium selenide (Cd/Se) QDs. They are designed using a Cd/Se inner core encapsulated within a ZnS outer core and have been demonstrated to be effective

fluorophores with a long fluorescence lifetime (H. Zhang et al., 2008). The type of substance used to obtain the QDs influences the final size of the QDs themselves.

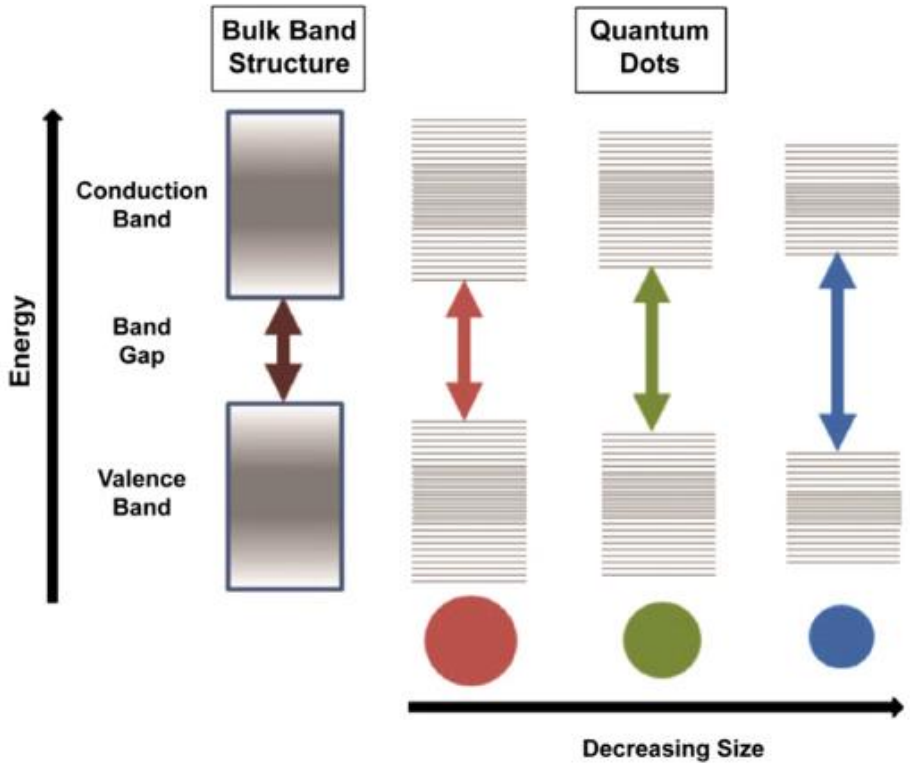

Fig. 16: The quantum confinement effect on the energy levels in semiconductor quantum dots. The band gap energy increases with decreasing QD size (Calatayud et al., 2022).

2.4.1.1 Salient characteristics of QDs

I. QDS are more resistant to degradation and more photostable than traditional fluorophores, due to their inorganic composition. This feature allows the tracking of the cellular process for a longer period.
II. QDs are 10-20 times brighter than organic dyes.
III. QDs have a broad absorption spectrum, a narrow emission spectrum, and excellent photo resistance capacity.
IV. The optical properties of QDs are affected by several aspects, such as core size, core composition, shell composition, and surface coating. Although all four properties can alter the emission of QDs, the most influential ones are core size and composition (Pericleous et al., 2012).
V. The surface of the QDs can be coated with different chemical entities and biomaterials owing to their easily moldable shape, which makes them suitable for biological systems.

VI. Because of their nanosize, they possess a large surface area, which allows for a high drug-loading capacity.
VII. QDs are chemically inert and excellent candidates for *in vitro* and *in vivo* use. They can be applied for theranostic drug delivery.
VIII. QDs can encapsulate both hydrophobic and hydrophilic drugs and show a long duration of blood circulation (Gidwani et al., 2021).

2.4.1.2 Toxicity of QDs

QDs' toxicity, which is based on their physicochemical characteristics, is the main problem with their usage in biological applications. It mostly depends on the QDs' size, the QDs' preparation material, the QDs' amount, the QDs' administration method, the QDs' capping substance, and the environment.

For example, in CdSe QDs, toxicity is caused by the release of cadmium ions from the core of the QDs due to photolysis and/or oxidation. Other mechanisms that contribute to the cytotoxicity induced by CdSe QDs are the formation of reactive oxygen species (ROS), which induce cell damage, and the interaction of QDs with individual cell components or with the cell membrane. The cellular dysfunctions generated by the presence of QDs are accompanied by apoptotic and necrotic biochemical changes, including morphological alterations in the plasma membrane, nuclear and mitochondrial damage, lysosome enlargement, and a reduction in the concentration of cytochrome C (Lin, 2016).

2.4.1.3 Carbon quantum dots (CQDs)

Various attempts have been made to solve the problem of toxicity associated with the use of QDs. Carbon quantum dots (CQDs) have recently drawn increasing attention due to their important qualities, like water solubility, tunable fluorescence, chemical inertness, easy and inexpensive synthesis, good photostability, biocompatibility, and above all, non-toxicity.

CQDs are a type of carbon-based fluorescent nanomaterial consisting of carbon nanoparticles with a size smaller than 10 nm. They were accidentally discovered during the processing of single-walled carbon nanotubes (SWCNT). Since then, the fluorescence properties of CQDs have been extensively investigated, making CDQs a new class of fluorescent biocompatible nanomaterials. Several simple synthesis methods have been proposed to obtain CQDs.

Structurally, they are characterised by amorphous to nanocrystalline cores with sp2 carbon; they have a polar nature and can be easily modified thanks to the presence of different functional groups on their surface, such as hydroxyl, carboxyl, ester, ether, or amino. Furthermore, CDQs can be prepared using green chemistry principles and thus without the use of toxic reagents. Green CQDs, which are synthesised without chemical exposure from organic compounds, have recently received a lot of attention due to the wide availability of starting materials, high quantum yield, and self-passivation. Any type of C-rich biowaste can be applied, such as tea leaves, coffee beans, or fruit peels.

The characteristics of CQDs have been extensively investigated for their use as fluorescent nanoprobes for bio-imaging, gene and drug delivery agents, and antibacterial agents (Devi et al., 2019; Janus et al., 2019).

Synthesis of CQDs

CQDs can be prepared by two general methods, bottom-up and top-down, which differ in the carbon source used for the synthesis of CQDs. Bottom-up methods are more eco-friendly as basic building blocks, such as fructose or glucose molecules, are taken up for the bottom-up synthesis of CQDs. Then, they undergo carbonization, condensation, and polymerization processes to obtain fluorescent CQDs under optimised synthesis conditions. These methods require the use of external energy sources such as microwave heating, ultrasounds, or conventional heating. This type of approach allows for fast, easily scalable, and cost-effective synthesis of CQDs but suffers from a poor ability to control the size of the synthesised CQDs. Subsequently, it is possible to modify the size of the CQDs with post-processing treatments, such as sonication, filtration, dialysis, centrifugation, column chromatography, and gel electrophoresis.

In the case of a top-down approach, CQDs are obtained starting from a block of carbon that is broken into smaller units of less than 10 nm. These methods are harsher, as they require high temperatures and pressures. The best-known top-down methods include arc discharge, laser ablation, and electrochemical methods. The problem with top-down approaches is that they involve complicated and time-consuming steps, which makes them less interesting from a commercial and scientific point of view (Devi et al., 2019; Janus et al., 2019).

Surface modification of CQDs

The surface functionalization of the CQDs allows for improved absorption and photoluminescence properties. Other functionalizations of CQDs are important to modify

their ability to interact with organic molecules, ions, drugs, and living organisms. Different types of molecules are used for the surface passivation of CQDs, which can be neutral, such as PEG, or charged (positively or negatively). The functionalization procedure can result in a net neutral or negative charge on the surface of the CQDs, and it is functional for therapeutic applications. In particular, neutral groups can escape clearance by the immune system, while negatively charged ones can avoid protein uptake due to electrostatic repulsions. In addition, the number of negative or neutral charges affects the internalisation efficiency in cancer cells, while positive charges facilitate cellular internalisation due to electrostatic interactions with the negative charges of cell membranes (Devi et al., 2019; Janus et al., 2019).

Cytotoxicity of CQDs

The cytotoxicity of CQDs has been extensively investigated in different cell lines and across different concentration levels, with or without surface passivation. It has been demonstrated that they have low cytotoxicity and easy penetration into the cells (Naik et al., 2022).

The possible cytotoxicity of CQDs does not depend on the carbon core but on the nature and charge of the functional groups. The neutral functional groups showed the best results, being the least toxic. Negatively charged groups cause cell cycle arrest and can induce oxidative stress; instead, those positively charged groups lead to cell cycle arrest in the G0 phase. However, these toxic effects were detected at a concentration of CQDs higher than 50ug/mL, while for concentrations lower than 25ug/mL, no toxic effects on cells were observed (Devi et al., 2019).

2.4.1.4 Biomass-derived carbon quantum dots

Among the different possible carbon sources, biomass and its derivatives represent a good carbon source for the preparation of biomass CQDs (BCQDs). According to the International Energy Agency, the term "biomass" refers to the set of organisms formed by photosynthesis, including all animals, plants, and microorganisms.

Biomass carbon sources are very advantageous for the synthesis of CQDs because they are eco-friendly natural products and compared to other carbon sources, they are inexpensive, easy to obtain, green, and abundant. Moreover, it allows the conversion of low-value biomass waste into useful and valuable materials. BCQDs are characterised by good biocompatibility and stable fluorescence emission, which are widely used in

sensing, imaging, sensors, drug delivery, and other applications (Meng et al., 2019; Y. Wang et al., 2020).

Methods for the synthesis of BCQDs

The synthesis of BCQDs, as in the case of CQDs, is based on two different approaches: top-down and bottom-up. Usually, BCQDs are obtained by exploiting bottom-up approaches, which guarantee a high yield and are convenient for introducing heteroatom doping into the synthesis process.

The most commonly used methods to synthesize BCQDs from biomass include hydrothermal carbonization (HTC), microwave-hydrothermal, microwave, chemical oxidation, and pyrolysis carbonization methods.

Hydrothermal Carbonization Method (HTC). HTC is a promising technique for converting biomass to carbon material for a large variety of potential applications. It consists of the thermochemical degradation of biomass in the presence of water (the water/biomass ratio can generally vary from 5:1 up to 75:1) at high temperatures and pressures (Meng et al., 2019;. The method is simple to operate, controllable, and non-toxic, and no passivation is required for photoluminescence; the main problem, however, is the difficulty in controlling the final size of the QDs (Wareing et al., 2021).

Through HTC, it is possible to obtain novel carbon-based materials starting from biomass carbon precursors such as sweet pepper, garlic, the husks of nuts, papaya juice, and rice husk (Meng et al., 2019).

Microwave method. In this method, BCQDs are synthesised by converting electromagnetic energy into thermal energy using microwave heating. This allows for high yields and purity.

Pyrolysis carbonization method. Pyrolysis is the process through which a substance is irreversibly decomposed using high pressure and high temperature (HPHT). It is one of the most commonly used methods for obtaining BCQDs. The size of the QDs obtained from biomass as a carbon source ranges between 0.4 nm and 6 nm, with a quantum yield ranging between 3% and 25%.

Chemical oxidation method. In this method, an oxidizing agent oxidizes a target, causing it to lose electrons. An oxidation method with a strong oxidizing agent, such as hydrogen peroxide, is called the chemical oxidation method.

BCQDs in bioimaging applications

BCQDs are better optical bioimaging agents than chemically derived CQDs, as they show better biocompatibility. Furthermore, their small size, high water solubility, photostability, and photobleaching resistivity make them ideal candidates for bioimaging applications. Research groups have used a large variety of biomass materials to obtain BCQDs (Tejwan et al., 2020).

There are many examples of biomass-derived CQDs that are used as imaging agents. For example, Feng et al., using microwave radiation, synthesised BCQDs using silkworm chrysalis as raw material. The BCQDs obtained possess low cytotoxicity when used at a concentration of 15 mg/mL and show bright blue, green, and red colours under an inverted fluorescence microscope during cellular imaging experiments. Seng et al., on the other hand, synthesised BCQDs starting from flax seeds. At the same time, lychee seeds and jujube kernels were also used to prepare BCQDs (Meng et al., 2019;. Instead, Yang et al. have synthesised green fluorescent CQDs from chitosan using the HTC method for in vitro imaging of human lung cancer (A549) cells. Hsu et al. (Tejwan et al., 2020)obtained coffee-ground-derived green fluorescent CQDs that were internalised via endocytosis in LLC-PK1 cells and used for imaging.

2.5 Mechanism of NPs targeting

The main goal of drug and gene delivery systems, such as NPs, in cancer treatment and diagnosis, is to deliver drugs to cancer cells without affecting healthy cells or tissues. Targeting cancer cells is an important characteristic of NPs since it allows them to improve therapeutic efficacy while protecting healthy cells and tissues from drug cytotoxicity. Targeting mechanisms can be divided into two categories: passive and active targeting (Yao et al., 2020a).

2.5.1 Passive targeting

Tumors are not exclusively clusters of tumor cells but can be considered "organs" in which tumor cells can build a microenvironment, known as a TME, that can cause non-malignant cells, such as those of the immune system, to support tumor growth rather than suppress it. TME plays a relevant role in different stages of tumor development, such as local resistance, immuno-escaping, and distant metastasis (Kalyane et al., 2019).

In tumors, the blood vessel system is completely different from the normal vasculature; this is due to the aggressive growth of the neoplastic cell population and the overexpression of pro-angiogenic factors. In particular, tumor vasculature is known to be characterised by dynamic aberrant structures and blood vessels that are immature, tortuous, and hyperpermeable. Tumor blood vessels lack a conventional blood vessel hierarchy, as arterioles, capillaries, and venules are not identifiable. The blood vessels are of inconsistent diameter and do not have a regular shape. The tumor lymphatic vascular system is absent or malfunctioning, so the ability to deliver nutrients via blood vessels and remove waste products via the lymphatic system is drastically decreased. Tumor blood vessels are more permeable than normal blood vessels. This increase in the permeability of the tumor blood vessels makes possible the accumulation of NPs (in the size range of 20-200nm), while the ineffectiveness of the lymphatic system prevents their removal from the tumor tissue (Siemann, 2011). This passive phenomenon is called the "Enhanced Permeability and Retention (EPR) effect" and was discovered for the first time by Matsumura and Maeda in 1980. The EPR effect represents one of the driving forces behind passive targeting (Danhier et al., 2010).

Passive targeting consists of the transport of NPs through leaky tumor capillary fenestrations within the tumor interstitium through passive diffusion (Fig.17) , which is defined as a process of molecular transports across the cell membrane, according to a concentration gradient, and without the need for an energy contribution (Danhier et al., 2010). In addition to the EPR effect, TME represents another important factor for the passive delivery of nanocarriers [80]. Nevertheless, the EPR effect represents the gold standard in cancer-targeting drug design. All NPs use the EPR effect as their main guide to reach the tumor site. Except for hypovascular cancers like prostate and pancreatic cancer, this is true for the vast majority of cancers (Danhier et al., 2010) .

By exploiting the passive target, there are, however, limitations in reaching the tumor site. For example, passive targeting depends on the degree of tumor vascularization and angiogenesis, so the extravasation of NPs will vary with tumor type and anatomical site. Moreover, the high interstitial fluid pressure of solid tumors does not allow adequate uptake and homogeneous distribution of drugs in the tumor (Danhier et al., 2010)

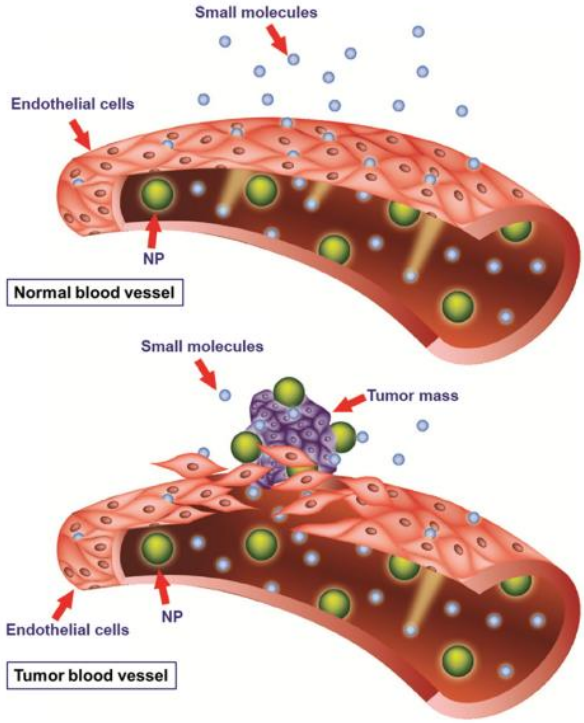

Fig.17: Targeting of nanomedicines by the enhanced permeability and retention (EPR) effect. Tumor vessels contain large fenestrations between the endothelial cells allowing the NPs to reach the matrix and the tumor cells. Conversely, normal tissues contain tightly joined endothelial cells, preventing the diffusion of NPs from the blood vessels (Danhier et al., 2010).

2.5.2 Active targeting

Some limitations of passive targeting can be overcome by implementing active targeting strategies as well. Active targeting, also known as ligand-mediated targeting, involves directly interacting between ligands on the surface of NPs and receptors or antigens overexpressed on tumour cells (Fig.18) (Danhier et al., 2010). The interaction that occurs between ligands and receptors induces receptor-mediated endocytosis, which allows NPs to be efficiently internalised (Yao et al., 2020b). To further promote the accumulation of NPs at the tumor site, ligands can also be used to target intravascular tumor cells or tumor blood vessel endothelial cells.

The ligand conjugation chemistry and the types of ligands available contribute to the effectiveness of the actively targeted NPs, which can also be influenced by other factors, such as the administration route or the non-specific binding of proteins in the NPs' pathway to the target site through the bloodstream. The final efficacy of the system can

also be influenced by the physicochemical properties of the NPs, such as the ligand density, the size of the NPs, or the choice of the target ligand (Bertrand et al., 2014)..

One of the main objectives of active targeting is to increase the internalisation of NPs by tumor cells. To that end, Kirpotin et al. demonstrated that the presence of anti-HER2 targeting moieties on the liposome surface significantly increases their capture in HER2-expressing tumour cells instead, in the case of non-targeted liposomes, it has been seen that these tend to accumulate in high concentrations in the stromal and perivascular spaces. In these cases, the liposomes are rapidly taken up by the macrophages (Bertrand et al., 2014).

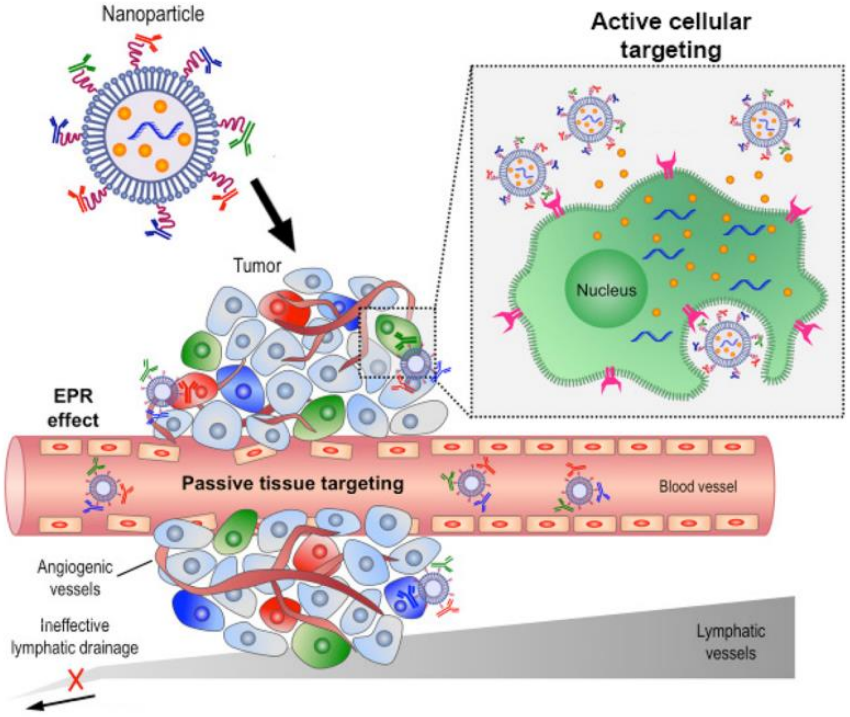

Fig. 18: Representation of the active tumour targeting process. Through the EPR effect, circulating nanoparticles initially penetrate into the tumour bulk before being recognised by cellular receptors and internalised by cells (Yao et al., 2020b).

Numerous possible strategies have been developed to functionalize NPs with target ligands and to evaluate their efficacy in preclinical models. In the last 15 years, only 13 ligand-targeted NPs able to target tumor cells have entered clinical trials (Pearce & O'Reilly, 2019).

Typically, the target ligands used are small molecules, polypeptides, protein domains, antibodies, and nucleic acid aptamers. In particular, antibodies and antibody fragments,

and protein domains are mainly used for their high specificity towards the target. Examples of commonly targeted ligands are presented in Table 5.

Table 5: Examples of commonly used targeting moiety (Pearce & O'Reilly, 2019).

Class	Ligand	Targets	Advantages	Limitations	Clinical approve
Antibodies	a-Herceptin Rituxan b-CD19	– HER2 – CD20 – CD19 antigen	High affinity and strong binding; already in clinical trials; therapeutic potential	High production cost; pharmacokinetics; 'binding site barrier effect'; potential immunogenicity	a-Approved as antimetastatic breast cancer (i.e. trastuzumab).[105] b-Approved as HIV Medicines.[106]
Peptides	a-RGD b-NGR	– $\alpha_v\beta_3$ integrins, Aminopeptidase N	High affinity	Reduced circulation half-life	a-[^{18}F]Galacto-RGD is approved as RGD PET tracer in human.[107] b-NGR-hTNF/DOX as vascular targeting agent is in phase 1b.[108]
Proteins	a-Transferrin LHRH	– Transferrin receptor – LHRH receptor	Already in clinical trials	High production cost	a-SGT-53, a scFv anti-TfR1 liposome complex is in Phase I and II.[109]
Aptamers	a-Pegaptanib	– VEGF receptor	Possible to develop for any target	High production cost	a-Approved as Macugen (Pegaptanib Sodium) Injection.[110]
Small molecules	a-Folate b-Galactose	– Folate receptor – Asialoglyco-protein receptor	Low production cost, low molecular weight; simple chemistry	Could reduce circulation time	a-Phase II.[111] b-Not approved yet

Among the classic ligands, numerous formulations have been developed using transferrin to bind to transferrin receptors, which are overexpressed in numerous tumors. For example, Singh et al. exploited transferrin to evaluate the passive and active targeting of NPs in vivo. They created two nanoparticle systems in poly(glycidal methacrylate) that encapsulated docetaxel and magnetite for therapy and imaging, respectively. One system, the one that can actively target tumor cells, has been modified on the surface to facilitate the attack of transferrin-targeting ligands. Then, the targeted and nontargeted systems were compared by evaluating their therapeutic efficacy in an orthotopic prostate cancer model. The results showed that only the targeted system was able to demonstrate the absence of off-target toxicity in terms of body mass loss and nonspecific spleen and kidney uptake (Pearce & O'Reilly, 2019).

Small internalizing peptides are widely used in the active targeting of tumor cells, as they are easily synthesized and are more stable than antibiotics. For example, the RGD peptide can target the adhesive integrin receptor αvβ3, which is highly overexpressed in endothelial cancer cells (Pearce & O'Reilly, 2019).

A classic example of a ligand is folic acid (FA), which binds specifically to the folate receptor (FR), which is significantly upregulated in many human tumors while being minimally expressed in many normal tissues (Attia et al., 2019).

Hyaluronic acid (HA) is a negatively charged, linear glycosaminoglycan that can be exploited as a targeting agent. The advantage associated with the use of HA is twofold: (I) HA has a high affinity for CD44 receptors, which are overexpressed on the surface of tumor cells; in addition, it is a polymer that can formulate stealth NPs.

Another promising strategy is to use small molecules as ligands, which are mainly advantageous in that their small size does not affect the pharmacokinetics of the transport system. Furthermore, they can be synthesized on a large scale, have high stability over time, are inexpensive, the process of synthesis and conjugation to NP is easy, and they have a low risk of triggering side effects. This class of ligands contains naturally occurring moieties such as glycans for targeting glucose transporters, folic acid for targeting the folate receptor and synthetically derived glutamate urea lysine for targeting PSMA (Pearce & O'Reilly, 2019).

2.5.3 Major ligands and targets in PCa

2.5.3.1 Prostatic-specific membrane antigen (PSMA)

PSMA is mostly expressed on the surface of PCa cells and is also found in the central nervous system, kidney, proximal small intestine, and salivary glands. In PCa, PSMA represents an excellent target due to the presence of a large extracellular domain and its overexpression in tumor cells; it has also demonstrated excellent potential in the internalization of nanocarriers.

Several formulations of NPs conjugated with ligands to target the extracellular domain of PSMA have been developed. For instance, Hrkach et al. functionalized, with a small molecule ligand, ACUPA, a docetaxel-encapsulated polymeric NP. In vitro studies have shown that this system has a higher affinity for PSMA than the same system without the ligand.

Mangadlao et al. investigated the theranostic capabilities of a system to which a ligand, PSMA-1, was attached. The system consisted of a gold nanoparticle conjugated to a fluorescent photodynamic therapy drug, Pc4, to assist in the intraoperative detection of PSMA-positive prostate cancer cells. In vitro studies on this system using spectroscopy techniques revealed that PSMA-positive PC3pip cells uptake gold NPs more than PSMA-negative cell lines, demonstrating active targeting of the PSMA-1 ligand for the receptor PSMA.

Nahesh et al. have developed superparamagnetic iron oxide NPs (SPIONs) encapsulating docetaxel that express on the surface a ligand, the antibody J591, able to target the external domain of PSMA. The targeting efficacy was evaluated by *in vitro* studies, which demonstrated increased uptake of the nanoparticles in PSMA-positive cell lines.

In addition to iron oxide nanoparticles, the researchers created bovine serum albumin (BSA) nanoparticles, which are polyethylenimine biocompatible NPs that are targeted by antibodies. For this purpose, it is also possible to attach aptamers, which are small, single-stranded DNA or RNA oligonucleotides that can selectively bind to a specific target with high affinity. The most widely used aptamers to target PCa cells are A9 and A10. Dhar et al. functionalized the surface of PLGA polymer nanoparticles with the A10 aptamer to deliver cisplatin. NPs demonstrated increased internalization compared to untargeted particles (Choksi et al., 2022).

2.5.3.2 Gastrin-releasing peptide receptor

The phospholipase C signalling pathway is activated by the gastrin-releasing peptide receptor (GRPR), a G-protein coupled receptor that controls smooth muscle contractions and the release of digestive hormones. The GRPR has a role in the proliferation of epithelial cells and the promotion of mitosis and is aberrantly expressed in several malignancies, including PCa. A neuropeptide called bombesin has a homologous sequence of amino acids to the mammalian gastrin-releasing peptide, enabling it to attach to the GRPR with great affinity. To combat PCa, many bombesin analogues have been developed that target the GRPR.

Martin et al. created a preclinical magnetic resonance imaging probe based on a SPION formulation functionalized with bombesin. Through the use of click chemistry, bombesin and the fluorescent dye rhodamine were coupled to the surface of the SPION, making production simple. In vitro tests showed internalisation of the SPION, and PC3 prostate cancer cells showed selective uptake of the bombesin-functionalized SPIONs as opposed to non-targeting SPIONs.

Chitosan nanoparticles conjugated with bombesin were created by Lee et al. to target the GRPR. A near-infrared fluorophore called Cy5.5 was used to mark the chitosan nanoparticle conjugates. Bombesin-targeting chitosan nanoparticles demonstrated enhanced binding to the PC3 cell surface and tumour formation compared to non-

targeting nanoparticles. To employ SPION as a possible MRI tracer, it was further conjugated to the chitosan complex (Choksi et al., 2022).

2.5.3.3 Glucose-regulated protein

The heat shock protein family includes glucose-regulated proteins, which are involved in both protein folding and the transportation of misfolded proteins for destruction. They are essential for the efficient operation of the endoplasmic reticulum and mitochondria, which are where they may be located. According to their molecular weight, glucose-regulated proteins are classified, with GRP78 being recognised as a ubiquitous protein involved in the endoplasmic reticulum's homeostatic equilibrium. When the endoplasmic reticulum is under stress, the nucleus produces genes related to the unfolded protein response, which leads to the induction of GRP78, which controls protein folding and preserves cellular homeostasis. To sustain protein folding, neoplastic cells cause endoplasmic reticulum stress and subsequently upregulate GRP78.

GRP78 has been found to have a role in carcinogenesis, cell proliferation, the downregulation of apoptotic proteins, and the adhesion between metastatic prostate cancer cells and the bone microenvironment in animal models of various cancers, including prostatic adenocarcinomas. Additionally, compared to benign cells, malignant cells show a higher localisation of GRP78 to their cell membrane. GRP78 has been targeted and inhibited using a variety of peptides and antibodies, both on the cell surface and in the endoplasmic reticulum.

To co-deliver docetaxel and GRP78 siRNA for an anti-prostate cancer impact, Zhang et al. created a preclinical calcium phosphate - polymeric conjugate nanoparticle that targets GRP78 with the Arg-Gly-Asp (RGD) ligand. It is proposed that the introduction of GRP78 siRNA will quiet GRP78 and make prostate cancer cells more susceptible to treatment. When compared to the simultaneous administration of a combination of free docetaxel and free GRP78 siRNA or either alone, in vitro investigations of PC3 prostate cancer cells showed a synergistic induction of apoptosis upon treatment with nanoparticles co-encapsulating both GRP78 siRNA and docetaxel (Choksi et al., 2022).

3 LAYER-BY-LAYER (LbL) TECHNIQUE

3.1 Introduction

The complex microenvironment of tumors, particularly its complexity and heterogeneity, is one of the most significant barriers to achieving potential therapeutic effects against cancer. The great majority of tissues and organs in vivo have been exposed to a variety of chemotherapeutic medications, which is an efficient method for eliminating tumour cells. These drugs have some inherent disadvantages, though, such as poor tumour tissue targeting, limited biocompatibility, and dose-limiting toxicity difficulties. It is therefore urgently needed to develop new strategies for administering chemotherapy medicines with greater therapeutic effectiveness(X. Zhang et al., 2021).

Due to their unique properties, such as the ability to induce the EPR effect, due to the reduced size, the potential for surface modifications for identifying the characteristics of healthy cells and cancer cells in clinical contexts, and the ability to simultaneously target the cancerous tissue, nano drug delivery systems (NDDS) have attracted widespread scientific interest for anticancer treatment in recent years. The layer-by-layer (LbL) construction of multilayer films onto nano-templated nanoparticles, followed by the optional removal of the template, is one of the most promising techniques for producing this type of NDDS for cancer therapy. The LbL assembly technology has intrinsic benefits over other methods for producing NDDS, such as nanoprecipitation, solvent evaporation, and in situ polymerization, making it ideal for use in the creation of NDDS (X. Zhang et al., 2021).

In addition to producing homogeneous nanoparticles, the LbL assembly technique can also produce heterogeneous NDDS with various components and complex architectures, such as multilayers. By adjusting the assembly conditions, the thickness, surface charge, and shape of the multilayers may be effectively regulated. Additionally, the layers interact chemically strongly, resulting in the LbL-formed NDDS's excellent mechanical and thermal stability. Medicines that are both hydrophilic and hydrophobic can be added with improved loading efficiency (X. Zhang et al., 2021).

3.2 Basic principles of the LbL technique

Layer-by-layer (LbL) assembly is a potent solution-processing method for producing multilayer films and coatings with control over the composition of the hierarchical material layers and the final nanoscale thickness of the films. LbL films are typically made by

alternately coating polymers that have been solubilized with opposing charges (creating polyelectrolyte multilayers); however, the technique may be adjusted and changed to process a range of functional materials.

Many other molecular interactions have also been developed to create LbL assembly techniques, such as hydrogen bonding, hydrophobic interactions, covalent bonding, host-guest interactions, van der Waals forces, and biospecific interactions, which can all be used to create LbL systems and may even be the main force behind film formation.

LbL self-assembly occurs according to a routine series of steps, schematically illustrated in figure 19: first, a multilayered structure is created by immersing a charged substrate in a solution of an oppositely charged colloid to produce the first monolayer; followed by a washing cycle to remove loose material and prevent contamination of the next oppositely charged colloid; the coated substrate is then submerged to deposit a second layer, and the multilayered structure is created. These steps can be continued until the desired thickness is achieved (de Villiers et al., 2011).

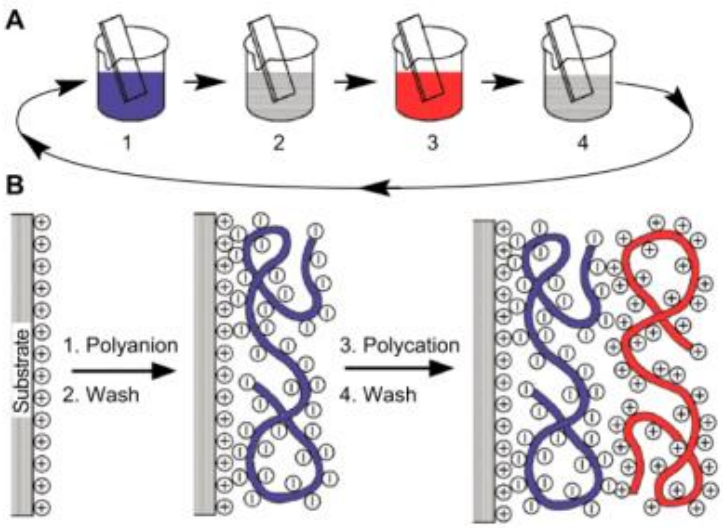

Fig. 19: (A) Schematic illustration of immersive LbL assembly on a planar substrate using oppositely charged polymers, (B) the charge characteristics of the films after each deposition step (de Villiers et al., 2011).

Some LbL methods don't need washing cycles, which greatly reduces assembly time. Polyelectrolytes or colloids with a high linear surface charge density are used excessively to prime the substrate. As a result, in comparison to the layer before it, an excess of charge that is not stoichiometric is absorbed after each step. This excess of charge acts as a step-by-step mechanism for the polarity of the surface charge to be reversed, creating an ideal surface for the adhesion of the succeeding layer. Covalent or click

chemistry methods, which do not rely on intermolecular interactions, were developed to create stable or biodegradable multilayered structures. But the sequential stacking approach still holds (de Villiers et al., 2011).

3.3 Assembly methods for LbL construction

The assembly method used in the LbL process affects significantly the physicochemical characteristics of assembled films, such as thickness, homogeneity, and inter- and intralayer film organisation, in addition to the process properties (such as time, scalability, and manual intervention). Numerous assembly techniques, including dip-coating, spin-coating, spraying, and perfusion, have been developed since the LbL process was first introduced to create multilayer films.

3.3.1 Immersive Assembly (dip-coating)

Immersive Assembly (Fig. 20) is a traditional method of LbL that consists of the manual immersion of planar substrates in solutions of the layering materials, followed by washing. Similarly, particulate substrates can be coated using immersion-based approaches; however, the substrate must be collected by centrifugation between a deposition step and the subsequent washing step (Xiao et al., 2016).

Manual assembly on planar substrates

Immersive assembly, in which the substrate is successively submerged into polymer solutions for deposition with washing procedures in between the deposition processes, is the usual traditional approach for LbL assembly on planar substrates. During these early stages, it was discovered that LbL assembly produced more homogeneous films than techniques such as gas deposition and nucleation deposition. Other studies have shown that the salt concentration and pH of the deposition solution, the concentration of the layering material, the immersion time, the washing parameters, and other factors can influence the growth of the film. The ideal absorption time for the deposition of the material on the previous layer is about 12 minutes. This time requirement for optimal deposition represents one of the main large-scale limitations of this method (Richardson et al., 2016).

Manual assembly on particulate substrates

Traditionally, immersion LbL assembly on particle substrates needs a separating step between the deposition and washing processes. For solid particulate substrates, this is often accomplished by centrifugation.

Centrifugation may produce aggregation and can be challenging to automate; therefore attempts to avoid it have been a primary driving force behind the development of innovative approaches for immersive LbL assembly on particulate substrates. One method, for instance, employs solvent exchange stages between the layer deposition and centrifugation phases to lessen the agglomeration of tiny particle substrates during washing.

One of the main requirements for this method is the high concentration of the polymer solution, which contains orders of magnitude more coating material than what is needed to coat the particles. If precise amounts of saturating polymer are added, washing procedures are not necessary, but if the zeta-potential is not constantly maintained, this can result in aggregation; moreover, utilising sonication during layer deposition can also aid in preventing aggregation when using this technique, also known as the saturation method (Richardson et al., 2016).

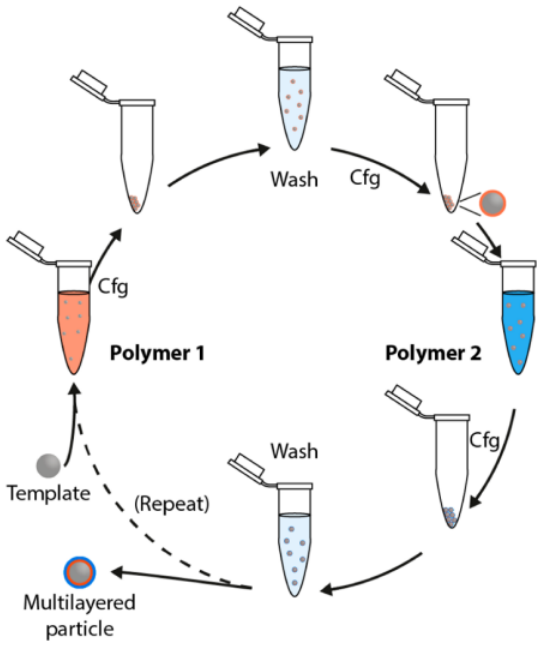

Fig. 20: Schematic illustration of immersive assembly on particulate substrates using centrifugation in between washing steps (Richardson et al., 2016).

3.3.2 Spin assembly

One of the earliest technologies to be used for LbL assembly was the widely used and industrially applicable coating process known as "spin coating," which uses a spinning substrate to aid coating and drying (Fig. 21). Although spin drying following immersive

LbL assembly can be used, the bulk of spin LbL assembly is carried out by casting the solution onto a spinning substrate or onto a stationary substrate that is then spun. With the spin coating, it is possible, in the case of polymers, to obtain thinner films. This is because the spinning process results in a more homogeneous film due to electrostatic interactions, viscous and centrifugal forces, and air share. The spin assembly procedure is automatable by integrating injection systems with rotating substrates and is relevant for several different applications (Richardson et al., 2016).

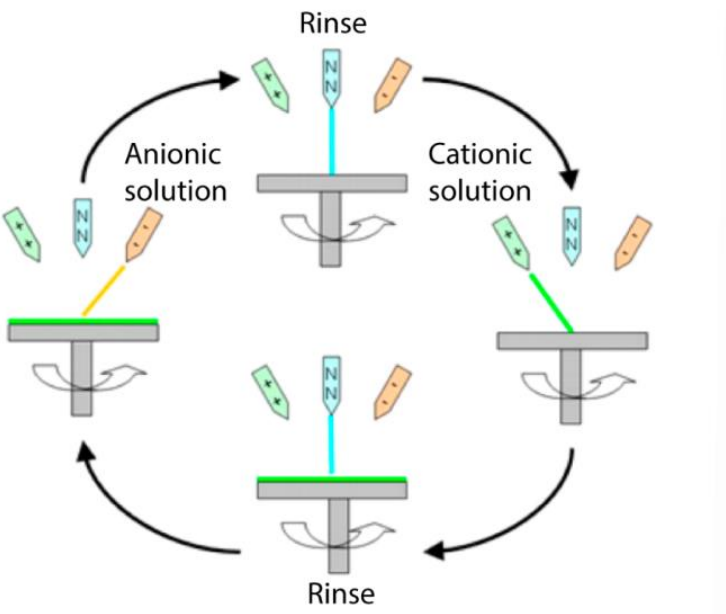

Fig. 21: Schematic illustration of spin, assembly using an automatic injection system (Richardson et al., 2016).

3.3.3 Spray assembly

Instead of dipping a solid substrate into the target component's solution, Schlenoff et al. sprayed the solution of the component, such as polyelectrolytes, with an intermediate rinsing by spraying water. They showed the creation of polyelectrolyte LbL multilayer films made from poly (styrenesulfonate) and poly (diallyldimethy-lammonium chloride), and this spraying technique allowed for the quick creation of LbL films over a vast area while retaining high uniformity and excellent quality (Fig. 22).

In a systematic study, Decher and coworkers compared LbL films made using the traditional dipping procedure with those made using the spraying approach under a variety of circumstances, such as component concentrations, spraying times, and drying times between deposits. They discovered that, despite the extremely quick assembly operations using the spraying LbL approach, the LbL films' thickness nevertheless rose

linearly with the number of deposition cycles, much like traditional dipping. Furthermore, using AFM and X-ray reflectometry, it was proven that the films made using the spraying LbL technique had reduced surface roughness. In practice, the quality of the LbL films made using the spraying approach, which required only 60 seconds for each layer, was equivalent to or better than that made by dipping a LbL film, which required 1520 seconds per layer, suggesting a 25-fold acceleration in the process of making LbL films. The acceleration in film preparation rose by a factor of more than 250 compared to dipping for LbL films of an acceptable grade (Xiao et al., 2016).

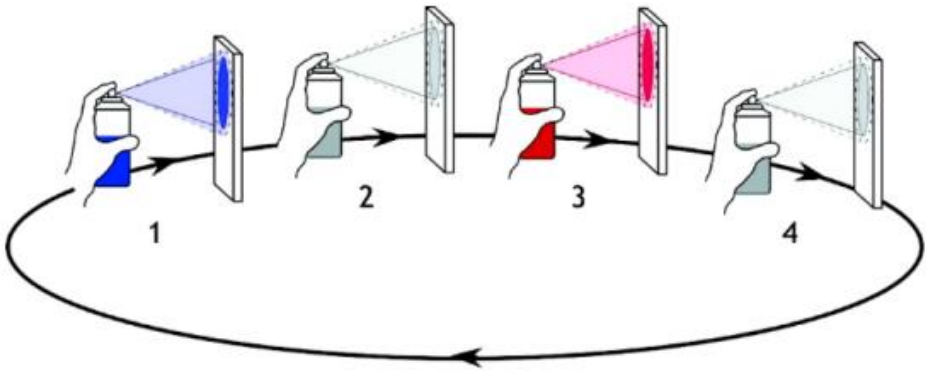

Fig. 22: Schematic illustration of manual spray assembly using polymer solutions (Xiao et al., 2016).

3.3.4 Fluidic Assembly

Flow-based assembly is used to deposit multilayers using fluidic channels (Fig. 23). In this case, to form the multilayer, the rinse and polymer solution is pushed through capillaries. Alternatively, the capillaries are manually coated with the polymer and rinse solution using pipetting or a pump, and the solution is then vacuumed out (Richardson et al., 2016). This makes fluidic assembly a valid alternative for centrifugation-free assembly on particle substrates. Moreover, it is a technique that can be used to coat surfaces that are not easily accessible with other methods. A limitation related to the use of fluidic assembly is the need for specialized equipment and expertise to build up fluidic systems, but the unique advantages of this technique make it extremely interesting for a different range of possible applications (Xiao et al., 2016).

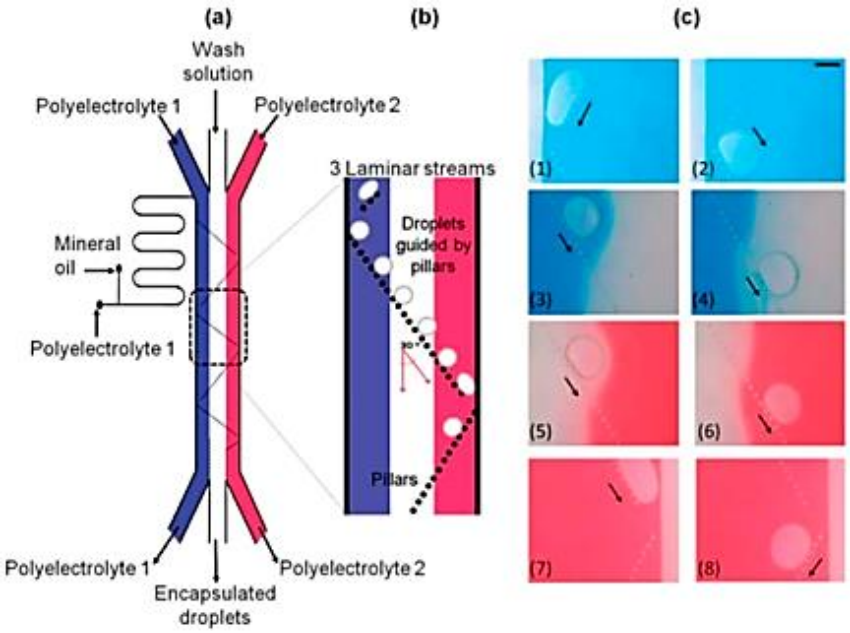

Fig. 23: Schematic illustration of fluidic assembly on particulate substrates using zigzag pillars to direct droplets back and forth between polymer solutions (Xiao et al., 2016).

3.3.5 Electromagnetic Assembly

In electromagnetic assembly (Fig. 24), a magnetic or electric field is applied to create a multilayer film. In a standard set-up, two electrodes are immersed in a polyelectrolyte solution and, by applying an electric current, electrodeposition occurs. Subsequently, the electrodes are rinsed and immersed in a solution of polyelectrolytes solution, of opposite charge. The process is repeated as many times as desired to obtain the required thickness. The electromagnetic assembly allows for the quick assembly of ions, polymers, and colloids. Moreover, the magnetic effect facilitates the deposition of multilayers on sensitive particulates or small templates that have difficulty being centrifuged (Xiao et al., 2016).

3.4 Parameters controlling the LbL assembly process

The structures of LbL-constructed multilayer thin films may be significantly influenced by a variety of variables, such as pH temperature, ionic strength, electrolyte type, solvent, and properties of PEs, such as charge density, molecular weight, concentration, and architecture (Richardson et al., 2016).

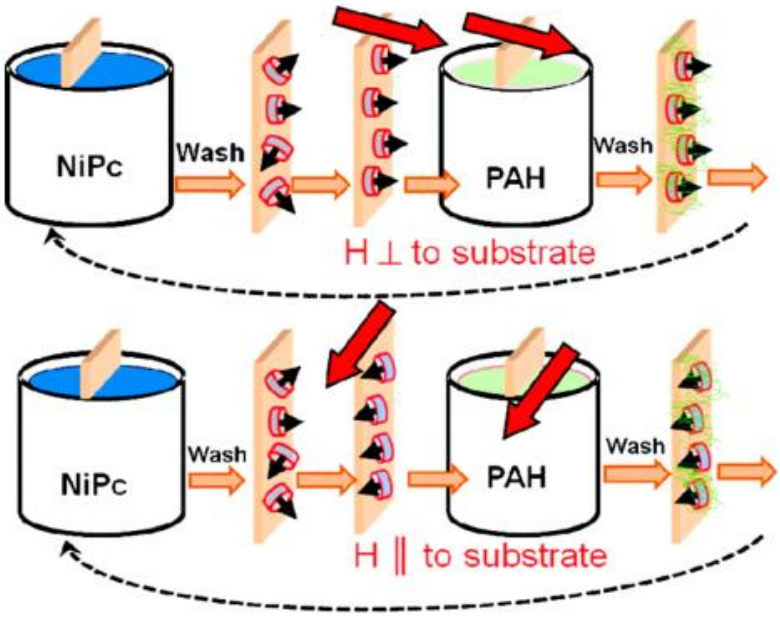

Fig. 24: Schematic illustration of the magnetic assembly of nanoparticles using differently aligned magnetic fields (Richardson et al., 2016).

3.4.1 pH

The composition, structure, and cross-link density of hierarchical nanostructures or LbL multilayer thin films are significantly influenced by the pH of a solution, mostly due to differences in the degree of PE ionisation under various pH conditions. While weak PEs with carboxylic acid or amine functional groups are highly sensitive to the pH of the external solution, strong PEs with substantial charges are fully charged independently of pH. For weak PEs, pH can be used to control the amount of nonionized carboxylic acid groups on the surface or within the multilayer film (Richardson et al., 2016).

3.4.2 Temperature

It has been explicitly investigated how temperature affects the stability, internal structure, and thickness of LbL multilayer assemblies. The swelling of the films and enhanced interpenetration between PE layers caused multilayer thin films built at high temperatures to be generally thicker than equivalent films manufactured under ambient circumstances, as demonstrated by prior research. The fact that temperature has a consistent impact on the stability and development of LbL-constructed multilayer thin films in both 2D and 3D assemblies is also noteworthy (Richardson et al., 2016).

3.4.3 Ionic strength

Another important parameter that significantly influences the stability, permeability and development of LbL multilayer systems has been identified as ionic strength. Numerous studies have explicitly investigated the relationship between salt type and concentration and the thickness of multilayer films during the past 20 years. As a result of the conformational transition of PE solution from the extended rod to the globular coil at low and high salt concentrations, respectively, it was discovered that significant differences were observed within the multilayer thin films assembled in the solutions with low and high salt concentrations. This led to different internal structures for multilayers (Richardson et al., 2016).

3.4.4 Solvent

The solvent environment has a significant impact on the structure of PEs and the formation of multilayer thin films or nanostructures. By changing the quantity of ethanol in the aqueous PE solutions, Poptoshev and colleagues investigated the impact of solvent quality on the formation and structure of PE multilayer thin films made of PSS and PAH. Their findings indicated that increasing the quantity of ethanol while reducing the solvent quality resulted in an increase in film thickness and mass loading, which was perhaps caused by the diminished solvating impact of aqueous solutions containing electrolyte ions. Therefore, choosing a suitable solvent to create PE solutions is highly recommended for effective LbL assembly building (Richardson et al., 2016).

3.4.5 Properties of PEs

Recent studies have analysed how the molecular weight (MW) of PEs affects the structure of multilayer PE films containing mobile polymer chains. The findings showed that an increase in polycation MW led to an increase in the internal roughness of multilayer films and that polyanion MW could accurately regulate the swelling and dissociation characteristics of multilayer films in response to pH. Further research showed that adjustable control over the MW of PEs might prevent the need for time-consuming post-treatment processes that would cause disassembly between internal deposition layers when fabricating multilayer films. In addition, PE chain topologies, such as chain conformation and chain interpenetration, can influence how PE multilayer thin films develop (Richardson et al., 2016).

3.5 Characterization of films on particulate substrates

In contrast to planar substrates, which are easier to handle and treat, particulate substrates (Fig. 25) provide several special benefits for the characterisation of thin films. For instance, measurement of the charge reversal associated with LbL assembly is made simple by the use of particulate substrates. Additionally, methods based on microscopy can make it simple to see how thin a coating is and how permeable it is. Particulate substrates can also be employed with another diffusion- and light-based approaches (Richardson et al., 2016).

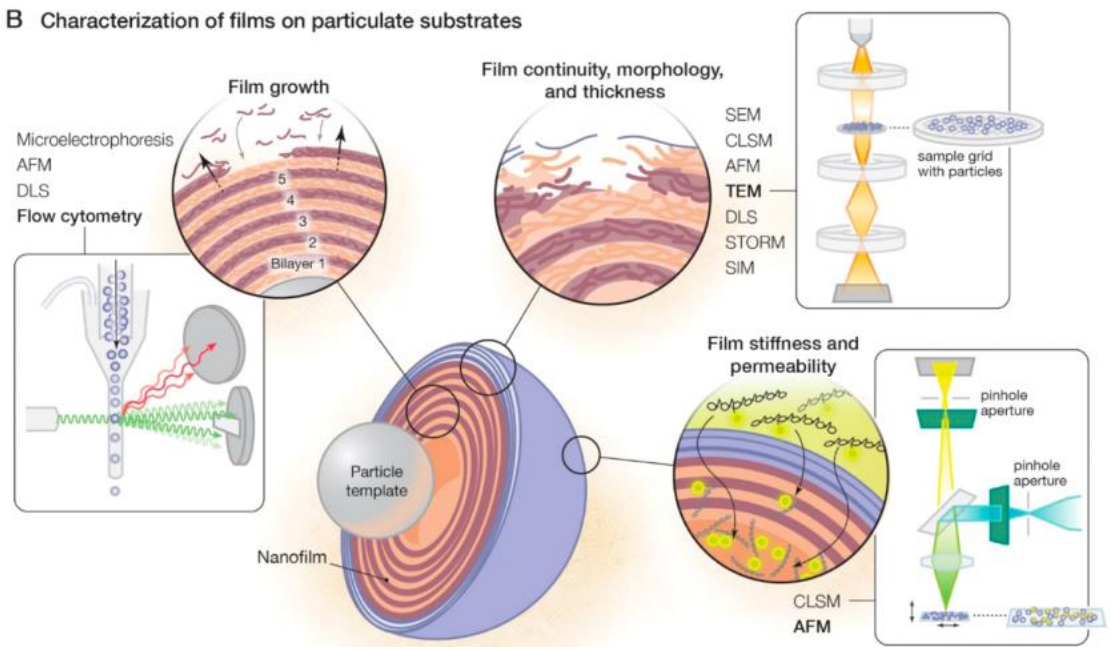

Fig. 25: Characterization of films on particulate substrates (Richardson et al., 2016)..

3.5.1 Assessing film growth

Microelectrophoresis is one of the most commonly used methods to monitor the LbL assembly process on the particulate substrate, which allows the evaluation of zeta-potentials. When polymers are deposited on particles, flow cytometry may be used to track the process since the number of layers results in more scattered light or fluorescence (in the case of fluorescently tagged polymers). Polymer films can alter the scattering characteristics, and their larger size can result in less Brownian motion. The dispersion of doublets, triplets, or bigger aggregates is greater than that of single particles; hence, both flow cytometry and DLS may be used to evaluate particle

aggregation during stacking. Aside from DLS, LbL assembly on dense particles may be seen using TEM after each layer, and the film growth can be calculated using the contrast difference between the particulate substrate and the film (Richardson et al., 2016).

3.5.2 Examining film morphology

AFM, SEM, and TEM allow for the evaluation of the morphology and thickness of LbL films. In the case of thin films, to study these characteristics, one generally proceeds first by removing the particulate substrate on which the films have been deposited, obtaining hollow capsules.

When imaging capsules (greater than 500 nm) with strong interference contrast, differential interference contrast (DIC) microscopy is used. Comparably, capsules made of luminous building blocks may be studied using fluorescence microscopy (like CLSM). Super-resolution microscopy methods that are modern. Recent studies have employed relatively new techniques to photograph smaller capsules (50 nm in diameter) and assess their nanostructure. Examples of these techniques are stochastic optical reconstruction microscopy (STORM) and structured illumination microscopy (SIM) (Richardson et al., 2016).

3.5.3 Determining film stiffness and permeability

LbL capsules' mechanical characteristics may be studied by examining their swelling or by using an AFM to measure their deformation when under load. Particularly, many polymer LbL capsules have Young's modulus in an aqueous solution that falls between 1 and 100 MPa. During mechanical measurements, the in situ deformation of capsules in the presence of applied force may be seen using a combination of AFM and CLSM. Microfluidic chamber-based flow studies can be used to track the deformability of capsules. Using fluorescent small molecules, polymers (like dextran), or nanoparticles under various solution conditions, fluorescence microscopy (e.g., CLSM) may be used to study the permeability of films in capsule form (Richardson et al., 2016).

4 AIM AND OBJECTIVES

Aim: the main purpose of this work is to propose and conceptually validate a novel theranostic platform for PCa imaging and treatment. The nanosystem is characterized by an internal calcium phosphate (CaP) core covered by polyelectrolytes deposited through the LbL self-assembly process technique. LbL allows the incorporation of drugs (docetaxel and enzalutamide) and carbon quantum dots (CQDs), such as imaging probes, to provide a therapy to treat cancer, releasing the drug load in a controlled manner over a specific time interval. A small-molecule PSMA ligand, PSMA-617, is linked to the outermost layer of the nanosystem to promote active targeting of tumor cells. The following objectives have been stated to fulfil the main thesis aim:

Objective 1: synthesis of chitin-derived CQDs and analysis of their chemical, physical, optical characteristics, cytocompatibility.

Objective 2: to develop and optimise nano theranostics system with a CaP core containing docetaxel (DTX), stabilising it by PAH deposition via a pumping method, and then functionalizing it with enzalutamide (ENZ), DTX, and CQDs via their encapsulation in LbL.

Objective 3: use of the LbL self-assembly process to coat the CaP core with chitosan (CHI) and furcellaran (FUR), as polyelectrolytes, to create a nanotheranostic drug delivery system for DTX and ENZ.

Objective 4: conjugation of PSMA-617 to the outer layer of the system to promote active tumor targeting.

Objective 5: characterization of NPs produced through chemical-physical, morphological, with a focus on the layers' ability to encapsulate and release drugs and CQDs.

Objective 6: to assess the efficacy of the proposed treatment and the uptake of NPs by cancer cells, different NP were tested for cytotoxicity on prostatic cancer cells (LNCaP, VCaP).

Table 6: Summary of the theranostic specifics and design of the nanoplatform.

	CHALLENGES	SPECIFICATIONS	VALUE/DETAILS
Core	Biocompatibility, Size	CaP	Size: ~100nm Surface charge: positive
Layer-by-layer	Biocompatibility, pH-responsive, passive targeting and EPR effect, drug release, size	Polyelectrolytes (polyanion/polycation): CHI FUR	pH operativity: acidic conditions particle size: ~200nm
Drugs and biomolecules	Biocompatibility, load efficiency	Docetaxel (DTX) Enzalutamide (ENZ)	DTX: 1.5mL DTX in PBS: DMSO (1:1) solution in the second and fourth layers. ENZ: 2.5mL ENZ in DMSO in the second and fourth layers.
External coating	Biocompatibility, Immune system stealth strategy, Increase circulation time	CHI	-
External surface functionalization	External probes, active targeting, tumor specificity, bioactivity	PSMA-617	Active targeting on cancer cells
Imaging	Imaging-guided tumor targeting therapy	CQDs	Chtin-derived QDs
Therapeutic Mode	Monomodal therapy	Chemotherapy	-

5 EXPERIMENTAL SECTION

5.1 Materials

In this study, to obtain the core of CaP nanoparticles, Calcium L-lactate hydrate (≥98.0%, Mw=218.22 Da), Ammonium phosphate dibasic (Mw=132.06 Da), Poly(allylamine hydrochloride) (PAH) (Mw =15 000 Da), and Docetaxel trihydrate (DTX) (Mw=861.93 Da) were purchased from Sigma-Aldrich (Gillingham, Dorset, SP8 4XT, UK). For the LbL process, Chitosan (CHI) (low molecular weight, 75% deacetylated), was purchased from Sigma-Aldrich, Furcellaran, manufactured by neutral aqueous extraction from Baltic Sea seaweed *Furcellaria lumbricalis,* was purchased from Biosynth Carbosynth (UK). The drugs encapsulated in the layers were DTX, dissolved in a solution of Dulbecco's phosphate-buffered saline (PBS; Sigma Life Science) and Dimethyl sulfoxide (DMSO) (Hybri-Max™, sterile-filtered, BioReagent, suitable for hybridoma, ≥99.7%), and Enzalutamide (ENZ) (50mg, Mw=464.4 Da), dissolved in a solution of DMSO. ENZ was purchased from Stratech (UK). The NPs obtained are targeted using Vipivotide tetraxetan (PSMA-617) (Mw=1042.14 Da), which was purchased from MedChemExpress (MCE). N-Ethyl-N'-(3-(dimethylamino)propyl)carbodiimide hydrochloride (EDC) (98%), N-hydroxysuccinimide (NHS) (98%), were obtained from Sigma Aldrich (UK). Other materials used included Hydrochloric acid (HCl) (reagent grade 37%), (Sigma-Aldrich, UK), Sodium acetate (Mw=82.03 Da) and Glacial Acetic Acid (100%) (Mw=60.05 Da), deionized water (dH_2O). Cellulose membrane in dialysis tube (typical cut-off of Mw=14,000 Da) and 0.22 µm filter papers were used according to the manufacturer's instructions.

5.2 Methods

5.2.1 Synthesis of CQDs from chitin (CHBOCQDs)

The "pyrolysis carbonization method" was used to produce the CQDs (Fig. 26). This method involves two steps: pyrolysis, which converts biomass waste into bio-oil products, and hydrothermal carbonization (HTC), which produces CQDs from the products of the preceding reaction.

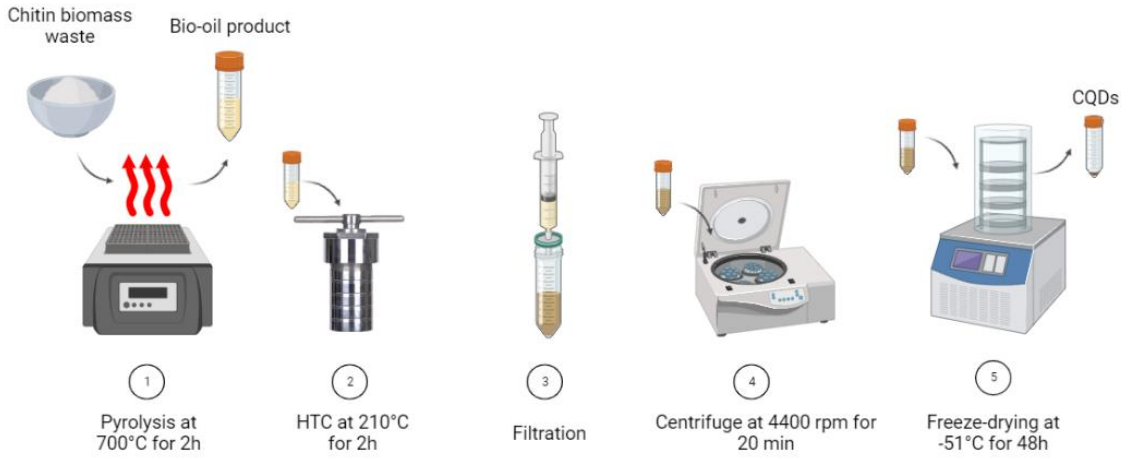

Fig. 24: Synthesis process of CQDs

Chitin (CH) biomasses were employed as carbon sources in the pyrolysis process to produce CQDs. First, the chitin biomasses were heated in a pyrolysis furnace at 700 °C for 2 hours in a N_2 atmosphere. Char-carbon and ash-based charcoal, as well as volatile materials, are produced during this process. The latter is made up of condensable vapours known as "pyrolysis oil", commonly referred to as bio-oil. To create a CQDs solution, the bio-oil samples were placed in a Teflon-lined stainless autoclave and incubated at 200 °C for 2 hours, in distilled water.

The subsequent purification step ensured that, after this reaction, the obtained samples consisted exclusively of CQDs. For this purpose, the samples were filtered using 0.22 µm filter paper and using a Buchner funnel to remove excess solids. Then, the samples were centrifugated at 400 rpm for 20 minutes, frozen at -20 °C, and then freeze-dried for 48 hours at -51 °C. The CQDs were stored in the fridge at 4°C.

5.2.2 Synthesis of LBL nanoparticles

5.2.2.1 Preparation of DTX-containing PHA-coated CaP nanoparticles

The core of the NPs was obtained following the protocol described by Urch et al. (2008) and Elizarova et al. (2016), making appropriate modifications.

The process, shown in Fig. 27, involves the use of a P-3 peristaltic pump (Pharmacia Fine Chemicals). Initially, 40 mL of an aqueous solution of calcium phosphate (24mM, pH 10) and ammonium phosphate (15mM, pH 10) are prepared separately, which will result in the formation of calcium phosphate nanoparticles. To the ammonium phosphate

solution is added DTX, previously dissolved in a solution of PBS: DMSO (1:1) with a concentration of 600 µM. Different amounts of DTX were tested (0, 150, 300, and 500 µL). In this way, the formation of CaP particles containing DTX is obtained. Then, 40 mL of an aqueous solution of PAH (1mg/mL, pH 10) was prepared and subsequently mixed with the previous two to obtain DTX-containing CaP coated with PAH.

Each of the three solutions was pumped through the corresponding silicone tube (3mm diameter) at a flow rate of 10 mL/min. The silicone tubes' geometric properties enable the production of the core and subsequent coating. In particular, the first 10 cm long tube allows the formation of DTX-containing CaP NPs, while the second 100 cm long tube allows the deposition of PAH on the surface of the CaP NPs. The NPs thus obtained were collected, stirred for 24h, collected again, and dialyzed against distilled water using a dialysis membrane for 12h.

Subsequently, the NPs were centrifuged at 4400 rpm for 20 min, the supernatant was removed and replaced with an equivalent volume of dH_2O. The NPs were sonicated for 2 minutes in an Ultrasonic Cleaner 1510 (Branson) before being freeze-dried for 72 hours for further testing. From this point on, DTX-containing and PHA-coated CaP NPs will be referred to as CaP NPs

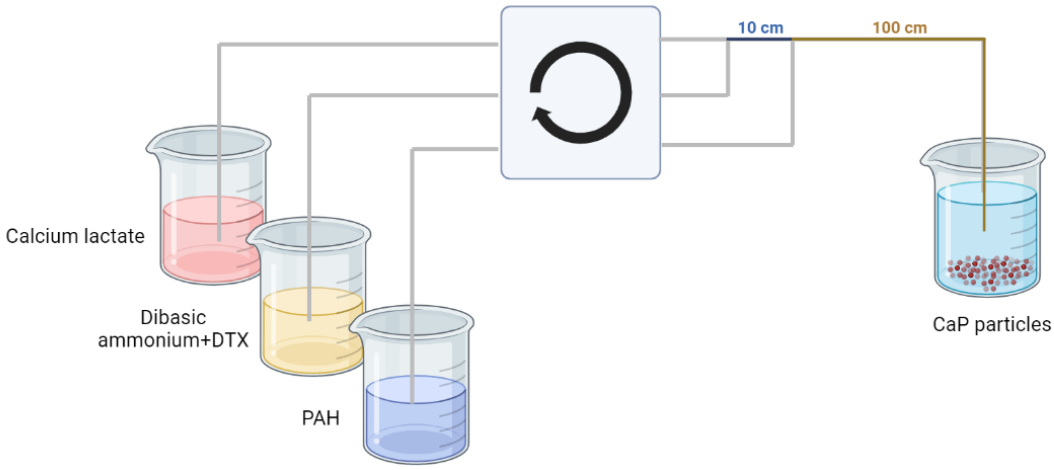

Fig. 27: Synthesis of DTX-containing PHA-coated CaP nanoparticles.

5.2.2.2 LBL deposition of aqueous solutions of polyelectrolyte on CaP NPs

The CHI and FUR concentrations were appropriately chosen to reach the saturation point of polyelectrolyte deposition on the CaP NPs.

CHI (1 mg/mL) and FUR (2 mg/mL) were prepared separately in 40 mL of dH_2O and heated at 50 °C for 1 h to obtain homogeneous mixtures. To improve the solubility of CHI, 1% (v/v) acetic acid was added. To increase the ionic strength of both polyelectrolytes, 750 µL of 0.005 M NaCl was added under constant magnetic stirring at 300 rpm. The charge of polyelectrolytes was evaluated using 0.1 M, 0.25 M, and 5 M HCl and NaOH and the optimal charge was found at pH 6. Fig. 28 shows the deposition process of successive layers of polyelectrolytes. The formation of the multilayers was accomplished by deposition of polyelectrolytes on each other (FUR/CHI/FUR/CHI) in a weight ratio of 1:1:3:3.

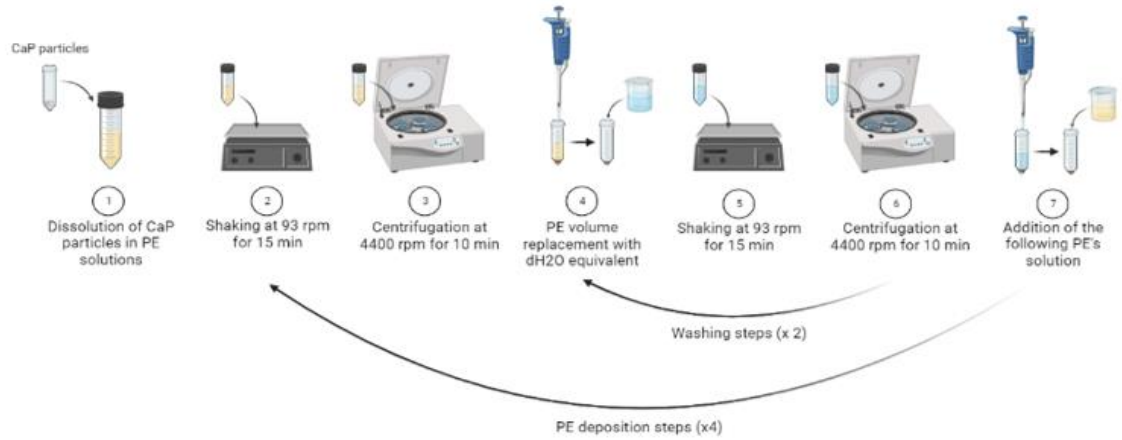

Fig. 28: LbL deposition process.

Precisely, the procedure involved dissolving 10 mg of freeze-dried CaP NPs in 10 mL of FUR solution and sonicating the mixture for 15 s. The NPs solution was shaken for 15 min at 95 rpm using an orbital shaker SSM1 (Cole Parmer/Stuart). Subsequently, the NPs were centrifuged at 4400 rpm for 10 min and two rinsing steps in dH2O were performed to remove excess polyelectrolyte. For the first rinsing step, the supernatant was removed, and replaced with 10 mL of dH2O; the NPs were sonicated for 15 s, shaken for 10 min at 95rpm and centrifuged for 5 min at 4400rpm. In the second rinsing step, the supernatant was removed and replaced with 10 mL of dH2O. The NPs were sonicated for 15s, shaken for 3 min at 95rpm and centrifuged for 10 min at 4400rpm. Before the last centrifugation, 100 µL of the NPs suspension was removed to analyze the corresponding ζ-potential. The deposition of the successive layers was performed in the same way as the one just described, with the only difference being that for the deposition of the last layer of CHI and FUR, the NPs were dispersed in a volume equal to 30mL of polyelectrolyte. After LBL assembly, the NPs were freeze-dried and stored in a vacuum desiccator for subsequent tests.

From this point forward, the CaP NPs systems on which multilayers of CHI and FUR without encapsulation of drugs have been deposited will be identified as "CaP - no drugs" (Fig. 29a).

5.2.2.3 LBL deposition of aqueous solutions of polyelectrolyte on CaP and incapsulation of ENZ

The procedure is similar to that described in the previous paragraph. The only difference is the incorporation of ENZ into the anionic layers of the final system. From a 9mM solution of ENZ in PBS, a 34uL aliquot was added to each solution of the anionic polyelectrolyte to create a FUR/ENZ solution.As in the previous system, a 100 uL aliquot of the functionalized NPs solution was used to measure the zeta potential. After the LBL assembly, the NPs were freeze-dried and stored in a vacuum desiccator for subsequent tests. From this point forward, the CaP NPs systems on which multilayers of CHI and FUR/ENZ have been deposited will be identified as "CaP - ENZ" (Fig. 29b).

5.2.2.4 LBL deposition of aqueous solutions of polyelectrolyte on CaP and incapsulation of ENZ and DTX

Also in this case the LBL procedure is similar to the previous cases. In addition to ENZ, DTX was incorporated into the layers of the system. A 34 µL aliquot of solution 600 µM of DTX in PBS:DMSO (1:1) and a 34 µL aliquot of ENZ solution were added to the aqueous solution of the anionic polyelectrolyte to create a FUR/ENZ/DTX solution.

A 100 uL aliquot of the functionalized NPs solution was used to measure the zeta potential. After LBL assembly, the NPs were freeze-dried and stored in a vacuum desiccator for subsequent tests.

From this point forward, the CaP NPs systems on which multilayers of CHI and FUR/ENZ/DTX have been deposited will be identified as "CaP - ENZ/DTX" (Fig. 29c).

5.2.2.5 Deposition of CQDs on CaP-no drugs, CaP-ENZ, and CaP- ENZ/DTX systems

In the final layer of deposition, 15 mg of a 500 µM solution of CHBOCQDs was added to the CHI solution for all synthesized systems. Fig 29 shows the schematic representations of the CaP-no drugs, CaP-ENZ, CaP-ENZ/DTX systems.

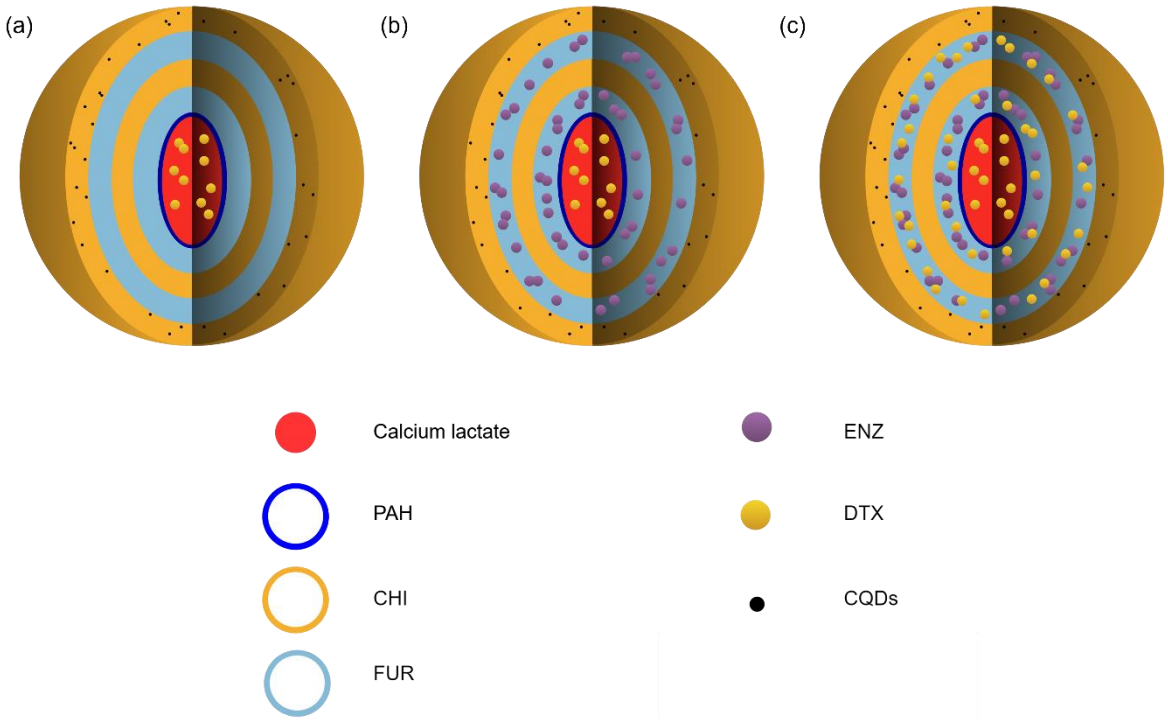

Fig. 29: Schematic representations of CaP-no drugs (a), CaP-ENZ (b), CaP-ENZ/DTX (c).

5.2.3 NPs surface modification with the PSMA-617

PSMA-617 was immobilized on the NPs (Fig. 30a) by modifying the protocol described by Chen et al.. PSMA-617-targeted NPs were synthesized by coupling PSMA-617 with chitosan (Fig. 30b). An amide bond was formed between the carboxyl groups of PSMA-617 and the residual amine groups in chitosan using 1-Ethyl-3-(3-dimethylaminopropyl) carbodiimide (EDC) and N-hydroxysuccinimide (NHS) as coupling agents. After dissolving PSMA-617 (100 µg) in 0.1 M 2-(N-morpholino)ethanesulfonic acid (MES) buffer (5mL), EDC (22 µg) and NHS (6.63 µg) were added to the PSMA-617 solution (molar ratio of PSMA-617: EDC: NHS = 1: 1.2: 0.6). The solution was incubated at room temperature for 30 min to activate the carboxyl groups of the PSMA-617. After 30 min of shaking at 80 rpm, the solution was added to the NPs solution dissolved in 0.1 M MES buffer (5 mL). The coupling reaction was carried out for 24 h at room temperature.

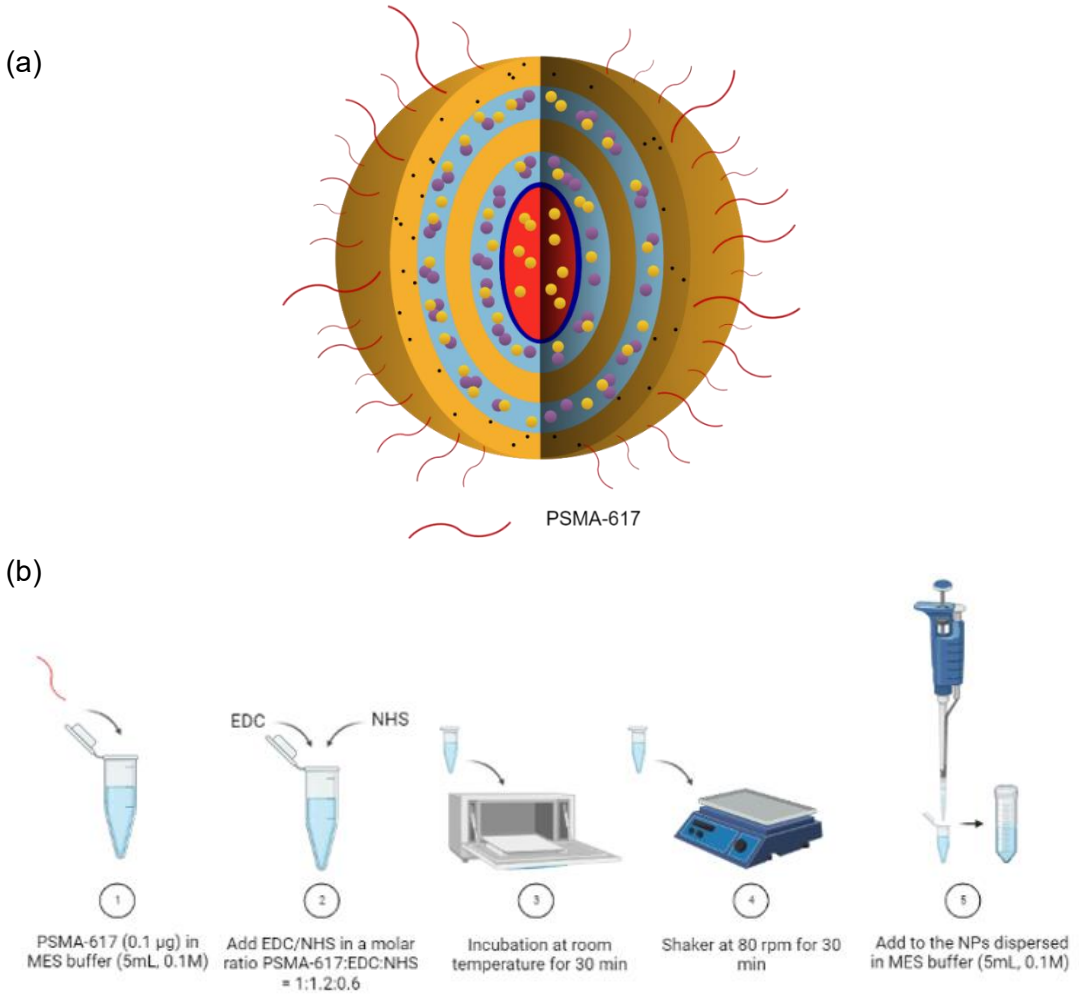

Fig. 30: (a) Schematic representations of CaP-ENZ/DTX+PSMA-617; (b) process of NPs surface modification with the PSMA-617 .

5.3 CQDs characterization methods

5.3.1 Physico-chemical characterization

5.3.1.1 UV-Vis analysy

A dual-beam UV-Vis spectrophotometer (Jenway 7315 spectrophotometer) was employed to study the light absorption patterns of aqueous solutions of CQDs, which were excited over a full wavelength range of 200-600 nm.

5.3.1.2 Fluorescence analysis

The fluorescence of the CQDs was analyzed using a UV lamp with a UV light of 12" at 300 nm and keeping the samples under the lamp.

5.3.2 Morphological characterization

5.3.2.1 High-resolution Transmission Electron Microscopy (HRTEM)

The morphology of the CQDs was evaluated using a Hitachi HT7800 120 kV TEM with cryo-capabilities using an EMSIS CMOS Xarosa camera. Samples were analyzed at a focus of as small as 50 nm.

5.3.3 Cytotoxicity evaluation

5.3.3.1 Cultivation of Neo-dermal fibroblast

Neo-dermal fibroblasts were used as the cell line to evaluate CQDs cytotoxicity. These were purchased from Sigma Life Science. Neo-dermal fibroblasts were grown in Dulbecco's Modified Eagle Medium (DMEM). The media were supplemented with 10% fetal bovine serum (FBS) and 5000 U/mL penicillin and streptomycin. The cells were maintained at 37 °C and 5% CO_2 in a humidified incubator.

5.3.3.2 PrestoBlue

The metabolic activity of the fibroblast cells was evaluated using the PrestoBlue™ assay. Neo-dermal fibroblasts were seeded onto 96-well plates at a density of 8000 cells per well. CQDs, previously solubilized in the medium, were added at different concentrations (10, 25, 50, 100, 250, 500, and 1000 µg/mL). Cell viability assays were performed after 24h and 48h of incubation of the fibroblasts with CQDs.

At these time points, the medium was removed from the wells and replaced with PBS pre-warmed at 37°C. The PrestoBlue™ reagent was diluted 1:10 with DMEM. To each well, 200 µL of the solution was added and incubated for 60 min at 37 °C and 5% CO_2. Then, 100 µL of solution from each well was transferred to a Greiner 96 F-bottom plate, and a FLUOstar Omega MicroPlate Reader (BMG Labtech) was used to measure the fluorescence (544 nm excitation, 590 nm emission).

The fluorescence values of each well were corrected by subtracting the mean fluorescence value obtained from the control wells, containing only the PrestoBlue™ reagent without the cells.The calculated values were adjusted by subtracting the mean

fluorescence of the control wells that contained just PrestoBlue solution. Data are displayed as viability (%) vs. of CQD concentrations (ug/mL). By comparing the fluorescence values of each sample with the average fluorescence values of the control cells, the percentage of viability was determined.

5.3.3.3 Live/Dead

The LIVE/DEAD kit was used to test the viability of neo-dermal fibroblasts. Cells were seeded into 96-well plates at 8000 cells per well and the same CQDs concentrations tested in paragraph 5.3.1.3.2 were used. Then, they were incubated for 24h and 48h at 37 °C in 5% CO_2. At each time point, the medium was removed and the cells were washed with PBS pre-warmed to 37°C. After removing the PBS, according to the manufacturer's instructions for the Live/Dead assay, the cells were double-stained with Calcein AM (1 µL per mL of PBS), which allows the detection of live cells, and Ethidium Homodimer-EthD1 (4 µL per mL of PBS), for the detection of dead cells, in PBS. The multiwell was incubated for 20 min at 37°C. Then, cells were observed using a EVOS M5000 (Thermo Fisher).

5.3.3.4 Immunostaining assay

The cellular morphology of Neo-dermal fibroblast was observed by staining the cytoskeleton with Actin RedTM 555 ReadyProbes Reagent (Thermo Fisher Scientific), and the nucleus was observed with 4,6-diamino-2-phenylindole (DAPI). Neo-dermal fibroblast were cultured, treated with CQDs and incubated for 24 h. Following incubation, control and treated cells were washed with PBS and fixed with 4 % paraformaldehyde (50uL) overnight at 4°C. The next day cells were washed twice with PBS and permeabilised using 0.1% (v/v) Tweem20® (Sigma, Life Science). 50 uL of the ActinRed solution (2 drops of ActinRed reagent per mL of PBS) were placed in each sample for 20 min at room temperature, protected from light. Then, the samples were washed twice with 0.1% (v/v) Tween20®/PBS to remove residues of ActinRed. Following this, the samples were stained DAPI solution (1 drop of DAPI solution in each well) for 10 min at room temperature protected from light. Subsequently, samples were washed twice with 0.1% PBS and were examined under fluorescent microscope (EVOS M5000, Thermo Fisher).

5.4 NPs characterization methods

5.4.1 Morphological characterization

5.4.1.1 Size and shape NPs

To determine the size and shape of the NPs, Transmission Electron Microscopy (TEM) was performed with a Philips CM 100 Compustage (FEI) transmission electron microscope (Philips) at HV = 100.0 kV, and digital images were captured using an AMT CCD camera with a magnification range of 130, 000×. Samples were prepared by drop-casting (10 µL) aqueous solutions of nanoparticles on copper grids (Scientific Agar) and dried for 20s before images were collected.

5.4.2 Physico-chemical characterization

5.4.2.1 ζ-Potential Evaluation

The ζ-potential of the different formulations of NPs was evaluated by a micro electrophoretic method using a Zetasizer Nano ZS Instrument (Malvern Panalytical, Ltd.). The ζ -potential was calculated using Henry's equation (Eq. 1):

$$\zeta = \frac{3\eta}{2\varepsilon F(\kappa\alpha)}\mu \quad (Eq.1)$$

where η is the dynamic viscosity, ε is the dielectric constant of water, F(κα) is the function of the dimensionless parameter F(κα), κ^{-1} is the electrostatic double layer thickness, which depends on *k* the Boltzmann constant, *e* the elementary charge, T the absolute temperature, I the ionic strength, c. All measurements were carried out at room temperature.

To measure the ζ-potential, aliquots of 200uL of each formulation were diluted in 600uL of dH_2O. The samples were read with refraction and absorption indexes of 1.700 and 0.010 respectively, the viscosity of the solvent was calculated from water (0.8872) and detection angle of 173° Each measurement was performed after a maximum of 100 runs. Three measurements were obtained for each sample, and the average values are presented in the following chapter.

5.4.2.2 Fourier Transform Infrared spectroscopy (FTIR-ATR)

FTIR spectroscopy of CaP, CaP - no drugs, CaP - ENZ, CaP - ENZ/DTX NPs, CHI and FUR samples were analyzed using a Spectrum Two PE instrument equipped with a

horizontal attenuated total reflectance (ATR) crystal (ZnSe) (PerkinElmer Inc., USA). For this analysis all NPs formulations were lyophilized. All samples were analyzed over a range of 4000 to 550 cm^{-1} with resolutions of 2 cm^{-1}.

5.4.2.3 X-ray photoelectron spectroscopy (XPS) analysis

XPS analysis of CaP, CaP - no drugs, CaP - ENZ, CaP - ENZ/DTX NPs were performed using a scanning microprobe Kratos Axis UltraDLD XPS spectrometer (EPSRC Harwell XPS Service Cardiff, UK), equipped with a monochromatic AlKα X-ray radiation source. Prior to XPS analysis, all samples were thoroughly freeze-dried. The base pressure in analysis chamber was 10−9 mbar. Samples were analysed in High 9596 Power mode with an X-ray take-off angle of 45° (scanned size∼1400 × 200 μm). Survey scans (Fixed Analyser Transmission mode, binding energy (BE) range 0–1200 eV, pass energy 117.4 eV) and high-resolution spectra (FAT mode, pass energy 29.35 eV) were acquired of C1s for each specimen,. Atomic concentration (At.%) on the survey scan was performed using the built-in CasaXPS software package and in order to detect the Binding Energy (BE) representing the chemical binding states of the each elements within the films, the XPS spectra for the chemical elements detected from the films were subjected to peak deconvolution using the same software.

5.4.2.4 Process Yield (Y)

To measure the amount of CaP particles produced compared with the initial amount of materials employed, Eq.2 was used:

$$Yield\ (\%) = \frac{(weight\ of\ the\ formulation)}{(weight\ of\ polymers + weight\ of\ drug + weight\ of\ other\ components)}\ x\ 100 \quad (Eq.2)$$

To measure the yield all formulations were previously freeze-dried.

5.4.2.5 Effectiveness of encapsulation of DTX in the core of CaP NPs

The CaP particles were frozen and freeze-dried to produce the dried products. The greater solubility of the CaP particles under alkaline conditions was used to calculate the encapsulation effectiveness. The procedure is divided into two steps: the first involves the use of a solvent to solubilize both the polymers and the drug, and the second involves the use of a solvent that only solubilizes the drug.

Lyophilized CaP (1 mg) was dissolved in HCl (3 mL, 1M) and stirred at 120°C until the acid had evaporated completely. At the end of this step, pellets of drugs and polymers were obtained. Subsequently, the pellet was dispersed in a 600 μL solution of ethanol

and water (3:1), soluble exclusively in the drug. The solution was stirred for 5h and centrifuged at 13,000 rpm for 10 min. Finally, 100 µL of supernatant was collected and transferred to a 96-well plate. The optical densities of the samples were analyzed using a FLUOstar Omega Microplate Reader (BMG Labtech).

The absorbance of the samples was calculated by subtracting the mean absorbance value of the wells containing the blank (ethanol/water solution).

For each sample, the DTX concentration, expressed in µg/mL, was calculated using a calibration curve. The encapsulation efficiencies of DTX in the CaP particle core was calculated as follows (Eq.3):

$$EE\ (\%)\frac{amount\ of\ drug\ in\ nanoparticles}{amount\ of\ drug\ supplied}\ 100 \qquad (Eq.3)$$

5.4.2.6 Drug release of DTX from CaP core

To determine the drug release profile, 1.5 mg of CaP particles were weighed, dispersed in 1 mL PBS, and incubated at 37°C for up to 6 days. The amount of drug released was measured at the following time points:10 min, 30 min, 3h, 4h, 6h, 1 d, 2 d, and 6 d.

At each step, 100 µL of the supernatant was taken in triplicate from the CaP particle solution. The optical density of the solution was measured at 228 nm for the DTX using a plate reader. For each time point analyzed, the effective absorbance was calculated by subtracting from the values obtained the mean value of the wells containing only the blank (PBS) for each standard and each sample. The DTX calibration curve was used to calculate the concentration of DTC released at each time point (µg/mL). Finally, starting from the concentration value released in the withdrawn aliquot, the amount of DTX released by the initial quantity of 1.5 mg of CaP particles was measured.

At each time point, the entire volume of PBS was withdrawn and replaced with an equal volume of PBS to achieve zero drug release in the next step.

5.4.2.7 Encapsulation of CQDs

A Shimadzu RF-6000 spectrofluorophotometer excited the particle solution with the encapsulated CQDs on a wavelength range from 200 nm to 250 nm. The emission was then analyzed and plotted.

5.4.3 Cytotoxicity evaluation

5.4.3.1 Cell cultures

VCaP (androgen receptor-positive, androgen-sensitive) and LNCaP (androgen receptor-positive, androgen-dependent) were kindly provided by the Newcastle University Center for Cancer. VCaP cells were cultured in DMEM with HEPES containing 10% FBS, 5000 U/mL penicillin-streptomycin, and 1% L-glutamine. LNCaP cells were cultured in RPMI 1640 with the same supplements. Cells were grown in an incubator at 37°C with 5% CO2 and 95% humidity. For different passages, the cells were washed with PBS, followed by the addition of trypsin–EDTA and incubation for 5 min. Subculturing was performed based on the density of the cells. Typically, for VCaP cells, subculture was performed once per week at 1/3 dilution; LNCaP cells were divided twice per week at 1/5 dilution.

5.4.3.2 Spheroid formation

5.4.3.2.1 Hanging drop method

LNCaP cells were used to create spheroids with the traditional hanging drop technique. Cells were cultured in the appropriate complete growth medium for at least three days in standard T75 flasks to reach approximately 70% confluency. Starting from a monolayer of cells, a suspension of cells was obtained and the cell count was determined. Drops of cell suspension (20 µL) containing 3000 cells were pipetted onto the lid of 150 dishes and inverted over dishes containing 15 mL of PBS. Hanging-drop cultures were incubated for 24 h under standard culture conditions (5% CO_2, 37 °C). After 24h, the drops were inspected under a microscope to assess spheroid formation.

The spheroids formed were transferred to a U-bottom 96-multiwell. Initially, 90 µL of the growth medium was added to each well. To reduce the effect of uneven evaporation on spheroid formation, the edge wells of the plates were not used and filled with PBS. The lid on which the drops containing the spheroids were present was slightly inclined, which allowed the spheroids to move towards the bottom of the drops and, in this way, it was easier to extract them. The spheroids were gently harvested using a P200 pipette and transferred to a single well of a 96-well plate for treatment and imaging.

5.4.3.2.2 U-bottom method

In this case, spheroids were obtained by combining two traditional techniques: the low attachment method with minor modifications and the use of methylcellulose as a viscosity inducer in the medium.

Both VCaP and LNCaP cells were used to generate spheroids. Cells were grown in an appropriate complete growth medium, as previously described. A cell suspension was obtained from a monolayer of VCaP and LNCaP cells. It is important to ensure that a homogeneous cell suspension (single cells) is obtained and that it does not contain aggregates, as this determines the size and uniformity of the spheroids. The VCaP and LNCaP suspensions were diluted with complete growth medium to obtain the final density and dispensed into Costar UltraLow Attachment 96 plates with a density ranging from 1000 to 100000 cells/well in DMEM cultures for VCaP and RPMI1640 cultures for LNCaP. Some wells were supplemented with 0.25% methylcellulose in DMEM or RPMI1640, as previously described. The protocol is illustrated in Fig. 31. The multiwells were incubated under standard culture conditions (5% CO_2, 37 °C), with 50% of the culture media every 48 h.

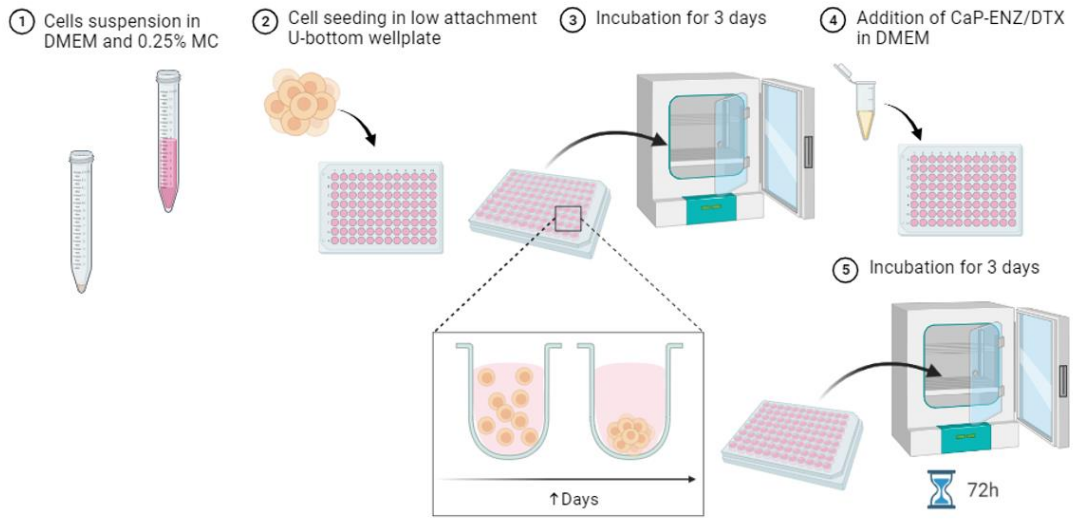

Fig. 31: Protocol for the synthesis of spheroids.

5.4.3.3 PrestoBlue

The PrestoBlue assay was performed to test the cell viability, in which a non-fluorescent blue compound called resazurin in the PrestoBlue® reagent can be reduced by living cells to resorufin, exhibiting strong red fluorescence.

The cytotoxicity of free DTX, free ENZ, CaP-no drugs, CaP-ENZ, and Cap-DTX/ENZ in VCaP and LNCaP cells was studied using the following method. First, the analysis was performed on 2D model (Fig.32). VCaP and LNCaP cells were seeded in a 96-well plate (cellular density: 8000/15000 cells per well) and medium containing NPs at concentrations ranging from 100 to 2000 µg/mL or free drug was added (Table 7). Cells

were cultured at 37 °C and 5% CO2. After 24 h, the culture medium was removed and the cells were washed once with PBS to remove excess NPs. PrestoBlue reagent diluted with DMEM or RPMI1640 was then added to each well and incubated at 37 °C under 5% CO2. At the same time, PrestoBlue® reagent diluted with DMEM or RPMI1640 was also added to blank wells without cells as the control. After 1 h of incubation, 100 µL of each well solution was transferred to a white bottom 96-well plate and a FLUOstar Omega MicroPlate Reader (BMG Labtech) was used to measure the fluorescence (560 nm excitation and 590 nm emission). All the samples were tested in triplicate. Cells not treated with NPs were used as controls. In the same way, the analysis was conducted on the 3D model of spheroid. (25000 cells/well).The obtained values were corrected by subtracting the average fluorescence of control wells with only PrestoBlue solution. Results are shown as viability (%) vs. concentration of NPs (µg/mL). Percent viability was obtained by relating the value in fluorescence of each sample with the average fluorescence values of control cells (which were not treated).

Table 7: Sample analyzed to test cell viability.

SAMPLE	CONCENTRATION
CaP-no drugs	100,250,500,1000,2000 ug/mL
CaP_ENZ	100,250,500,1000,2000 ug/mL
CaP-DTX/ENZ #1	100,250,500,1000,2000 ug/mL
CaP-DTX/ENZ #2	100,250,500,1000,2000 ug/mL
CaP-DTX/ENZ #3	100,250,500,1000,2000 ug/mL
Free DTX	10 uL
Free ENZ	10 uL

5.4.3.5 Live/Dead

The LIVE/DEAD kit was used to test the viability of the LNCaP and VCaP cells both on 2D and 3D model cells. VCaP and LNCaP cells were seeded in a 96-well plate (cellular density:8000/15000 cells per well), and medium containing NPs at concentrations ranging from 100 to 1000 µg/mL or free drug was added. Cells were cultured at 37 °C and 5% CO2. After 24 h, the culture medium was removed, and the cells were washed once with PBS to remove excess NPs. After removing the PBS, according to the manufacturer's instructions for the Live/Dead assay, the cells were double-stained with Calcein AM (1 µL per mL of PBS), which allowed the detection of live cells, and Ethidium Homodimer-EthD1 (4 µL per mL of PBS) for the detection of dead cells in PBS. Multiwell

plates were incubated for 20 min at 37°C. The cells were then observed using an EVOS M5000 (Thermo Fisher Scientific).

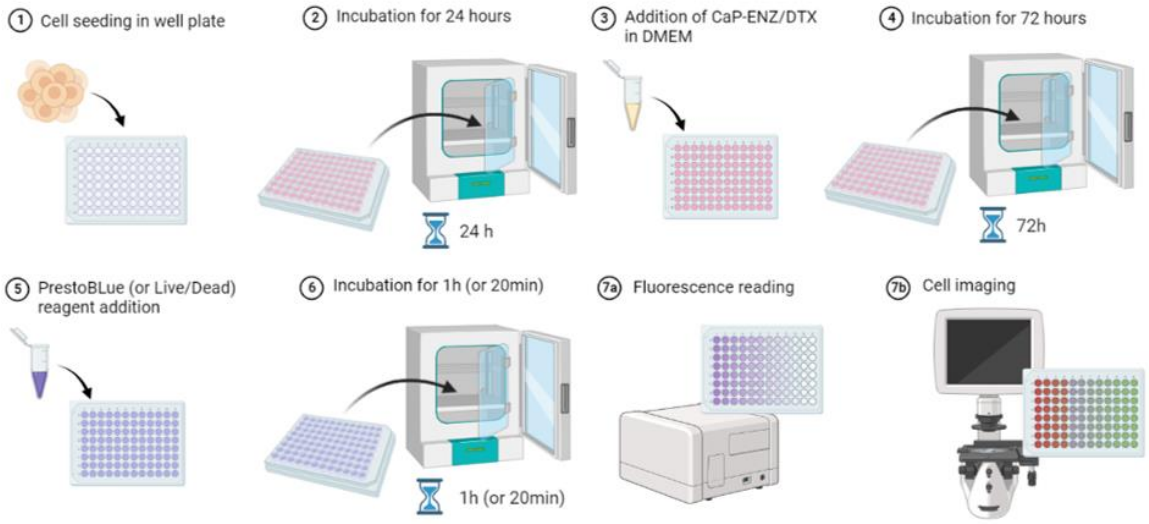

Fig. 32: Protocol for the evaluation of cellular viability on 2D models.

5.4.4 Statistical analysis

All the results were expressed as mean ± standard deviations for triplicate experiments. The mean values obtained in the treatment and control groups were compared and significant differences were determined by two-way ANOVA, followed by Turkey's multiple comparison test using levels of statistical significance of $p < 0.05$ (*), $p < 0.01$ (**), $p < 0.001$ (***), and $p < 0.0001$ (****).

6 RESULTS AND DISCUSSIONS

6.1 CQDs characterization

6.1.1 Physico-chemical characterization

Chitin is a material found in some types of fungus and yeasts as well as the shells of marine invertebrates and insects. It represents biomass waste that can be successfully converted into CQDs. Furthermore, chitin has attracted considerable attention owing to its biocompatibility, nontoxicity, and eco-friendliness (Gomes et al., 2019). In this study, the synthesis of CQDs was based on the degradation and carbonization of chitin during pyrolysis and hydrothermal treatment, starting from bio-oil as an intermediate product. The conversion reaction of chitin into CQDs, for which the intermediate product structure is not yet known, is illustrated in Fig.33 (Desmond et al., 2021).

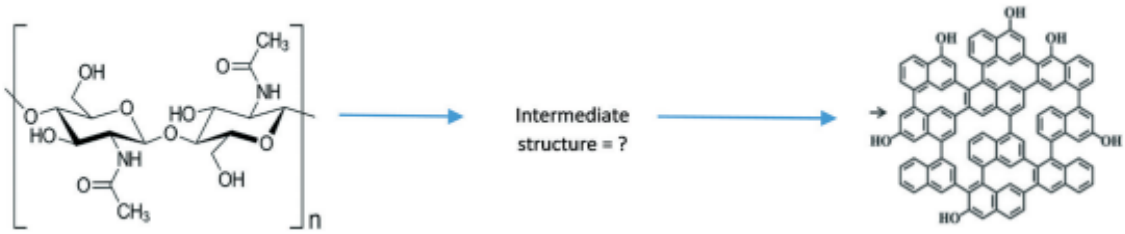

Fig. 33: Conversion reaction of chitin into CQDs (Desmond et al., 2021).

The optical properties of the synthesized CQDs were investigated using UV-Vis absorption and photoluminescence (PL) spectra. These results confirm the successful synthesis of the CQDs. Illumination of the CQD sample with a UV lamp of 12" at a wavelength of 300 nm revealed the presence of luminescence. In particular, as seen in Fig.34, intense blue light indicates the high presence of CQDs in the solution,

Fig.34: images of CQDs while held under the UV lamp.

demonstrating their small size and ability to emit a large amount of energetic light according to the quantum confinement effect.

The next step was to determine the absorbance of light by dots. The UV-Vis absorbance curve of the CQD sample in Fig. 35 shows fluorescence at 300 nm. The absorption peak at a wavelength between 230-280 nm is due to the π–π* electronic transition of the C=C bonds belonging to an aromatic ring (Alas et al., 2020).

The results obtained from the two previous tests confirm the synthesis of CQDs starting from bio-oil products derived from the pyrolysis of chitin.

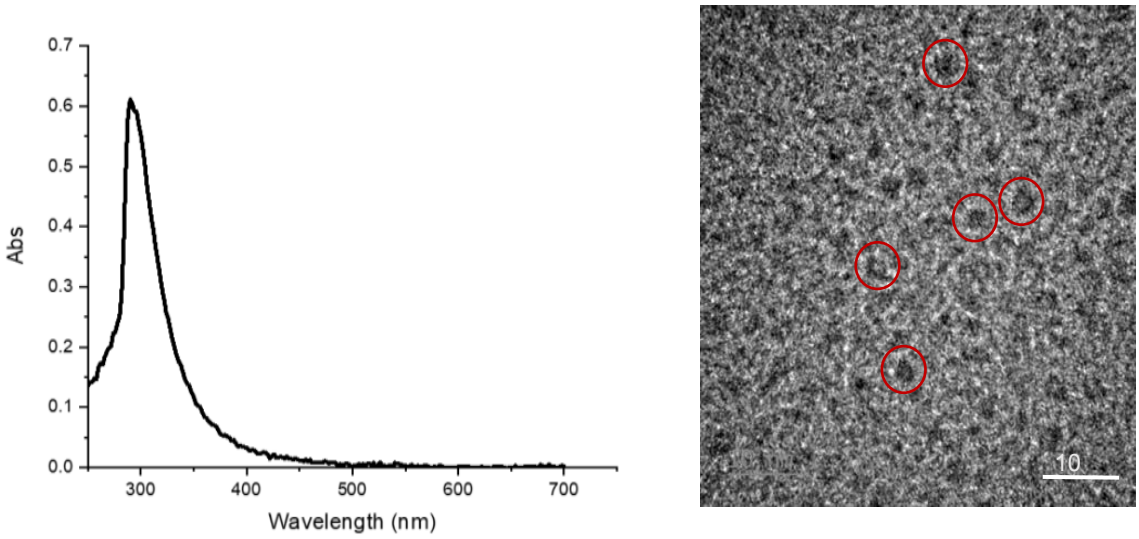

Fig. 35: (Left) UV-Vis spectra of CHBOCQDs. (Right) HRTEM of CQDs.

6.1.2 Morphological characterization

The morphology of the CQDs was determined using High-resolution Transmission Electron Microscopy (HRTEM). The images obtained demonstrate the success of the HTC process, starting from the bio-oil products. As shown in Fig. 30, all CQDs were smaller than 10 nm and round. This result is in good agreement with the literature date (Gomes et al., 2019).

6.1.3 Cytotoxicity evaluation

The *in vitro* biocompatibility of CQDs was evaluated using PrestoBlue and Live/Dead assays by incubating neo-dermal fibroblast cells with CQDs for 24h and 48h.

(a)

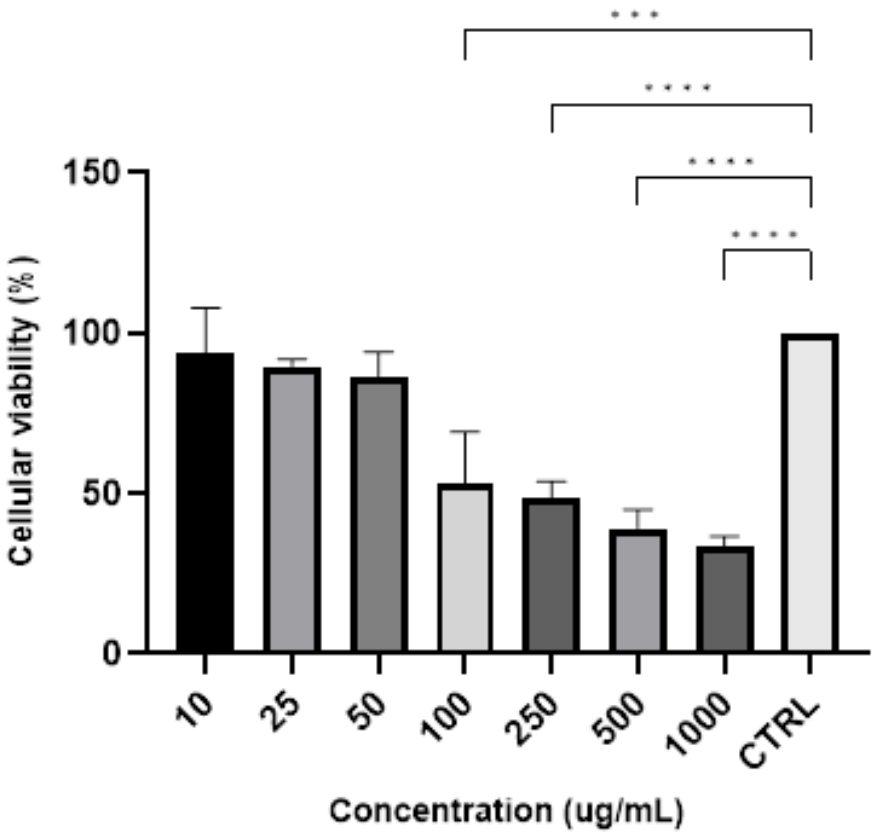

(b)

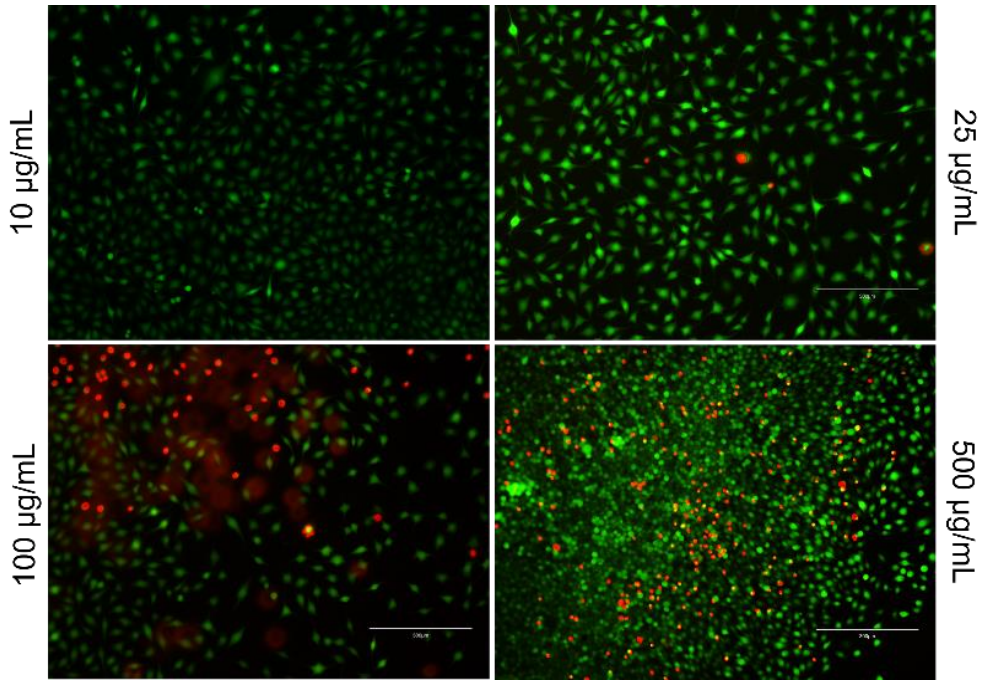

Fig. 36: PrestoBlue (a) and LiveDead assay (b) of Neo-dermal Fibroblast seeded with CQDs at different concentrations.

As seen in Fig.36a, the PrestoBlue assay shows that after 48h the CQDs do not show a relevant cytotoxic effect for concentrations up to 50ug/mL; in these cases, the cellular viability values are higher than 90%. While for concentrations higher than 100ug/mL the cellular viability is halved.

The cytotoxicity of the CQDs was also confirmed using a Live/Dead assay (Fig. 36b). The assay revealed a large number of live cells (green) compared with dead cells (red) for concentrations lower than 100ug/mL, while the number of dead cells significantly increases at higher concentrations of CQDs. This value does not agree perfectly with the results reported in the literature. For example, Janus et al. identified 0.30 mg/mL a biosafe concentration of CQDs for use. This difference in the values obtained could be related to the fact that the CQDs were not sterilized, which could have influenced their cytotoxicity in fibroblasts (Janus et al., 2020).

6.2 NPs characterization

6.2.1 CaP synthesis

6.2.1.1 Morphological analysis

CaP particles were synthesized using a peristaltic pump, which controlled the flow rate of the reactant solutions and thereby regulated the size and morphology of the resulting particles. The pump was operated in a continuous flow synthesis process to precisely control the addition of a calcium-containing solution to a phosphate-containing solution, which resulted in the precipitation of CaP particles. In particular, CaP particles were formed during a crystallization time of 5 s and subsequently stabilized in colloidal form by the deposition of PAH for 15 s to obtain a precipitation of NPs, as demonstrated by Urch et al. (2009). The times were calculated based on the pump flow rate and tubes diameter. The yield of the CaP particle synthesis process (Y (%)) was 15%. The reduced number of particles produced was related to the removal of most of the starting material during the dialysis process. Another reason for the low yield was the loss of particles during the freeze-drying process due to the size of the holes in the parafilm that were created manually.

CaP particles are often used as carriers in drug delivery systems because they are biocompatible and can be easily absorbed by the body (Trofimov et al., 2018). In this study, CaPs containing different concentrations of DTX were synthesized (150, 300, and

500 µL). The optimal concentration of DTX in the core was identified based on the results of the particles' physicochemical, morphological, and DTX release analyses.

The dimension of the CaP particles depends on the amount of encapsulated drug. If the drug is loaded into the core of the particle, the size of the particle may increase owing to an increase in the overall volume. The sizes of the CaP particles obtained with different concentrations of DTX were evaluated using TEM analysis. In particular, as shown in Fig.37, particles with an average size 108 ± 8 nm were obtained for all DTX concentrations. Hence, different amounts of encapsulated DTX did not significantly change the final size of the CaP particles.

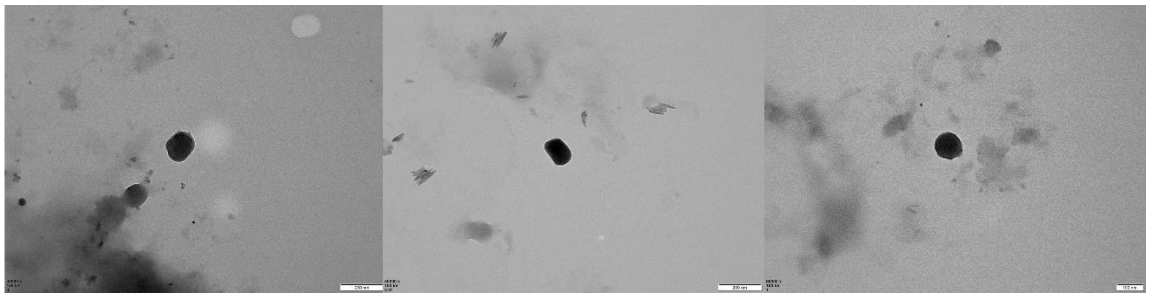

Fig. 37: TEM images of CaP particles loaded with DTX (150, 300, 500 µL).

6.2.1.2 Physico-chemical characterization

By analyzing the ζ-potential value, it was verified that an increase in the amount of encapsulated DTX corresponded to a decrease in the ζ-potential value (Fig.38).

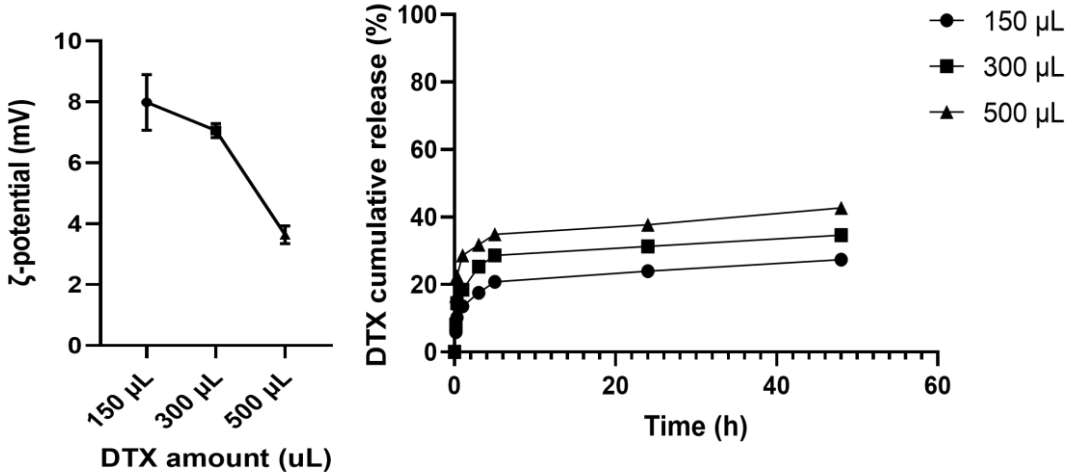

Fig.38: (a) ζ-potential values of the CaP particles with different amount of DTX; (b) DTX cumulative release from CaP particles.

This is related to the fact that the charge of DTX can vary according to the pH of the solution in which it is dissolved. The exact pK_a value of DTX may vary slightly depending on the specific formulation or solvent used; however, it is generally approximately 10 (Sohail et al., 2018). At pH values below this value, DTX is predominantly in its protonated and positively charged form. As the pH increased above pK_a, an increasing number of DTX molecules became deprotonated and negatively charged.

For the synthesis of the CaP particles, DTX was dissolved in a solution at pH 10, a value for which it was negatively charged. The release of DTX from the CaP particles core was studied for up to 48 hours. As shown in Fig. 38b, the amount of DTX released increased proportionally with the amount of encapsulated drug. Furthermore, in the case of the maximum amount of encapsulated DTX, the saturation point was not reached; therefore, it is possible to further increase the amount of DTX encapsulated in the CaP particles. DTX release was also characterized by an initial burst release of less than 20% in all cases and a constant release over the following days. This proves that the CaP particles and PAH layer alone were adequate to ensure a gradual, controlled release of the drug.

Based on the results obtained from the various analyses conducted on the CaP particles, only the system with 500 µL of DTX encapsulated in the core of the CaP particles was considered. This choice is linked to the fact that there are no significant differences between the three systems; therefore, the system that was able to release the greatest amount of drug was chosen.

FTIR spectroscopy of CaP particles was performed to investigate their chemical structure. As shown in Fig. 39, the FTIR spectrum displayed several characteristic bands of the CaP particles, demonstrating their successful synthesis. The phosphate groups in the CaP particles gave rise to a series of absorption bands in the FTIR spectrum. The bands at approximately 460, 550–600, 960, and 1020–1100 cm^{-1} were attributed to the symmetric stretching vibration of PO_4^{3-} ions. Furthermore, CaP particles contain carbonate ions that give rise to absorption bands which can be observed at 875 cm^{-1} and around 1420 and 1480 cm^{-1}. In some cases, they could also be attributed to the absorption of atmospheric carbon dioxide during the preparation of the particles. Moreover, stoichiometric hydroxyapatite's typical low-intensity OH ions-derived bands at 630 and 3570 cm^{-1} are seen. The presence of absorbed water could also be detected from the FTIR spectra in the region around 3300-3500 cm^{-1} (Salma et al., 2008). The peaks at approximately 1630 cm-1 and 1410 cm^{-1} are attributed to the stretching vibration of the C=N bond and the N-H group of the PAH used to coat the CaP particles.

Additionally, by comparing the FTIR spectra of the CaP particles with and without DTX, as shown in Fig.39, it is possible to confirm the correct encapsulation of DTX within the CaP particle core. DTX has characteristic bands, including carbonyl, aromatic ring, and amide vibration bands. In particular, from the FTIR spectrum obtained, it is possible to identify the characteristic peaks of DTX at 3368 cm^{-1} (N-H and O-H stretching) and 2984 cm^{-1} (C-H stretching) (da Rocha et al., 2020).

High-resolution XPS was employed to further investigate the surface chemical elements and chemical compositions. XPS can provide qualitative and quantitative information on the different elements on the surfaces of nanoparticles. The XPS spectra of the CaP particles (Fig.40a) clearly shows that the O1s peak appears at 531 eV and the C1s peak at 285 eV, which confirms the presence of carbon and oxygen in the CaP particles. The peaks around 399, 347, and 133 eV confirm the presence of Na, Ca, and P, respectively, which are characteristic of the materials used in the synthesis of CaP particles. Si atoms were found in the CaP particles under analysis; this was undoubtedly a result of contamination caused by their proximity to other samples.

Furthermore, the high-resolution C1s and O1s spectra of the CaP particles (Fig.40b) were obtained and fitted with the curve-fitting function in the CasaXPS software. The high-resolution spectra of C1s and O1s are shown in the figure, associated with the different chemical bonds with the respective peaks appearing in the spectra.

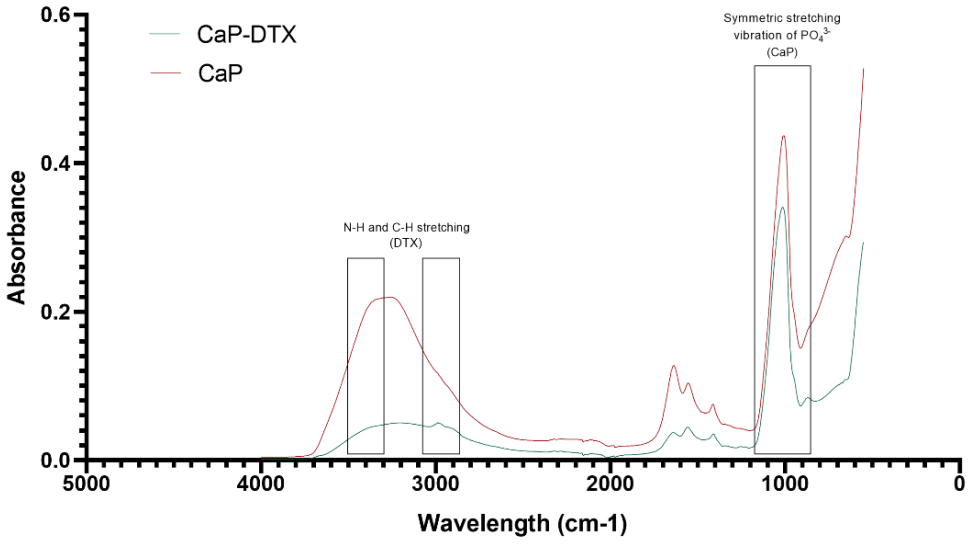

Fig.39: FTIR spectra of CaP particles with and without encapsulated DTX.

The encapsulation efficiency of DTX in the CaP particles was calculated by spectrometric analysis, obtaining a value of 7.4% ± 0.5 .Spectrometric analyses of the supernatant solutions obtained in the various steps of the synthesis process of the CaP particles showed that almost all of the DTX remained in the solutions instead of inside the CaP particles. In general, the chemotherapeutic loading efficiency of CaP particles is not adequate for cancer chemotherapy. As a result, efforts have been made to improve the efficacy of CaP particle encapsulation by complexing drugs with biomolecules on the particle's surface rather than within it(Huang et al., 2019).

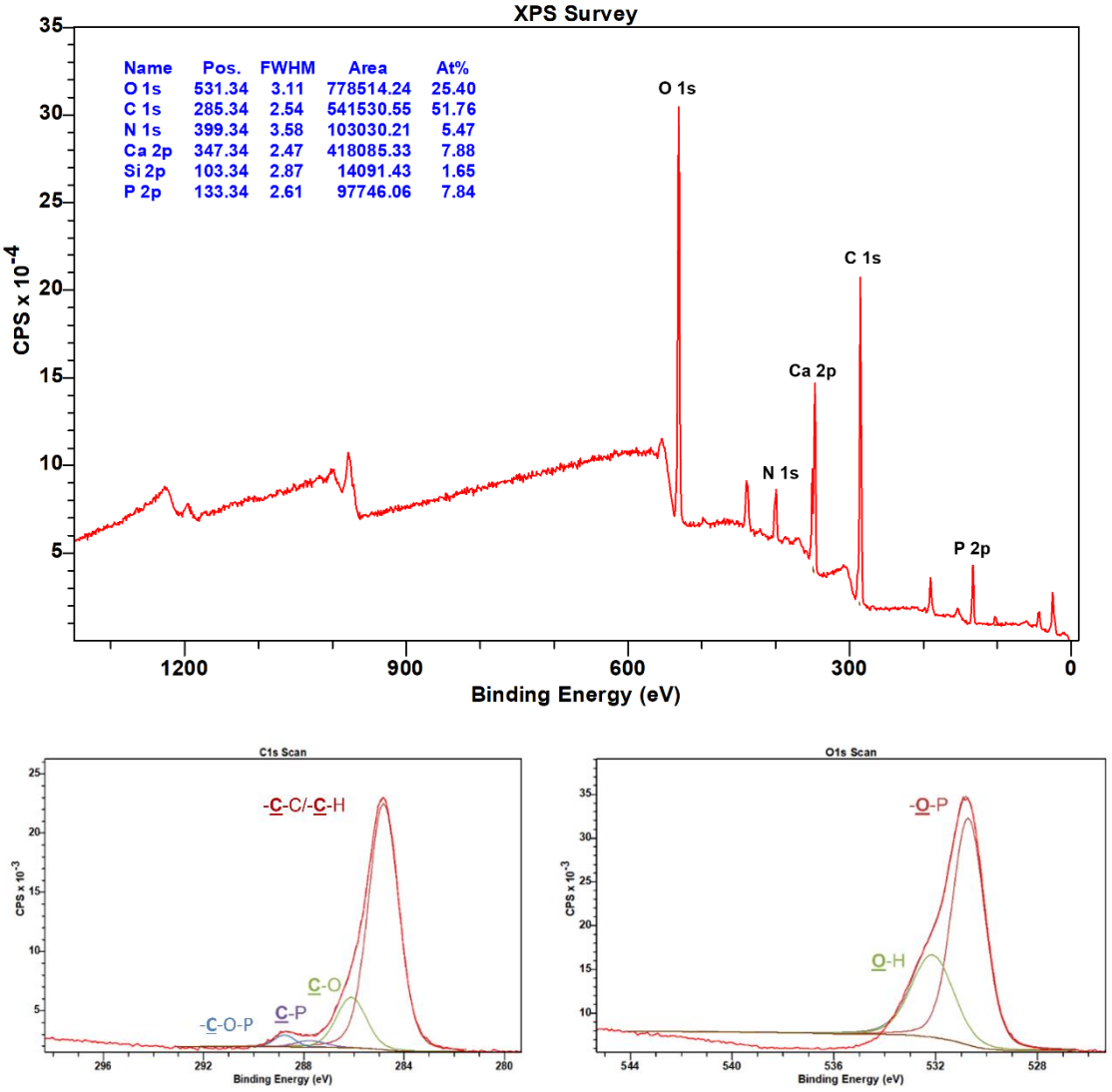

Fig.40: (a) XPS spectra of CaP particles; (b) High resolution spectra od C1s and O1s.

6.2.2 Deposition of polyelectrolytes on CaP particles

6.2.2.1 Physico-chemical analysis

Subsequent deposition of the polyelectrolyte layers on the CaP particles was conducted at pH 6. This pH level was chosen considering the constant dissociation of the polymers, but it is primarily motivated by the desire to create an environment that is as close to physiological as possible. The system must be able to maintain physiological pH levels to achieve site-specific drug release from the particles during bloodstream circulation.

Understanding the effect of pH on the ζ-potential of polyelectrolytes is necessary to determine the ideal conditions for forming FUR/CHI complexes on CaP particles. FUR is an anionic sulphated polysaccharide extracted from the red alga, *Furcellaria lumbricalis*. It is non-toxic, biodegradable, biocompatible, soluble in water, and has exceptional gel-forming capabilities (Marangoni Júnior et al., 2021). Although there is limited research on the use of FUR for specifically treating PCa, there are several ways in which it could potentially be used to enhance current treatment strategies, such as a drug delivery system. FUR is an effective carrier of various drugs, including anticancer agents. The encapsulation of these drugs in FUR could improve their bioavailability and reduce their toxicity, thereby enhancing their efficacy against PCa cells. The chemical structure of FUR (Fig. 41) is characterized by the presence of a repeating backbone of alternating 3-linked β-D-galactose and 4-linked α-D-galactose residues. It is currently considered to be a type of κ-carrageenan (Laos & Ring, 2005). In polar solvents, such as water, the sulphate groups of FUR dissociate, leaving charges on the polymer chain and releasing counter ions into the solution. These charged polymer chains can easily interact with other polymer chains through electrostatic interactions. Jamroz et al. determined the dependence of the ζ-potential of FUR on pH at different ionic strengths. They demonstrated that the ζ-potential is independent of pH at a given ionic strength, which could be expected because the charge originates from strongly acidic sulphate groups (Jamróz et al., 2014). Regardless of the pH value, the ζ-potential of FUR used in this study is negative (-36.9 ± 0.3 mV), as shown in Fig. 43, owing to the presence of ionic (sulfonyl hydroxide) groups.

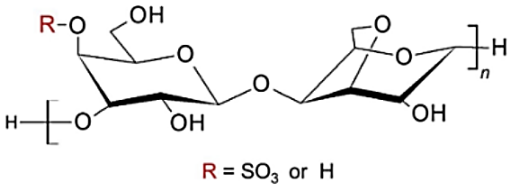

Fig. 41: FUR chemical structure.

On the other hand, CHI, a copolymer of β(1→4)-2-amino-2-deoxy-D-glucopyranose and β(1→4)-2-acetamido-2-deoxy-D-glucopyranose or a homopolymer of β(1→4)-2-amino-2-deoxy-D-glucopyranose, is a natural cationic copolymer produced by the deacetylation of chitin (Fig. 42). CHI has been extensively investigated as a drug delivery system because of its biocompatibility, biodegradability, and ability to form nanoparticles. CHI nanoparticles have effectively encapsulated various anticancer drugs, including paclitaxel, doxorubicin, and docetaxel. These nanoparticles could potentially be used to enhance the efficacy of these drugs against PCa cells, while minimizing their toxicity to healthy cells.

CHI is characterized by good solubility in acidic media owing to the presence of amino groups susceptible to protonation, whereas it is insoluble in water and alkali. The degree of diacylation is an important characteristic of chitosan, as only those with diacylation above 80% showed the highest activity. Despite this, a higher percentage of diacylation corresponds to lower water solubility and biological activity. The molecular weight of chitosan also influences its properties. CHI with a molecular weight below 30 kDa may be soluble in water; however, its solubility decreases as the weight increases. polysaccharides with higher molecular weights are soluble only after protonation of their amino groups in the presence of an acidic medium. In addition, polymers are biocompatible, non-toxic, and bio adhesive (Kurczewska, 2022). The ζ-potential of CHI used in this study is positive (17.6 ± 1.8 mV) owing to the charged amino groups, as shown in Fig. 43. Unlike FUR, the zeta potential of CHI depends on the pH of the solution in which it is solubilized. Indeed, at pH<6.5, the amino groups of the D-units of CHI are predominantly positively charged owing to the low pK_a value of these groups.

This study indicated that negatively charged FUR and positively charged CHI are excellent candidates for the formation of layers in the preparation of NPs. Fig.39 illustrates the process by which electrostatic interactions between FUR and CHI are formed.

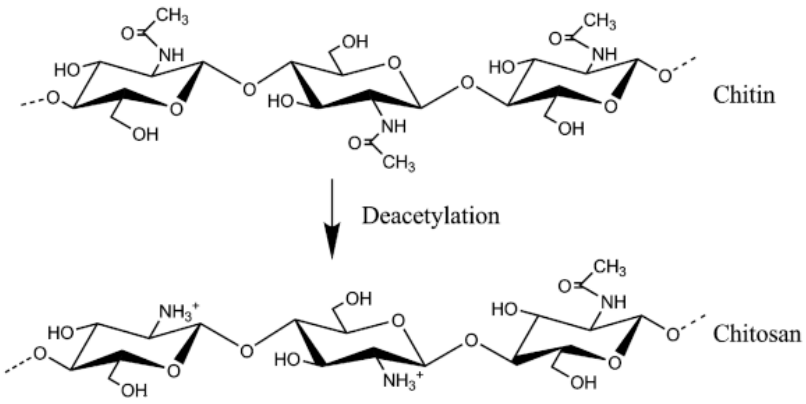

Fig. 42: CHI and chitin chemical structure.

Using the layer-by-layer assembly technique, successive layers of CHI and FUR were deposited on the CaP particles to obtain 4 layers of polyelectrolytes. The total volume of the polyelectrolyte solution used for the formation of the new layers was determined experimentally by evaluating the ζ-potential. In particular, reaching a constant value of the ζ-potential after the addition of further polyelectrolyte indicates the volume necessary for the formation of a new polyelectrolyte layer. For this reason, it was necessary to increase the volume of polyelectrolytes for the formation of the third and fourth layers to avoid significantly varying the ζ -potential value.

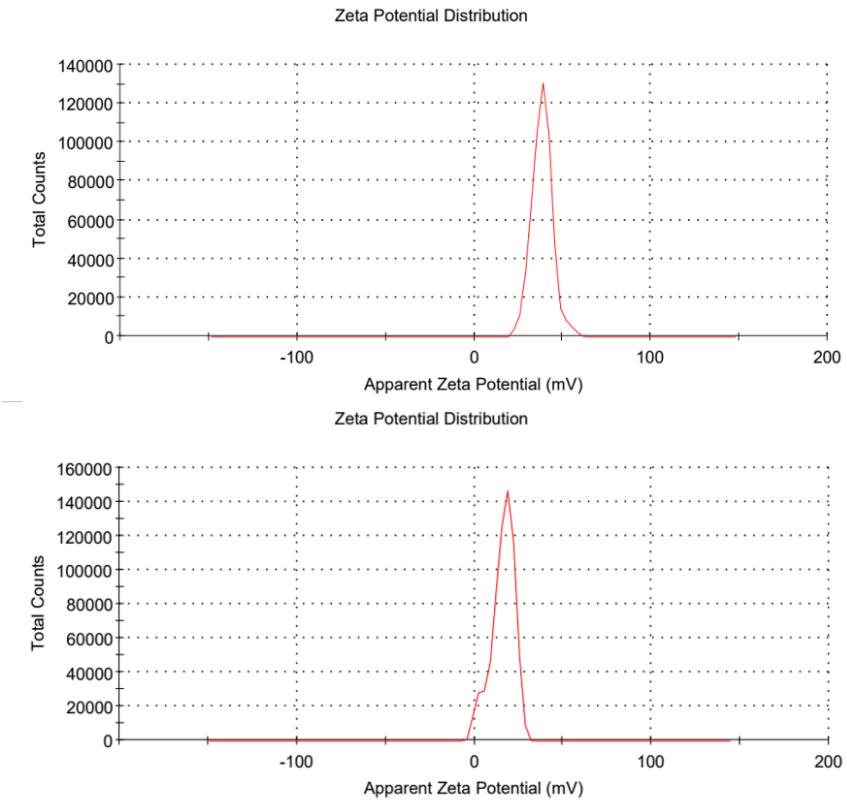

Fig. 43: ζ-potential of FUR (up) and CHI (down).

Within the various layers have been encapsulated one or two different types of drugs. Both DTX and ENZ are hydrophobic (water-insoluble) molecules with a net charge of zero at a physiological pH (approximately 7.4). This means that they are uncharged molecules in neutral environments, such as the bloodstream or cell membranes.

In particular, at physiological pH (approximately 7.4), DTX and ENZ are neutral molecules because they do not have a precise positive or negative charge. However, functional groups can potentially ionize at higher or lower pH values, resulting in a partially positive or negative charge on the molecule. The net charge value measured for DTX, solubilized in DMSO:PBS and water, at pH 6 was negative, so it was encapsulated only in the negative layers. While in the case of ENZ, solubilized in DMSO and water, at pH 6, a neutral value of ζ -potential has been obtained. Therefore, it can be contained in both positive and negative layers.

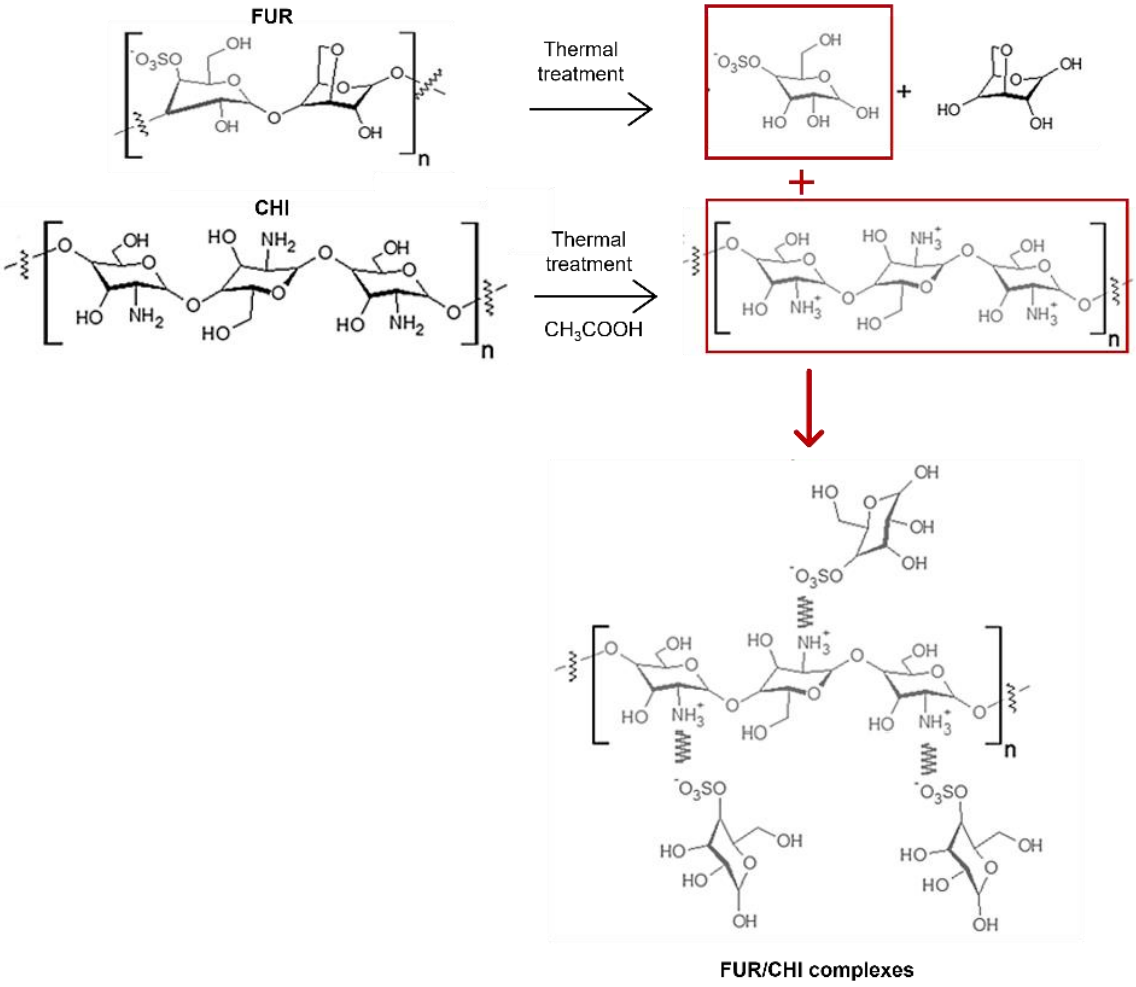

Fig. 44: Electrostatic interactions formed between FUR and CHI (Milosavljevic et al., 2020).

In this study, depending on the system, it was chosen to encapsulate both drugs in the FUR layers, the negatively charged polyelectrolyte layers.

In particular, in the CaP-no drugs system, no drugs were encapsulated in the layers. In the CaP-ENZ system, only ENZ was encapsulated in both layers of FUR. Instead, in the CaP-ENZ/DTX system, both ENZ and DTX were encapsulated in FUR layers to investigate the synergistic effect of the two drugs Fig.45 shows the value of ζ-potential for each layer in the three systems. In all cases studied, the phenomenon of charge reversal was noted, demonstrating that drug encapsulation did not affect the value of the ζ-potential of the layers in which they were encapsulated. Furthermore, all systems showed a positive zeta potential value higher than +20mV and a negative value not lower than -20mV, with the exception of the second layer, which can be considered a settlement layer. Therefore, it is possible to consider the obtained NPs stable systems.

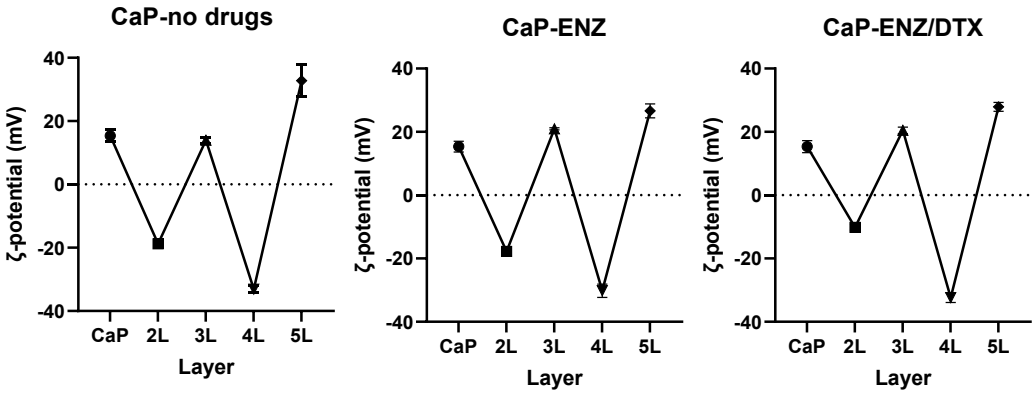

Fig. 45: ζ-potential of FUR (up) and CHI (down).

To confirm the successful deposition of the polyelectrolyte on the previous layer, FTIR spectroscopy was used to examine the chemical structure of the NPs obtained after each layer of FUR and CHI was deposited.

FTIR spectrum of the second and fourth layers of the CaP-No drug system are shown in Fig.46 along with the spectrum of FUR. The following wavelengths allowed for the identification of some distinguishing bands in the FUR control spectrum: 1157 cm^{-1} and 1032 cm^{-1}, 922 cm^{-1}, 1246 cm^{-1}, which correspond to the bridge C-O stretching and C-O stretching vibration, stretching mode of C-O-C in the repeating disaccharide sequence of α-d-galactopyranose, O=S=O symmetric vibration, respectively (Salma et al., 2008). These peaks were also found in the second and fourth layers of the system, which

corresponded to the deposition of FUR on the CaP particles, demonstrating the successful deposition of FUR.

The FTIR spectrum of CHI is shown in Fig.47, along with those of the third and fifth layers of the CaP-no drug system. In the region between 3291 cm^{-1} and 3361 cm^{-1} in the spectrum of pure CHI, there was a noticeable band corresponding to intramolecular hydrogen bonds and N- and O-H stretching. These two peaks were more evident in the fifth layer of the system, in contrast to the third layer of the system, in which they were not easily noticeable. This is most likely caused by the polyelectrolyte volume of the last layer being higher than that of the third, which enables a more even uniform CHI coating. Furthermore, stretching of the C-H atoms in symmetric and asymmetric ways is responsible for the absorption bands at approximately 2921 cm^{-1} and 2877 cm^{-1}, respectively, in the spectra of CHI. Instead, the bands at roughly 1645 cm^{-1} (C=O stretching of amide I) and 1325 cm^{-1} (C-N stretching of amide III) confirmed the presence of residual N-acetyl groups of CHI (Salma et al., 2008).

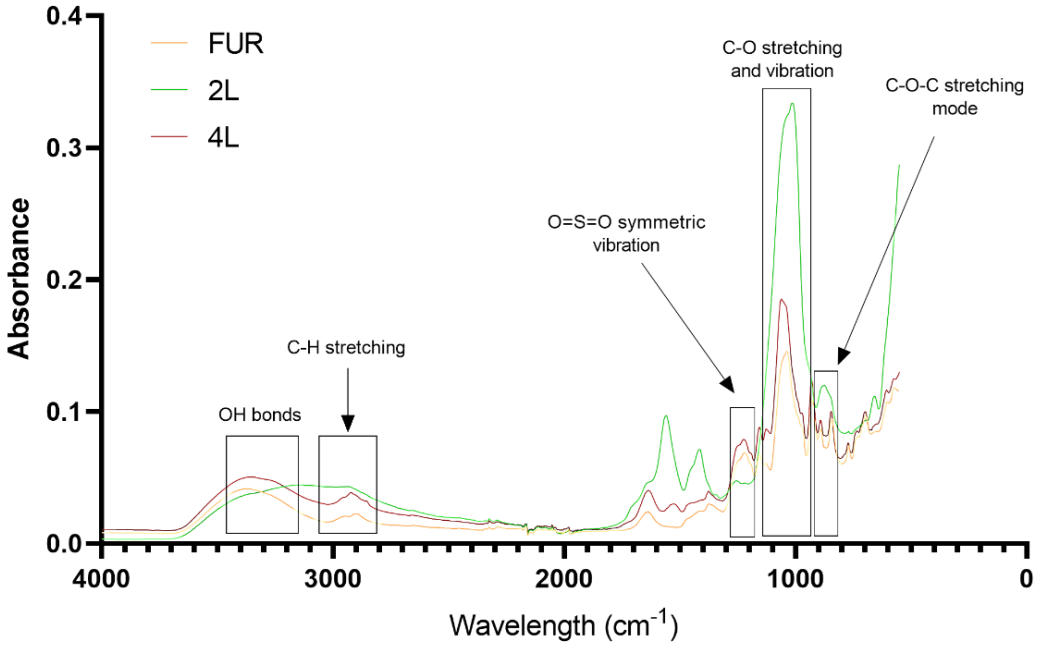

Fig. 46: FTIR spectra of FUR, 2L and 4L of CaP-no drugs.

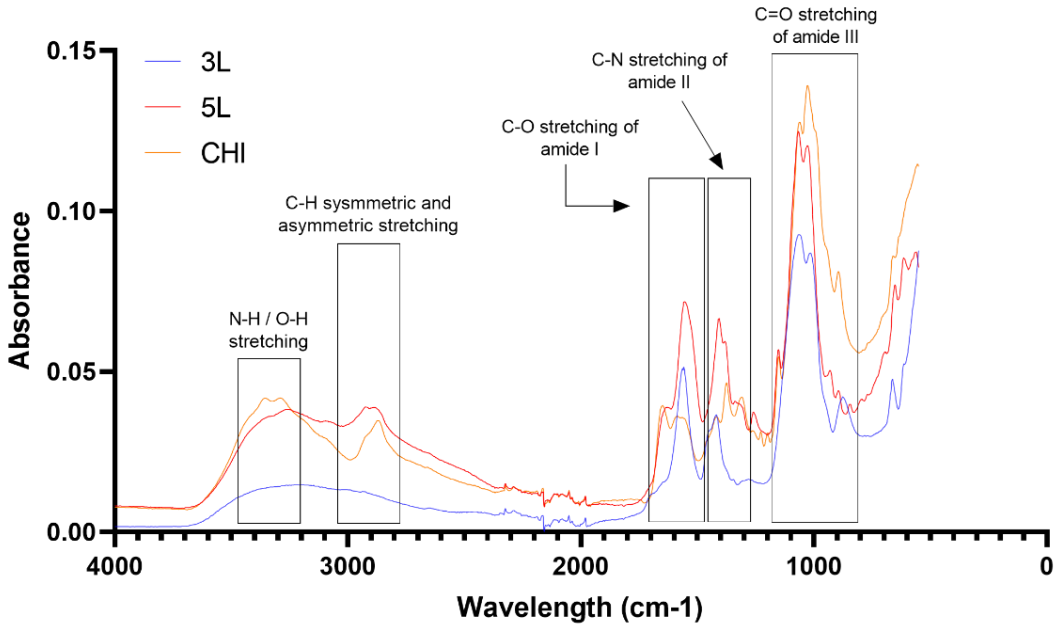

Fig. 47: FTIR spectra of CHI, 3L and 5L of CaP-no drugs.

The complexation of FUR with CHI led to a shift in the ionized groups of FUR and CHI, which may be proof of intermolecular interactions involving the -OSO_3- groups in FUR with the -NH_3 groups in CHI. The peak at 1555 cm^{-1} indicates symmetrical deformation of the -NH_3^+ groups, suggesting that electrostatic interactions occurred between the ionizable groups of the sulfated polysaccharide and CHI's amino group. Significant shifts were observed for the bands at 1650 cm^{-1}, assigned to the hydroxyl group (Salma et al., 2008). The FTIR spectra of the different FUR and CHI layers deposited in the CaP-ENZ system are shown in Fig. 48. The presence of ENZ through FTIR analysis was identified by the presence of characteristic peaks at the following wavelengths: 3433, 3095, 2951, 2233, 1763, 1607, 1499, 1270, 1136, 1052, 998, and 786 cm^{-1} (da Rocha et al., 2020). Most of the peaks in this instance are difficult to distinguish because they are obscured by other peaks that are representative of other materials that are present in the system at higher concentrations. However, it is possible to spot a peak that appears at a wavelength of approximately 1000 cm^{-1}, which is indicative of ENZ's presence in the system. Fig. 49 shows the FTIR spectra of the layers related to the CaP-ENZ/DTX system. In addition, DTX was also identified. It is difficult to identify the second and fourth layers because their characteristic peaks correspond to those of other materials.

The elements and surface chemicals of the three synthesized particle systems were identified using high-resolution XPS. In Fig.50a, the XPS spectrum of CaP-no drugs is shown. The XPS spectra, in contrast to those previously obtained for the CaP particles,

clearly show the appearance of a peak at 169 eV, which confirms the presence of sulfur in the particles of the CaP-no drug owing to the deposition of FUR layers. Instead, the presence of the peak at 399 eV as well as those at 532 and 285 eV, associated nitrogen, carbon, and oxygen, respectively, are an indication of correct CHI deposition. Furthermore, a shift in the O1s peak of the sulfate groups toward higher binding energies provides further evidence of the interaction between the final two external layers of FUR and CHI.

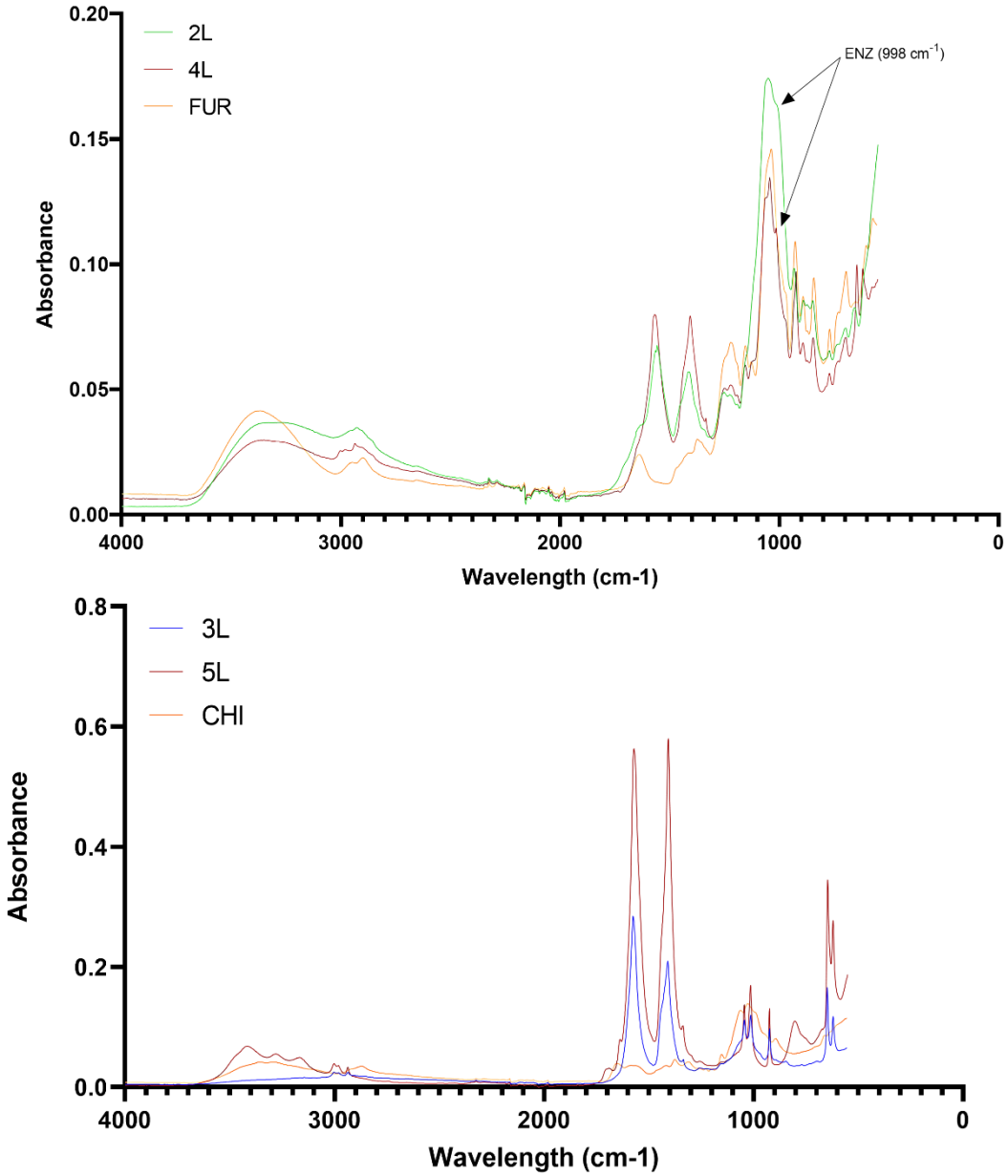

Fig. 48: FTIR spectra of FUR, 2L,4L, CHI, 3L and 5L of CaP-ENZ.

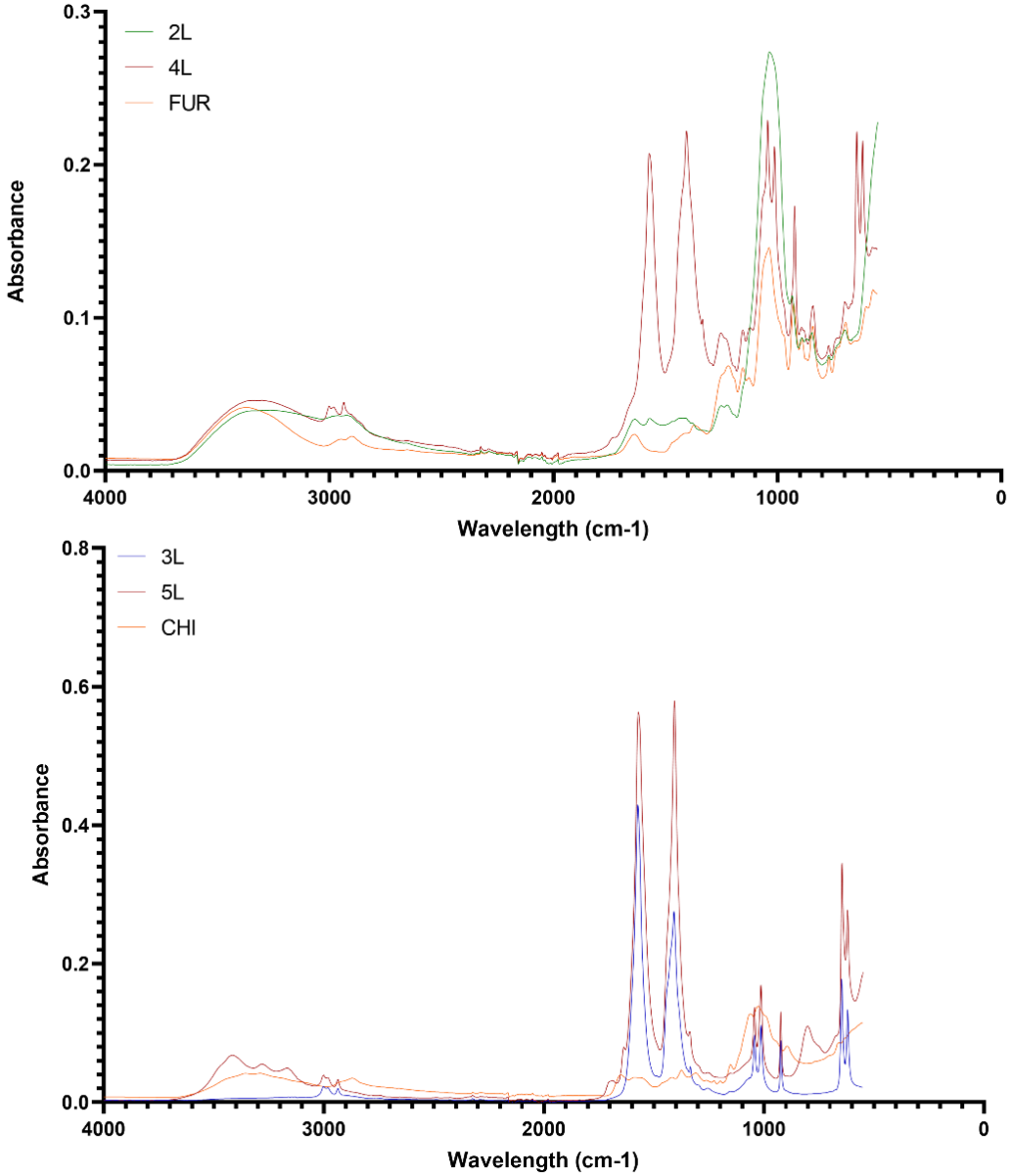

Fig. 49: FTIR spectra of FUR, 2L,4L, CHI, 3L and 5L of CaP-ENZ/DTX.

In comparison, the O1s peak of the amino groups may shift towards lower binding energies. In Fig.50b the XPS spectrum of the CaP-ENZs is reported. With the exception of the peak that appeared due to the presence of fluorine in the CaP-ENZ system, there were no obvious changes in the spectra when compared to the CaP-no drug system.. This demonstrated the effective encapsulation of ENZ in the system.

The At% of nitrogen and sulfur is noticeably higher in the CaP-ENZ/DTX+PSMA-617 system's XPS spectrum (Fig.50c), which is related to the surface functionalization of the outermost layer of CHI with PSMA-617 by EDC/NHS. In addition, the high-resolution C1s and O1s spectra of CaP-no drugs, CaP-ENZ were examined. The pertinent peaks

connected to the chemical bond in which the C or O atoms are engaged are displayed in Fig.51.

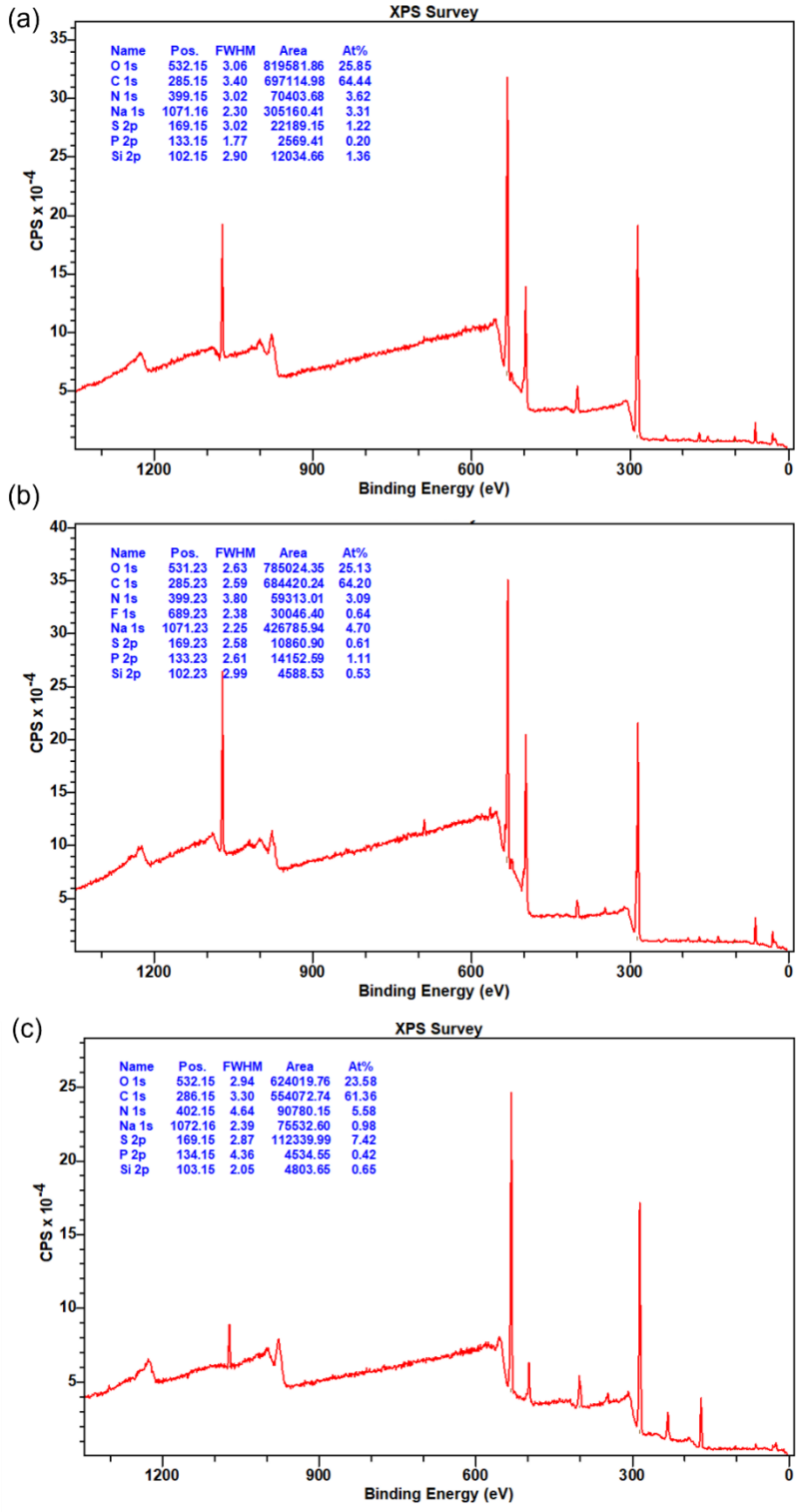

Fig. 50: XPS spectra of (a) CaP-no drugs, (b) CaP-ENZ, (c) CaP-ENZ/DTX+PSMA-617

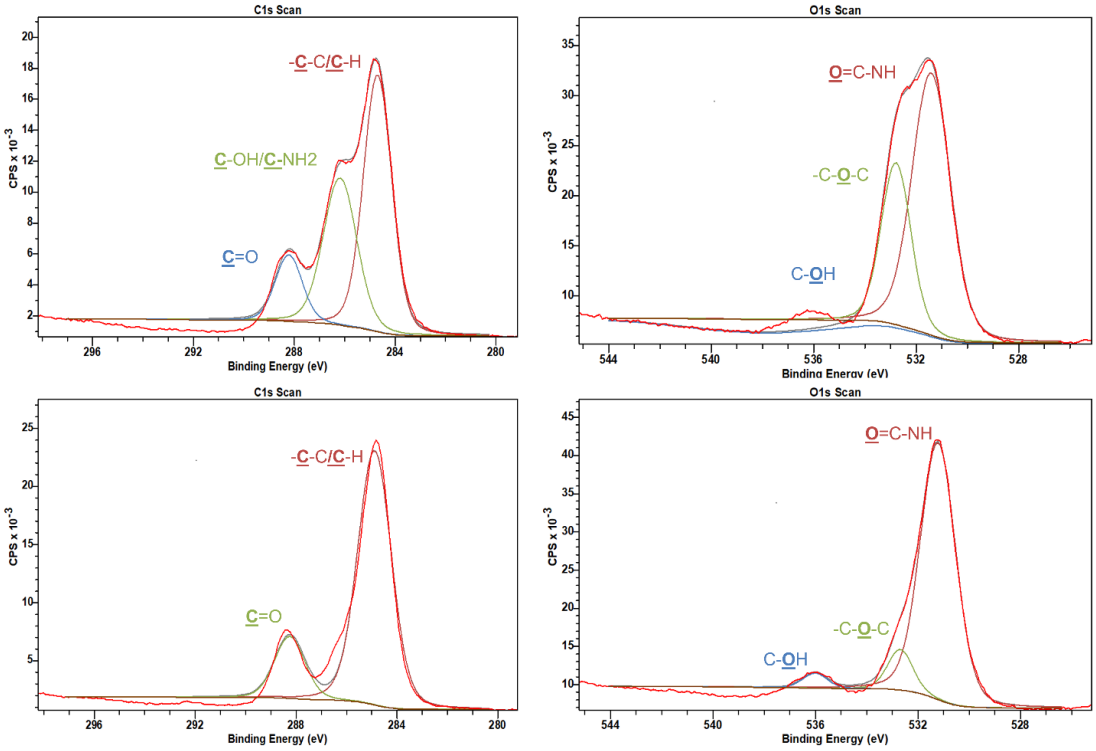

Fig. 51: High resolution C1s and O1s spectra spectra of (a) CaP-no drugs, (b) CaP-ENZ, (c) CaP-ENZ/DTX+PSMA-617

6.2.2.2 Morphological analysis

TEM was used to evaluate the morphology and size distribution of CaP-no, CaP-ENZ, CaP-ENZ/DTX. Fig. 52 shows that the nanoparticles obtained in all systems were spherical and smooth. Notably, the polyelectrolyte coating and entrapment of ENZ and DTX did not alter the spherical shape of the initial CaP particles. However, the addition of DTX and ENZ in the second and third systems influenced the final size of the nanoparticles, as shown in Fig. 53, where the average sizes of CaP-no drugs (157±3.7 nm), CaP-DTX (197±0.96nm), CaP-ENZ/DTX (196 ±2.13 nm), were reported.

After layer-by-layer assembly, the produced nanoparticles without encapsulated drugs (CaP-no drugs) showed a diameter increase of approximately 50 nm compared to the CaP particles without layers, thus indicating that the average thickness of the deposited layers was ~ 50 nm. The increase in nanoparticle diameter is ascribed to the deposition of four layers of FUR/CHI on the surface of the CaP nanoparticles. Milosavljevic et al. (Milosavljevic et al., 2020) reported similar behaviour, where the deposition of four layers of CH/FUR resulted in an average thickness of 60 nm.

Moreover, most of the nanoparticles obtained for the three different systems had uniform size, without aggregation. However, visible variations in the diameters of some particles can be attributed to the shrinkage of the last CHI layer during the evaporation of the sample solution prior to imaging (Unsoy et al., 2014). Furthermore, Rivera et al. reported that a small percentage of nanoparticles have a tendency to swell during sample washing to remove free drugs and polyelectrolytes (Rivera et al., 2015).

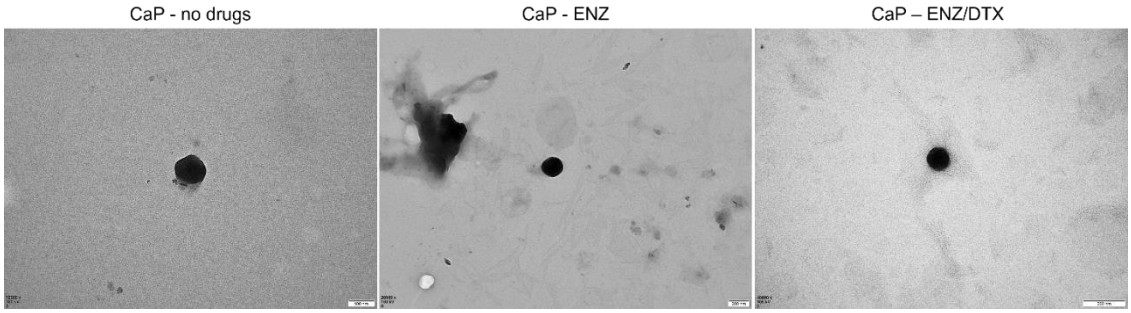

Fig. 52: TEM images of CaP-no drugs, CaP-ENZ; CaP-ENZ/DTX

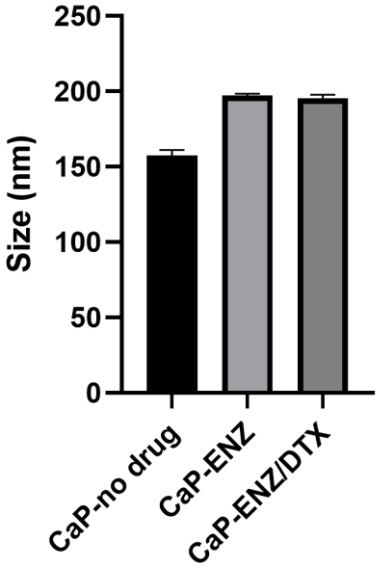

Fig. 53: Average diameter of the different nanoparticles obtained after LbL assembly

6.2.2.3 Evaluation of CQDs encapsulation in CaP-DTX/ENZ

To verify that the CQDs were properly encapsulated in the particle system, a spectro fluorophotometer excited the particle solution in the wavelength range 200–250 nm. The results are presented in Fig. 54. It is possible to note the presence of a peak at a

wavelength of 250 nm, which confirms the effective encapsulation of the CQDs in the system.

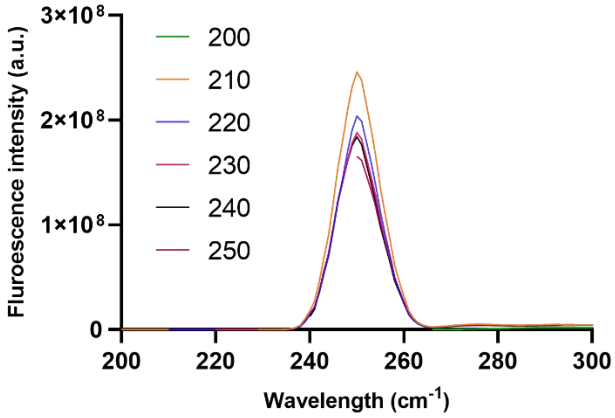

Fig. 54: Emission spectra of the CQDs at different excitation wavelengths

6.2.2.4 Cytotoxicity evaluation on 2D model

At various concentrations (100, 250, 500, 1000, 2000 µg/mL) the cytotoxicity of the different NPs systems (CaP-no drugs, CaP-ENZ, and CaP-ENZ/DTX) was assessed on two distinct cell lines: LNCaP and VCaP. As a control, in addition to cells treated without NPs, the cytotoxicity of free ENZ and DTX was also evaluated.

As shown in Fig. 55a, both in the case of LNCaP and VCaP cells, the obtained cellular viability (%) values are in no way representative of the real cytotoxic behaviour of the different systems. The high cell viability values of the cells treated with the NPs compared to the control cells were mainly due to the fact that the cells, both LNCaP and VCaP, used as controls, were not very viable after they were seeded in the multiwell wells. LiveDead assay (Fig. 55b) was further performed to assess cell viability. A higher concentration of live cells (green) than dead cells (red) was observed for both LNCaP and VCaP cells, regardless of the concentration. As also demonstrated by the PrestoBlue results, most LNCaP and VCaP cells died when they were directly treated with free ENZ and DTX. It follows that both drugs have cytotoxic effects on both cell types. However, it is possible that the amount of DTX and ENZ encapsulated in the systems was not sufficient to significantly affect the cells in a cytotoxic manner.

To solve the problem of poor viability of the cells seeded in the wells, the cell density was increased from 8000 to 15000 cells/well. This last value was chosen to consider the

subculturing procedure guidelines, according to which it is necessary to maintain cultures of LNCaP and VCaP at a cell concentration between 1×10^4 and 2×10^5 cells/cm^2 (https://www.atcc.org/products/crl-2876). Furthermore, the cells in the wells were treated with the NPs after 24h in order to allow the cells to adhere to the multiwell.

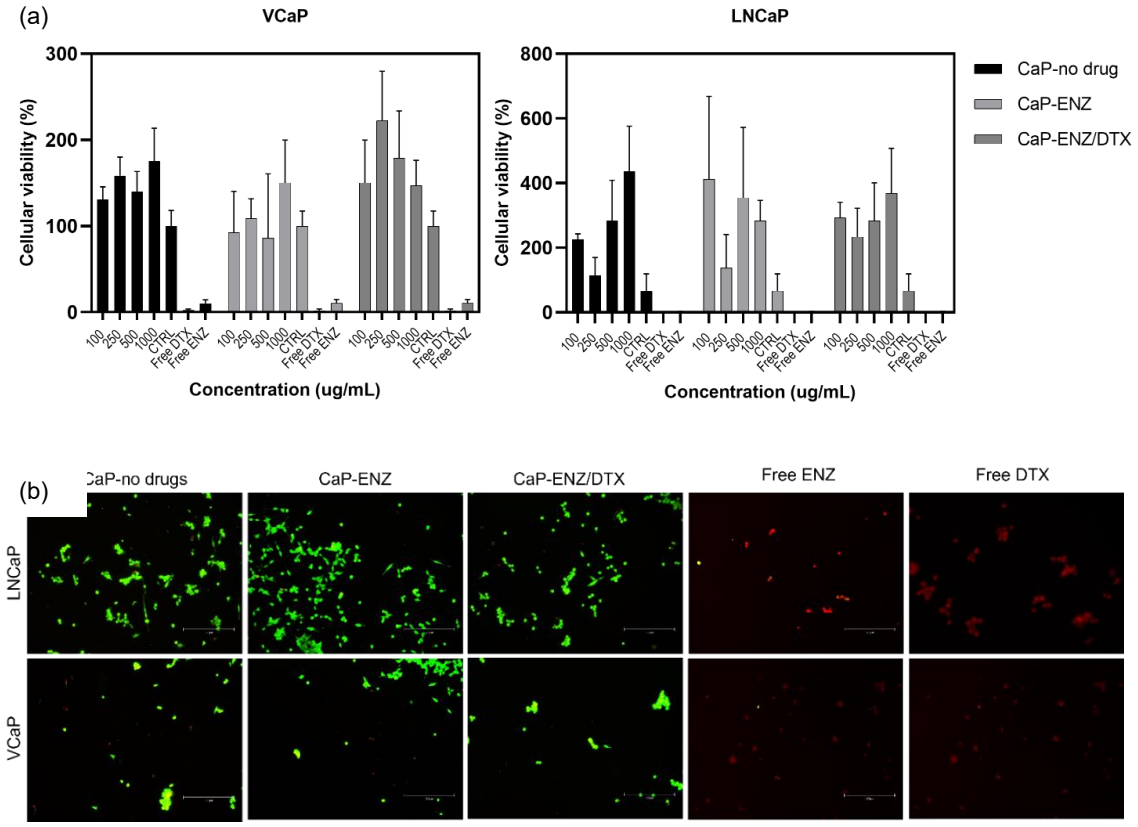

Fig. 55: (a) PrestoBlue and (b) LiveDead assay of LNCap and VCaP after 48h (Bar= 300µm).

Additionally, owing to the low EE value (%) achieved for the encapsulation of DTX in the core as well as ENZ and DTX in the layers, the concentration of both drugs was increased in both the core and the layers. In particular, 1 mL of DTX (600 µM) was encapsulated in the core of the CaP particles, while 3.75 mL of ENZ (10mM) and 3 mL of DTX (600 µM) were added to the layers.

Subsequent cellular tests were performed using only the CaP-ENZ/DTX system at concentrations of 250, 500, 1000, and 2000 µg/mL. VCaP and LNCaP cells were seeded in 96-well plates (15000 cells per well) for 24 h, and after exposure to NPs at various concentrations for 72 h, viability was determined using PrestoBlue and LiveDead assays. Fig. 56a shows that, in comparison to the control group, the CaP-ENZ/DTX clearly exhibited cytotoxicity on VCaP and LNCaP cells. Starting from the control cells, it was possible to notice an improvement in the cell viability of the latter, both from the

PrestoBlue assay values (Fig.56a) and from the LiveDead images (Fig. 56b). This is due to the fact that by increasing the number of cells in each well, cell-cell interactions can be enhanced, leading to an improvement in cell viability. However, there remains a different behaviour between the two cell lines, as VCaPs are much more viable than LNCaPs.

There are several possible explanations for the different behaviours between LNCaP and VCaP cells when seeded in 96-well plates. For example, genetic differences between the two cell lines may affect their behaviour, including their ability to grow and survive *in vitro*. Another explanation could be linked to the phenotypic differences between the two cell lines; for example, VCaP cells express high levels of androgen receptors and exhibit a more aggressive phenotype than LNCaP cells (S. Gao et al., 2016), which could explain why under the same experimental conditions, VCaP cells are able to have better cell viability than LNCaP cells.

Furthermore, it is possible to observe that there were no statistically significant differences between the viability of the cells treated with various concentrations of NPs. This is due to the fact that the particles were not entirely soluble in DMEM, which led to an incompletely homogenous final solution and prevented the cells from being exposed to an increasing concentration of particles. It is evident that DTX and ENZ together have a cytotoxic effect on LNCaP and VCaP cells. However, it is possible that the efficacies of DTX and ENZ were different between the two cell lines. The most common androgen-dependent prostate cancer cell line, LNCaP cells, depend on androgen receptor signalling for growth and survival. By preventing androgen receptor signalling, the androgen receptor inhibitor ENZ effectively inhibits the growth of LNCaP cells. Contrarily, androgen-independent prostate cancer cell lines, VCaP cells, do not require androgen receptor signalling for growth and survival (Park et al., 2015). Since ENZ has been shown to have antitumor activity in other androgen-independent prostate cancer models, it may still be effective in VCaP cells. However, because VCaP cells have different cellular properties than LNCaP cells, ENZ's efficacy in VCaP cells might be lower than in LNCaP cells. To support this, it is possible to see that the cell viability values for VCaP and LNCaP are, on average, higher than those for LNCaP.

As with the results obtained from the PrestoBlue assays, also with the LiveDead assay (Fig.56b), there was no discernible difference between the number of live cells (green) as the particle concentration varied. In particular, it should be noted that the number of

dead cells was rather low. This might be because the dead cells were eliminated during the PBS rinsing step because they were no longer adherent to the multiwell surface.

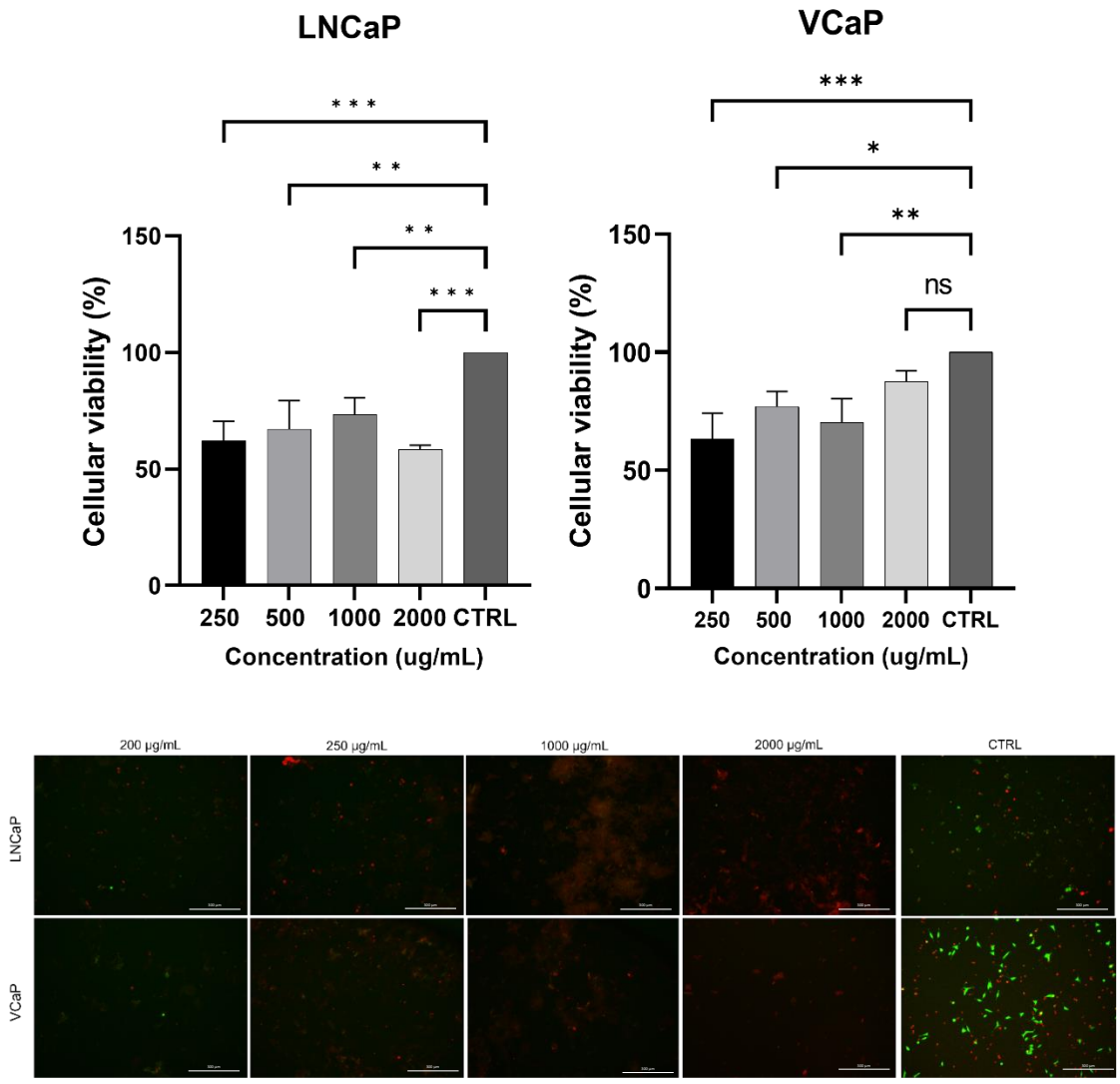

Fig. 56: (a) PrestoBlue and (b) LiveDead assay of LNCap and VCaP after 72h (Bar= 300µm).

6.2.2.5 Spheroid assembly

Because cell attachment is inhibited in U-bottom multiwells, cells can clump together and form 3D spheroids. The U-profile of the wells ensures that only one spheroid is formed per well. Two different protocols were used to obtain spheroids: the hanging drop and U-bottom methods. In Fig. 57, spheroids of LNCaP cells obtained using the hanging drop method are shown. By employing the hanging drop technique, it was possible to observe

that LNCaP cells have the propensity to aggregate and form loose cell clusters rather than clearly defined spheroids. Because their compactness and spherical geometry are fundamental characteristics, giving them *in vivo*-like tumor features that make them more reliable tools in cancer research and drug safety assessment, loose cell aggregates that are easily detached or other types of spatial aggregation cannot be considered spheroids (Leung et al., 2015).

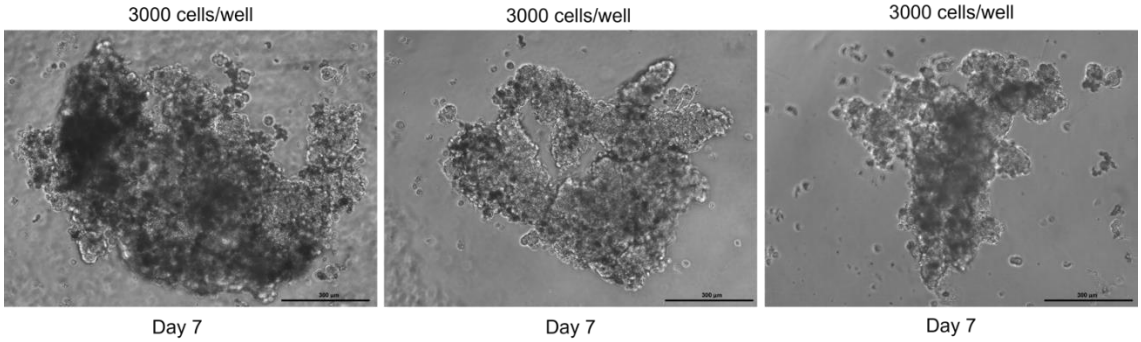

Fig. 57: LNCaP spheroids obtained using the hanging drop method after 7 days.

By changing the protocol, an attempt was made to obtain spheroids using LNCaP cells inside the wells of a multiwell U-bottom. The effect of methylcellulose on spheroid assembly was evaluated. Methylcellulose can provide a scaffold for cells to adhere to and form aggregates, as well as regulate cell-cell interactions and the diffusion of nutrients and oxygen. Several studies have demonstrated the effectiveness of methylcellulose in promoting spheroid assembly in various cell types, including cancer cells. For example, Leung et al. showed that methylcellulose can contribute to a more compact and circular spheroid morphology (Leung et al., 2015). Figure 58 shows the LNCaP cell aggregates obtained in the presence or absence of methylcellulose with the following cell density values: 1000, 1500, 2000, 5000, 10000, 25000, 50000, and 100000 cells per well. In addition, LNCaP aggregates formed only loose aggregates and not compact spheroids. It is evident that the presence of methylcellulose helps the cells aggregate more, but it is insufficient to obtain spheroids.

An attempt to obtain spheroids was also made using VCaP cells. Fig. 60 shows the results obtained in the presence and absence of methylcellulose with the following cell density values:1000, 1500, 2000, 5000, 10000, 25000, 50000, and 100000 cells per well. It can be observed that VCaP cells have a greater capacity for spheroid aggregation and formation. After monitoring the development of spheroids with cell densities of 10,000,

25,000, 50,000, and 100,000 cells per well for 16 days (Fig. 61), ImageJ software was used to calculate the final diameter, showed in Fig.59.

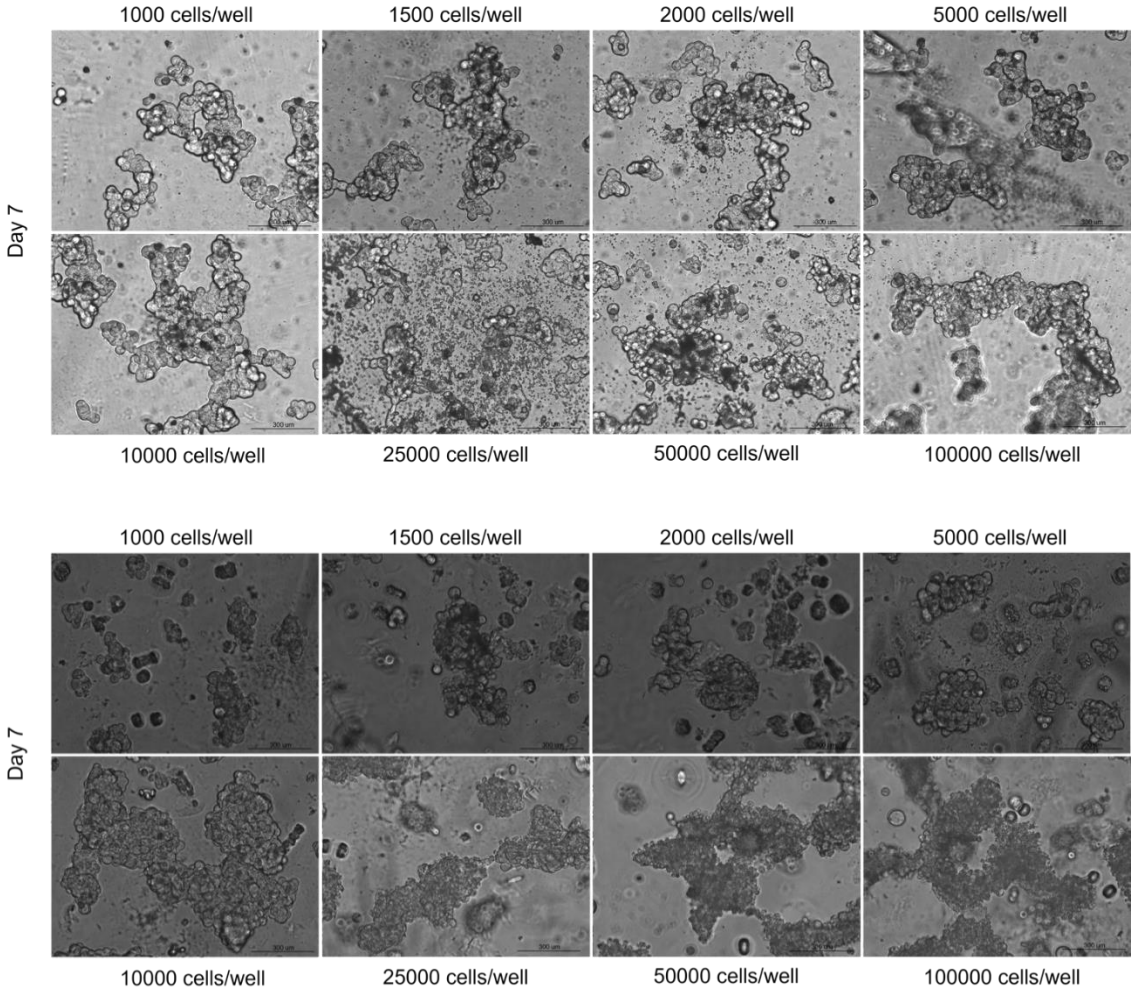

Figure 58: Spheroids obtained using LNCaP cells, with (a) and without (b) the presence of methylcellulose, after 7 days.

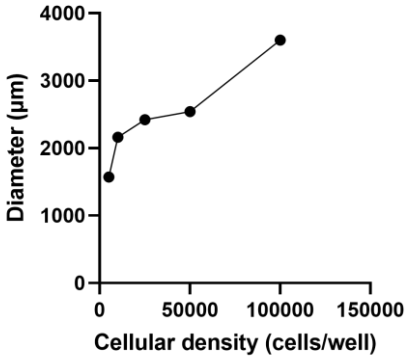

Figure 59: VCaP spheroids diameter analysed after 16 days with Image software.

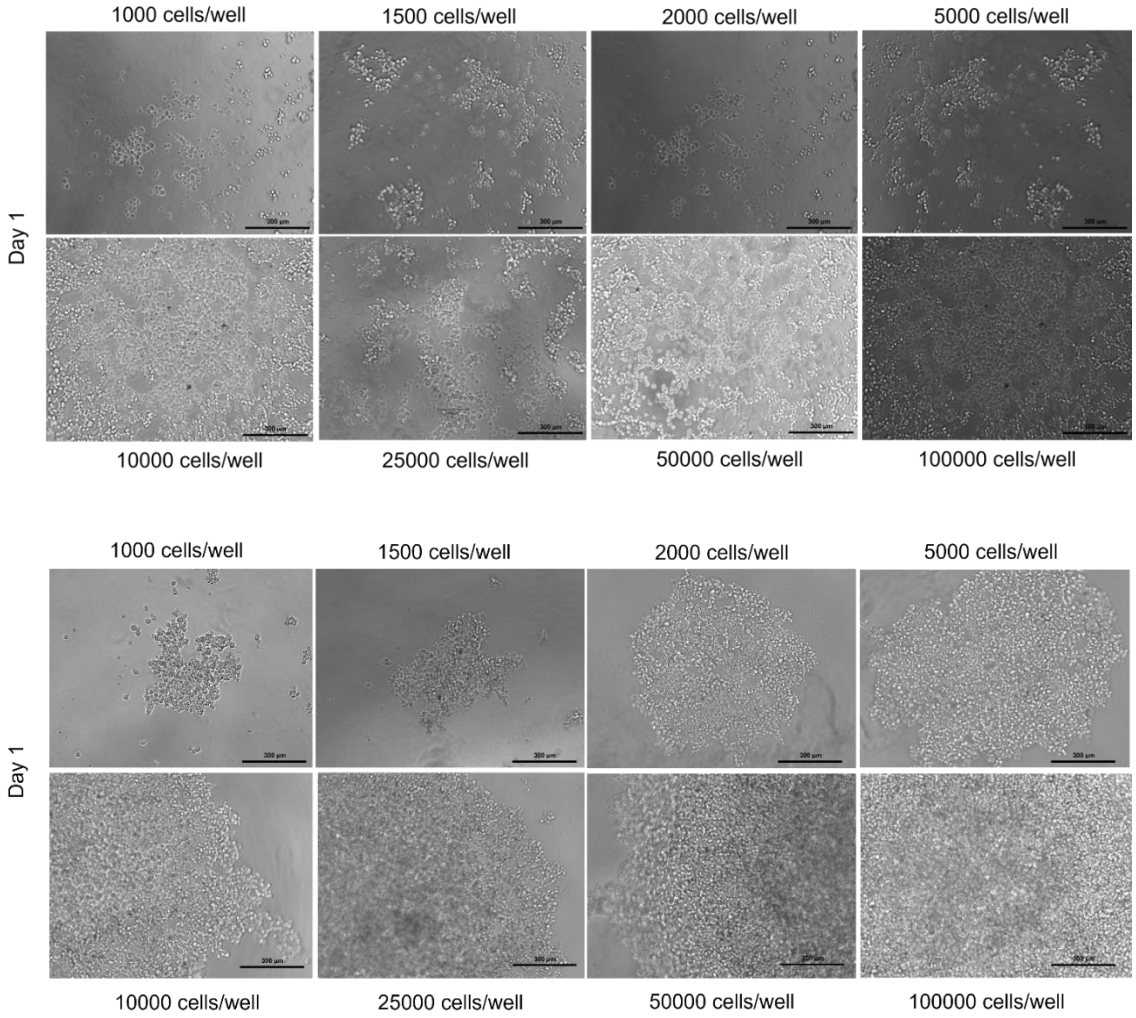

Figure 60: Spheroids obtained using VCaP cells, with (a) and without (b) the presence of methylcellulose, after 1 day.

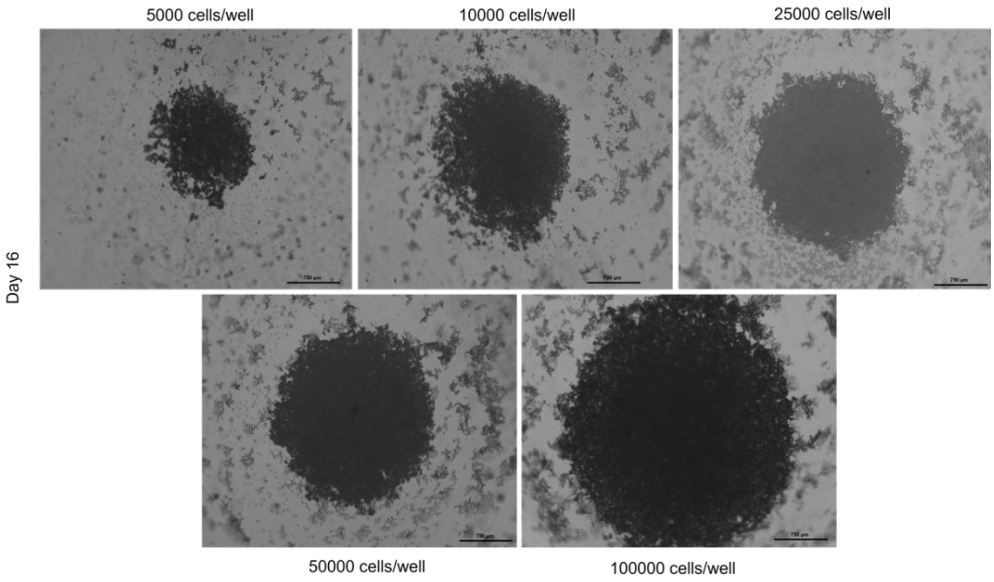

Figure 61: VCaP spheroids after 16 days.

6.2.2.6 Cytotoxicity evaluation on 3D model

To evaluate the cytotoxicity of the CaP/ENZ-DTX system in 3D models, VCaP spheroids with a cell density of 25,000 cells per well were generated. The VCaP spheroids were exposed to the particles at a concentration of 2000 ug/ml after 24 h of incubation. After 72 hours, cellular viability assays were performed.

Fig. 62 shows the values of cellular vitality. A statistically significant difference was observed between the vitality of the spheroids and that of the controls (spheroids that were not exposed to the CaP/ENZ-DTX system).

Fig. 63 shows the results of the live/dead cell assay. It is possible to see how the spheroids treated with the CaP-ENZ/DTX system differed from the control because they were no longer compact. This shows that the cells were dying and unable to communicate with each other and stay together. When drugs are tested on spheroids, some structural changes can be used to gauge the therapeutic efficacy of the treatment. Among these, changes in the shape and volume of spheroids were the primary outcomes that showed therapeutic effects. As the treatment progresses, cell-cell and cell-matrix interactions are disrupted owing to cytotoxicity. Consequently, the structure of the spheroid collapses and the spheroid is no longer compact (Han et al., 2021).

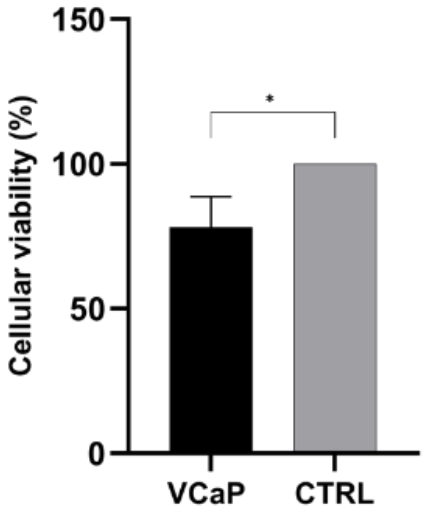

Figure 62: Cellular viability (%) of VcaP spheroids treated with CaP-ENZ/DTX.

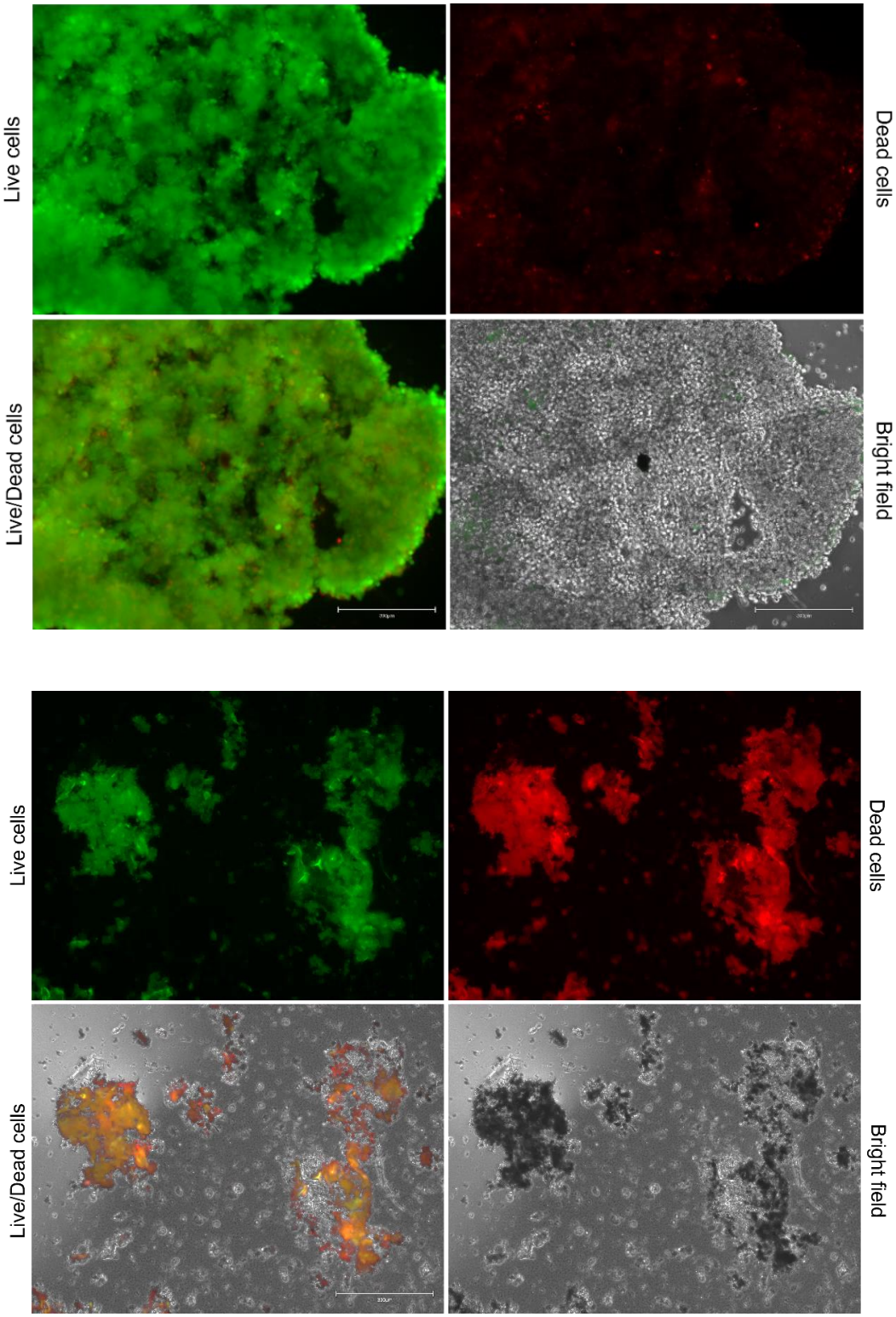

Figure 63: Live/Dead assay performed on VCaP spheroids treated with CaP-ENZ/DTX.

CONCLUSIONS

In this study, a nanotheranostic approach for prostate cancer imaging and treatment was developed. In particular, this application involves the design of PSMA-targeted DTX- and ENZ-co-loaded nanoparticles, which have been characterized in terms of their physicochemical and morphological properties. Moreover, their cytotoxic effects were assessed in two types of prostate cancer cells, LNCap and VCaP.

The designed particle was characterized by the presence of a CaP core encapsulating DTX and stabilized by the PAH coating. The encapsulation efficiency (EE%) of DTX in the CaP particle core, calculated by spectrometric analysis, was very low (7.4% ± 0.5). In general, the chemotherapeutic loading efficiency of CaP particles is not adequate for cancer chemotherapy. Therefore, efforts have been made to improve the efficacy of CaP particle encapsulation by complexing drugs with biomolecules on the particle surface rather than within it. The DTX release profile from CaP particles showed a controlled release of the drug over time, demonstrating how the CaP particles and PAH coating were able to retain the drug.

Using the layer-by-layer assembly technique, four layers of two natural polyelectrolytes, chitosan and furcellaran, with opposite charges were deposited on the CaP core via electrostatic interactions. Chitosan and furcellaran are two natural polymers that have some ideal characteristics for applications in nanocarriers for the treatment of prostate cancer (good mechanical properties, biodegradability, and biocompatibility) and have been approved by both the FDA and EMA for use in pharmaceutical applications.

In the subsequent deposition of FUR and CHI layers, two drugs, ENZ and DTX, were encapsulated. To evaluate the single and synergistic effects of the two drugs, three systems were created: in the first, no drugs were encapsulated in the layers; in the second, ENZ was encapsulated in the negative layers; and in the last system, both DTX and ENZ were encapsulated in the negative layers.

Subsequently, chitin-derived CQDs were encapsulated in the final layer of the system. These are fluorescent probes with unique optical and chemical properties that provide system-imaging properties. The main problem associated with the use of quantum dots is their toxicity, but in this case, the use of CQDs derived from chitin ensures their biocompatibility, which was evaluated by cell viability tests on fibroblasts. The results demonstrated that concentrations of CQDs of up to 50 μg/mL did not exhibit a cytotoxic effect on the cells.

Moreover, a small-molecule ligand, PSMA-617, was grafted onto the outermost layer of the system to enhance cancer cell-specific targeting, uptake, and retention.

The three different final systems were characterized by morphological and chemical-physical studies. In particular, TEM analyses have shown that the addition of drugs to the layers causes an increase in the average particle size to approximately 50 nm. The particles remained spherical in all the cases. The subsequent deposition of polyelectrolytes on the CaP particles was verified using zeta potential analysis. In all systems, the phenomenon of charge inversion was noted, obtaining values of zeta potential higher than + 20mV and lower than - 20mV. Therefore, these systems can be considered to be stable. Analysis of the FTIR spectra for the three systems highlighted the presence of the characteristic peaks of FUR and CHI in the respective layers, as well as providing proof of the correct encapsulation of DTX and ENZ. The surface chemistry of the three different particle systems was further characterized using high-resolution XPS. In the case of the first system, the XPS spectrum showed the characteristic peaks of the main elements constituting the system. In particular, the presence of sulfur and nitrogen peaks confirmed the successful deposition of FUR and CHI. Instead, the appearance of a peak associated with fluorine confirmed the encapsulation of enzalutamide in the second system. In the third system, the increase in the atomic concentrations of nitrogen and sulfur was related to the encapsulation of DTX and surface functionalization of the outermost layer with PSMA-617.

Subsequently, the cytotoxic effect of the particles was evaluated in two types of prostate cancer cells, VCaP and LNCaP. Initially, LNCaP and VCaP cells were exposed for up to 48h to the three different particle systems in concentrations from 20 to 1000 μg/mL. Cell viability was evaluated using the PrestoBlue and Live/Dead assays. The results of the cell viability tests showed no statistically significant differences between the different systems and concentrations. From the results obtained from the drug encapsulation efficiency in the layers and in the core, the absence of statistically significant differences between the different systems was mainly due to the low encapsulation efficiency of DTX and ENZ both in the layers and in the core. Therefore, subsequent cell tests were conducted only with the complete system containing both drugs. To increase the cytotoxic effect, changes were made to the composition of the system, including an increase in the concentration of encapsulated drugs and exposure of the cells to a higher concentration of particles (up to 2000 μg/mL) for a longer time (up to 72h). Cell viability results demonstrated a significant cytotoxic effect of the particles on both LNCaP and VCaP cells.

Subsequently, spheroids were generated from the LNCaP and VCaP cells to assess the efficacy of the proposed system in a biomimetic and reliable manner. However, in the case of LNCaP cells, only loose aggregates were obtained, which cannot be considered realistic models. Instead, spheroids were generated using VCaP cells and were characterized in terms of their diameter for up to 16 days. Larger diameters were obtained as the cell density of spheroids increased. In particular, for spheroids with a cell density of 100,000 cells, the final measured diameter was approximately 3600 μm.
The generated VCaP spheroids were used to test the particle system's cytotoxicity, which had previously been tested on LNCaP and VCaP cells. The particles' cytotoxic effect was demonstrated by tests on cell viability.

FUTURE PRESPECTIVES

The system used in this study could be improved in several ways. The main objective is to enhance drug encapsulation within the layers of nanoparticles, which is crucial for drug delivery research because it can increase drug efficacy and reduce adverse effects. For instance, it would be wise to conduct a more thorough assessment of the ability of the materials used in the current system to load drugs, maintain stability, and be toxic. Ultimately, it could be determined whether chitosan layers, as opposed to furcellaran layers, improve drug encapsulation efficiency. Regarding drug release, it could be determined whether altering the placement of the drugs in the various layers allows for the creation of different drug release kinetics. Additionally, it is important to assess how drugs release in environments that mimic physiological and tumour environments.

Finally, a higher particle concentration should be used in order to better understand the outcomes of spheroids. However, it is necessary to develop 3D models that include various components that characterize the tumor microenvironment (TME), stromal cells, extracellular matrix (ECM), angiogenic factors, immune cells, hypoxia, and metabolic factors tumourder to assess the effectiveness and reliability of the results.

REFERENCES

Aghebati-Maleki, A., Dolati, S., Ahmadi, M., Baghbanzhadeh, A., Asadi, M., Fotouhi, A., Yousefi, M., & Aghebati-Maleki, L. (2020). Nanoparticles and cancer therapy: Perspectives for application of nanoparticles in the treatment of cancers. *Journal of Cellular Physiology*, *235*(3), 1962–1972. https://doi.org/10.1002/jcp.29126

Alas, M. O., Alkas, F. B., Aktas Sukuroglu, A., Genc Alturk, R., & Battal, D. (2020). Fluorescent carbon dots are the new quantum dots: an overview of their potential in emerging technologies and nanosafety. *Journal of Materials Science*, *55*(31), 15074–15105. https://doi.org/10.1007/s10853-020-05054-y

Amaral, T. M. S., Macedo, D., Fernandes, I., & Costa, L. (2012). Castration-resistant prostate cancer: mechanisms, targets, and treatment. *Prostate Cancer*, *2012*, 327253. https://doi.org/10.1155/2012/327253

Ang, M. J. Y., Chan, S. Y., Goh, Y.-Y., Luo, Z., Lau, J. W., & Liu, X. (2021). Emerging strategies in developing multifunctional nanomaterials for cancer nanotheranostics. *Advanced Drug Delivery Reviews*, *178*, 113907. https://doi.org/10.1016/j.addr.2021.113907

Attia, M. F., Anton, N., Wallyn, J., Omran, Z., & Vandamme, T. F. (2019). An overview of active and passive targeting strategies to improve the nanocarriers efficiency to tumour sites. *The Journal of Pharmacy and Pharmacology*, *71*(8), 1185–1198. https://doi.org/10.1111/jphp.13098

Baig, F. A., Hamid, A., Mirza, T., & Syed, S. (2015). Ductal and Acinar Adenocarcinoma of Prostate: Morphological and Immunohistochemical Characterization. *Oman Medical Journal*, *30*(3), 162–166. https://doi.org/10.5001/omj.2015.36

Barani, M., Sabir, F., Rahdar, A., Arshad, R., & Kyzas, G. Z. (2020). Nanotreatment and Nanodiagnosis of Prostate Cancer: Recent Updates. *Nanomaterials (Basel, Switzerland)*, *10*(9). https://doi.org/10.3390/nano10091696

Becker, A. L., Orlotti, N. I., Folini, M., Cavalieri, F., Zelikin, A. N., Johnston, A. P. R., Zaffaroni, N., & Caruso, F. (2011). Redox-Active Polymer Microcapsules for the Delivery of a Survivin-Specific siRNA in Prostate Cancer Cells. *ACS Nano*, *5*(2), 1335–1344. https://doi.org/10.1021/nn103044z

Bell, K. J. L., Del Mar, C., Wright, G., Dickinson, J., & Glasziou, P. (2015). Prevalence of incidental prostate cancer: A systematic review of autopsy studies. *International Journal of Cancer*, *137*(7), 1749–1757. https://doi.org/10.1002/ijc.29538

Bertrand, N., Wu, J., Xu, X., Kamaly, N., & Farokhzad, O. C. (2014). Cancer nanotechnology: The impact of passive and active targeting in the era of modern cancer biology. *Advanced Drug Delivery Reviews*, *66*, 2–25. https://doi.org/10.1016/j.addr.2013.11.009

Bhojani, N., Capitanio, U., Suardi, N., Jeldres, C., Isbarn, H., Shariat, S. F., Graefen, M., Arjane, P., Duclos, A., Lattouf, J.-B., Saad, F., Valiquette, L., Montorsi, F., Perrotte, P., & Karakiewicz, P. I. (2010). The Rate of Secondary Malignancies After Radical Prostatectomy Versus External Beam Radiation Therapy for Localized Prostate Cancer: A Population-Based Study on 17,845 Patients. *International Journal of*

*Radiation Oncology*Biology*Physics*, *76*(2), 342–348. https://doi.org/10.1016/j.ijrobp.2009.02.011

Bruno, J. G. (2022). Advantages and Disadvantages of Using Quantum Dots in Lateral Flow and Other Biological Assay Formats. In *Application of Quantum Dots in Biology and Medicine* (pp. 91–102). Springer Nature Singapore. https://doi.org/10.1007/978-981-19-3144-4_5

Calatayud, D. G., Neophytou, S., Nicodemou, E., Giuffrida, S. G., Ge, H., & Pascu, S. I. (2022). Nano-Theranostics for the Sensing, Imaging and Therapy of Prostate Cancers. *Frontiers in Chemistry*, *10*, 830133. https://doi.org/10.3389/fchem.2022.830133

Chen, J., Hu, C., Niestroj, M., Yuan, D., & Chang, S. (2015). Treating cancer stem cells and cancer metastasis using glucose-coated gold nanoparticles. *International Journal of Nanomedicine*, 2065. https://doi.org/10.2147/IJN.S72144

Choksi, A. U., Khan, A. I., Lokeshwar, S. D., Segal, D., Weiss, R. M., & Martin, D. T. (2022). Functionalized nanoparticles targeting biomarkers for prostate cancer imaging and therapy. *American Journal of Clinical and Experimental Urology*, *10*(3), 142–153.

da Rocha, M. C. O., da Silva, P. B., Radicchi, M. A., Andrade, B. Y. G., de Oliveira, J. V., Venus, T., Merker, C., Estrela-Lopis, I., Longo, J. P. F., & Báo, S. N. (2020). Docetaxel-loaded solid lipid nanoparticles prevent tumor growth and lung metastasis of 4T1 murine mammary carcinoma cells. *Journal of Nanobiotechnology*, *18*(1), 43. https://doi.org/10.1186/s12951-020-00604-7

Danhier, F., Feron, O., & Préat, V. (2010). To exploit the tumor microenvironment: Passive and active tumor targeting of nanocarriers for anti-cancer drug delivery. *Journal of Controlled Release : Official Journal of the Controlled Release Society*, *148*(2), 135–146. https://doi.org/10.1016/j.jconrel.2010.08.027

De Marzo, A. M., Haffner, M. C., Lotan, T. L., Yegnasubramanian, S., & Nelson, W. G. (2016). Premalignancy in Prostate Cancer: Rethinking What We Know. *Cancer Prevention Research*, *9*(8), 648–656. https://doi.org/10.1158/1940-6207.CAPR-15-0431

de Villiers, M. M., Otto, D. P., Strydom, S. J., & Lvov, Y. M. (2011). Introduction to nanocoatings produced by layer-by-layer (LbL) self-assembly. *Advanced Drug Delivery Reviews*, *63*(9), 701–715. https://doi.org/10.1016/j.addr.2011.05.011

Desmond, L. J., Phan, A. N., & Gentile, P. (2021). Critical overview on the green synthesis of carbon quantum dots and their application for cancer therapy. *Environmental Science: Nano*, *8*(4), 848–862. https://doi.org/10.1039/D1EN00017A

Devi, P., Saini, S., & Kim, K.-H. (2019). The advanced role of carbon quantum dots in nanomedical applications. *Biosensors and Bioelectronics*, *141*, 111158. https://doi.org/10.1016/j.bios.2019.02.059

Dhar, S., Gu, F. X., Langer, R., Farokhzad, O. C., & Lippard, S. J. (2008). Targeted delivery of cisplatin to prostate cancer cells by aptamer functionalized Pt(IV) prodrug-PLGA–PEG nanoparticles. *Proceedings of the National Academy of Sciences*, *105*(45), 17356–17361. https://doi.org/10.1073/pnas.0809154105

Dube, N., Shu, J. Y., Dong, H., Seo, J. W., Ingham, E., Kheirolomoom, A., Chen, P.-Y., Forsayeth, J., Bankiewicz, K., Ferrara, K. W., & Xu, T. (2013). Evaluation of Doxorubicin-Loaded 3-Helix Micelles as Nanocarriers. *Biomacromolecules*, *14*(10), 3697–3705. https://doi.org/10.1021/bm4010518

Farzin, M. A., & Abdoos, H. (2021). A critical review on quantum dots: From synthesis toward applications in electrochemical biosensors for determination of disease-related biomolecules. *Talanta*, *224*, 121828. https://doi.org/10.1016/j.talanta.2020.121828

Freitas, L. F., Ferreira, A. H., Thipe, V. C., Varca, G. H. C., Lima, C. S. A., Batista, J. G. S., Riello, F. N., Nogueira, K., Cruz, C. P. C., Mendes, G. O. A., Rodrigues, A. S., Sousa, T. S., Alves, V. M., & Lugão, A. B. (2021a). The State of the Art of Theranostic Nanomaterials for Lung, Breast, and Prostate Cancers. *Nanomaterials (Basel, Switzerland)*, *11*(10). https://doi.org/10.3390/nano11102579

Freitas, L. F., Ferreira, A. H., Thipe, V. C., Varca, G. H. C., Lima, C. S. A., Batista, J. G. S., Riello, F. N., Nogueira, K., Cruz, C. P. C., Mendes, G. O. A., Rodrigues, A. S., Sousa, T. S., Alves, V. M., & Lugão, A. B. (2021b). The State of the Art of Theranostic Nanomaterials for Lung, Breast, and Prostate Cancers. *Nanomaterials (Basel, Switzerland)*, *11*(10). https://doi.org/10.3390/nano11102579

Galsky, M. D., & Vogelzang, N. J. (2010). Docetaxel-based combination therapy for castration-resistant prostate cancer. *Annals of Oncology*, *21*(11), 2135–2144. https://doi.org/10.1093/annonc/mdq050

Gandaglia, G., Leni, R., Bray, F., Fleshner, N., Freedland, S. J., Kibel, A., Stattin, P., Van Poppel, H., & La Vecchia, C. (2021). Epidemiology and Prevention of Prostate Cancer. *European Urology Oncology*, *4*(6), 877–892. https://doi.org/10.1016/j.euo.2021.09.006

Gao, S., Gao, Y., He, H. H., Han, D., Han, W., Avery, A., Macoska, J. A., Liu, X., Chen, S., Ma, F., Chen, S., Balk, S. P., & Cai, C. (2016). Androgen Receptor Tumor Suppressor Function Is Mediated by Recruitment of Retinoblastoma Protein. *Cell Reports*, *17*(4), 966–976. https://doi.org/10.1016/j.celrep.2016.09.064

Gao, Y., Gao, D., Shen, J., & Wang, Q. (2020). A Review of Mesoporous Silica Nanoparticle Delivery Systems in Chemo-Based Combination Cancer Therapies. *Frontiers in Chemistry*, *8*. https://doi.org/10.3389/fchem.2020.598722

Gavas, S., Quazi, S., & Karpiński, T. M. (2021a). Nanoparticles for Cancer Therapy: Current Progress and Challenges. *Nanoscale Research Letters*, *16*(1), 173. https://doi.org/10.1186/s11671-021-03628-6

Gavas, S., Quazi, S., & Karpiński, T. M. (2021b). Nanoparticles for Cancer Therapy: Current Progress and Challenges. *Nanoscale Research Letters*, *16*(1), 173. https://doi.org/10.1186/s11671-021-03628-6

Gidwani, B., Sahu, V., Shukla, S. S., Pandey, R., Joshi, V., Jain, V. K., & Vyas, A. (2021). Quantum dots: Prospectives, toxicity, advances and applications. *Journal of Drug Delivery Science and Technology*, *61*, 102308. https://doi.org/10.1016/j.jddst.2020.102308

Gomes, M. F., Gomes, Y. F., Lopes-Moriyama, A., de Barros Neto, E. L., & de Souza, C. P. (2019). Design of carbon quantum dots via hydrothermal carbonization

synthesis from renewable precursors. *Biomass Conversion and Biorefinery*, *9*(4), 689–694. https://doi.org/10.1007/s13399-019-00387-4

Greene, D. R., Fitzpatrick, J. M., & Scardino, P. T. (1995). Anatomy of the prostate and distribution of early prostate cancer. *Seminars in Surgical Oncology*, *11*(1), 9–22. https://doi.org/10.1002/ssu.2980110104

Gu, C., Li, C., Zhang, J., Li, X., Wang, L., Ju, Y., Liu, Y., & Xu, Y. (2020). Ultra-effective near-infrared Photothermal therapy for the prostate cancer Nursing care through novel intended and surface tailored photo-responsive Ga-Au@MPS nanovesicles. *Journal of Photochemistry and Photobiology B: Biology*, *202*, 111685. https://doi.org/10.1016/j.jphotobiol.2019.111685

Han, S. J., Kwon, S., & Kim, K. S. (2021). Challenges of applying multicellular tumor spheroids in preclinical phase. *Cancer Cell International*, *21*(1), 152. https://doi.org/10.1186/s12935-021-01853-8

He, L., Liu, J., Li, S., Feng, X., Wang, C., Zhuang, X., Ding, J., & Chen, X. (2019). Polymer Nanoplatforms at Work in Prostate Cancer Therapy. *Advanced Therapeutics*, *2*(4), 1800122. https://doi.org/10.1002/adtp.201800122

Ho, J. A., Wang, L.-S., & Chuang, M.-C. (2012). Nanotheranostics – a review of recent publications. *International Journal of Nanomedicine*, 4679. https://doi.org/10.2147/IJN.S33065

Huang, D., He, B., & Mi, P. (2019). Calcium phosphate nanocarriers for drug delivery to tumors: imaging, therapy and theranostics. *Biomaterials Science*, *7*(10), 3942–3960. https://doi.org/10.1039/C9BM00831D

Hull, G. W., Rabbani, F., Abbas, F., Wheeler, T. M., Kattan, M. W., & Scardino, P. T. (2002). Cancer control with radical prostatectomy alone in 1,000 consecutive patients. *The Journal of Urology*, *167*(2 Pt 1), 528–534. https://doi.org/10.1016/S0022-5347(01)69079-7

Jamróz, E., Para, G., Jachimska, B., Szczepanowicz, K., Warszyński, P., & Para, A. (2014). Albumin–furcellaran complexes as cores for nanoencapsulation. *Colloids and Surfaces A: Physicochemical and Engineering Aspects*, *441*, 880–884. https://doi.org/10.1016/j.colsurfa.2013.01.002

Janus, Ł., Piątkowski, M., Radwan-Pragłowska, J., Bogdał, D., & Matysek, D. (2019). Chitosan-Based Carbon Quantum Dots for Biomedical Applications: Synthesis and Characterization. *Nanomaterials*, *9*(2), 274. https://doi.org/10.3390/nano9020274

Janus, Ł., Radwan-Pragłowska, J., Piątkowski, M., & Bogdał, D. (2020). Facile Synthesis of Surface-Modified Carbon Quantum Dots (CQDs) for Biosensing and Bioimaging. *Materials*, *13*(15), 3313. https://doi.org/10.3390/ma13153313

Kalyane, D., Raval, N., Maheshwari, R., Tambe, V., Kalia, K., & Tekade, R. K. (2019). Employment of enhanced permeability and retention effect (EPR): Nanoparticle-based precision tools for targeting of therapeutic and diagnostic agent in cancer. *Materials Science and Engineering: C*, *98*, 1252–1276. https://doi.org/10.1016/j.msec.2019.01.066

Kenfield, S. A., Van Blarigan, E. L., DuPre, N., Stampfer, M. J., L. Giovannucci, E., & Chan, J. M. (2014). Selenium Supplementation and Prostate Cancer Mortality. *JNCI*

Journal of the National Cancer Institute, *107*(1), dju360–dju360. https://doi.org/10.1093/jnci/dju360

Khan, S., & Hossain, M. K. (2022). Classification and properties of nanoparticles. In *Nanoparticle-Based Polymer Composites* (pp. 15–54). Elsevier. https://doi.org/10.1016/B978-0-12-824272-8.00009-9

Khramtsov, P., Kropaneva, M., Bochkova, M., Timganova, V., Zamorina, S., & Rayev, M. (2019). Solid-phase nuclear magnetic resonance immunoassay for the prostate-specific antigen by using protein-coated magnetic nanoparticles. *Microchimica Acta*, *186*(12), 768. https://doi.org/10.1007/s00604-019-3925-4

Kundu, P., Singh, D., Singh, A., & Sahoo, S. K. (2020). Cancer Nanotheranostics: A Nanomedicinal Approach for Cancer Therapy and Diagnosis. *Anti-Cancer Agents in Medicinal Chemistry*, *20*(11), 1288–1299. https://doi.org/10.2174/1871520619666190820145930

Kurczewska, J. (2022). Recent Reports on Polysaccharide-Based Materials for Drug Delivery. *Polymers*, *14*(19), 4189. https://doi.org/10.3390/polym14194189

Laos, K., & Ring, S. G. (2005). Note: Characterisation of furcellaran samples from Estonian Furcellaria lumbricalis (Rhodophyta). *Journal of Applied Phycology*, *17*(5), 461–464. https://doi.org/10.1007/s10811-005-1635-2

Leung, B. M., Lesher-Perez, S. C., Matsuoka, T., Moraes, C., & Takayama, S. (2015). Media additives to promote spheroid circularity and compactness in hanging drop platform. *Biomaterials Science*, *3*(2), 336–344. https://doi.org/10.1039/C4BM00319E

Levy, O., Brennen, W. N., Han, E., Rosen, D. M., Musabeyezu, J., Safaee, H., Ranganath, S., Ngai, J., Heinelt, M., Milton, Y., Wang, H., Bhagchandani, S. H., Joshi, N., Bhowmick, N., Denmeade, S. R., Isaacs, J. T., & Karp, J. M. (2016). A prodrug-doped cellular Trojan Horse for the potential treatment of prostate cancer. *Biomaterials*, *91*, 140–150. https://doi.org/10.1016/j.biomaterials.2016.03.023

Lim Ng, K. (2021). The Etiology of Prostate Cancer. In *Prostate Cancer* (pp. 17–28). Exon Publications. https://doi.org/10.36255/exonpublications.prostatecancer.etiology.2021

Lin, L. Y. (2016). Quantum Dot Nanophotonic Integrated Circuits. In *Encyclopedia of Nanotechnology* (pp. 3389–3399). Springer Netherlands. https://doi.org/10.1007/978-94-017-9780-1_193

Marangoni Júnior, L., Vieira, R. P., Jamróz, E., & Anjos, C. A. R. (2021). Furcellaran: An innovative biopolymer in the production of films and coatings. *Carbohydrate Polymers*, *252*, 117221. https://doi.org/10.1016/j.carbpol.2020.117221

McAninch, J. W., & Lue, T. F. (2020). *Smith & Tanagho's General Urology* (19e ed.). McGraw Hill.

McNeal, J. E. (1984). Anatomy of the prostate and morphogenesis of BPH. *Progress in Clinical and Biological Research*, *145*, 27–53.

Meng, W., Bai, X., Wang, B., Liu, Z., Lu, S., & Yang, B. (2019). Biomass-Derived Carbon Dots and Their Applications. *ENERGY & ENVIRONMENTAL MATERIALS*, *2*(3), 172–192. https://doi.org/10.1002/eem2.12038

Milosavljevic, V., Jamroz, E., Gagic, M., Haddad, Y., Michalkova, H., Balkova, R., Tesarova, B., Moulick, A., Heger, Z., Richtera, L., Kopel, P., & Adam, V. (2020). Encapsulation of Doxorubicin in Furcellaran/Chitosan Nanocapsules by Layer-by-Layer Technique for Selectively Controlled Drug Delivery. *Biomacromolecules*, *21*(2), 418–434. https://doi.org/10.1021/acs.biomac.9b01175

Mohler, J. L., Antonarakis, E. S., Armstrong, A. J., D'Amico, A. V., Davis, B. J., Dorff, T., Eastham, J. A., Enke, C. A., Farrington, T. A., Higano, C. S., Horwitz, E. M., Hurwitz, M., Ippolito, J. E., Kane, C. J., Kuettel, M. R., Lang, J. M., McKenney, J., Netto, G., Penson, D. F., … Freedman-Cass, D. A. (2019). Prostate Cancer, Version 2.2019, NCCN Clinical Practice Guidelines in Oncology. *Journal of the National Comprehensive Cancer Network*, *17*(5), 479–505. https://doi.org/10.6004/jnccn.2019.0023

Murray, T. B. J. (2021). The Pathogenesis of Prostate Cancer. In *Prostate Cancer* (pp. 29–42). Exon Publications. https://doi.org/10.36255/exonpublications.prostatecancer.pathogenesis.2021

Naik, K., Chaudhary, S., Ye, L., & Parmar, A. S. (2022). A Strategic Review on Carbon Quantum Dots for Cancer-Diagnostics and Treatment. *Frontiers in Bioengineering and Biotechnology*, *10*, 882100. https://doi.org/10.3389/fbioe.2022.882100

Nangare, S. N., Patil, P. O., Tade, R. S., Patil, A. G., Deshmukh, P. K., Pandey, A., Khan, Z. G., Mutalik, S., Jadhav, N. R., Patel, J. K., More, M. P., & Bari, S. B. (2022). *Polymeric Nanoplatforms for the Targeted Treatment of Prostate Cancer* (pp. 427–471). https://doi.org/10.1007/978-3-031-14848-4_16

Narayanan, N. K., Nargi, D., Randolph, C., & Narayanan, B. A. (2009). Liposome encapsulation of curcumin and resveratrol in combination reduces prostate cancer incidence in PTEN knockout mice. *International Journal of Cancer*, *125*(1), 1–8. https://doi.org/10.1002/ijc.24336

Nuhn, P., De Bono, J. S., Fizazi, K., Freedland, S. J., Grilli, M., Kantoff, P. W., Sonpavde, G., Sternberg, C. N., Yegnasubramanian, S., & Antonarakis, E. S. (2019). Update on Systemic Prostate Cancer Therapies: Management of Metastatic Castration-resistant Prostate Cancer in the Era of Precision Oncology. *European Urology*, *75*(1), 88–99. https://doi.org/10.1016/j.eururo.2018.03.028

Park, E., Kim, E. K., Kim, M., Ha, J. M., Kim, Y. W., Jin, S. Y., Shin, H. K., Ha, H. K., Lee, J. Z., & Bae, S. S. (2015). Androgen Receptor-dependent Expression of Low-density Lipoprotein Receptor-related Protein 6 is Necessary for Prostate Cancer Cell Proliferation. *The Korean Journal of Physiology & Pharmacology*, *19*(3), 235. https://doi.org/10.4196/kjpp.2015.19.3.235

Parveen, S., & Sahoo, S. K. (2008). Polymeric nanoparticles for cancer therapy. *Journal of Drug Targeting*, *16*(2), 108–123. https://doi.org/10.1080/10611860701794353

Pearce, A. K., & O'Reilly, R. K. (2019). Insights into Active Targeting of Nanoparticles in Drug Delivery: Advances in Clinical Studies and Design Considerations for Cancer

Nanomedicine. *Bioconjugate Chemistry*, *30*(9), 2300–2311. https://doi.org/10.1021/acs.bioconjchem.9b00456

Peng, Z.-H., & Kopeček, J. (2015). Enhancing Accumulation and Penetration of HPMA Copolymer-Doxorubicin Conjugates in 2D and 3D Prostate Cancer Cells via iRGD Conjugation with an MMP-2 Cleavable Spacer. *Journal of the American Chemical Society*, *137*(21), 6726–6729. https://doi.org/10.1021/jacs.5b00922

Pericleous, P., Gazouli, M., Lyberopoulou, A., Rizos, S., Nikiteas, N., & Efstathopoulos, E. P. (2012). Quantum dots hold promise for early cancer imaging and detection. *International Journal of Cancer*, *131*(3), 519–528. https://doi.org/10.1002/ijc.27528

“Rajal B. Shah,” & “Ming Zhou.” (2019). *Prostate Biopsy Interpretation, An Illustrated Guide* (2end ed, Vol. 1).

Rawla, P. (2019). Epidemiology of Prostate Cancer. *World Journal of Oncology*, *10*(2), 63–89. https://doi.org/10.14740/wjon1191

Richardson, J. J., Cui, J., Björnmalm, M., Braunger, J. A., Ejima, H., & Caruso, F. (2016). Innovation in Layer-by-Layer Assembly. *Chemical Reviews*, *116*(23), 14828–14867. https://doi.org/10.1021/acs.chemrev.6b00627

Ridgway, A. J., & Aning, J. J. (2021). Role of primary care in the management of prostate cancer. *Prescriber*, *32*(2), 11–17. https://doi.org/10.1002/psb.1892

Rivera, M. C., Pinheiro, A. C., Bourbon, A. I., Cerqueira, M. A., & Vicente, A. A. (2015). Hollow chitosan/alginate nanocapsules for bioactive compound delivery. *International Journal of Biological Macromolecules*, *79*, 95–102. https://doi.org/10.1016/j.ijbiomac.2015.03.003

Rizzo, M. (2021). Mechanisms of docetaxel resistance in prostate cancer: The key role played by miRNAs. *Biochimica et Biophysica Acta (BBA) - Reviews on Cancer*, *1875*(1), 188481. https://doi.org/10.1016/j.bbcan.2020.188481

Roy Chowdhury, M., Schumann, C., Bhakta-Guha, D., & Guha, G. (2016). Cancer nanotheranostics: Strategies, promises and impediments. *Biomedicine & Pharmacotherapy = Biomedecine & Pharmacotherapie*, *84*, 291–304. https://doi.org/10.1016/j.biopha.2016.09.035

Salma, K., Borodajenko, N., Plata, A., Berzina-Cimdina, L., & Stunda, A. (2008). *Fourier Transform Infrared Spectra of Technologically Modified Calcium Phosphates* (pp. 68–71). https://doi.org/10.1007/978-3-540-69367-3_19

Sanna, V., Roggio, A. M., Posadino, A. M., Cossu, A., Marceddu, S., Mariani, A., Alzari, V., Uzzau, S., Pintus, G., & Sechi, M. (2011). Novel docetaxel-loaded nanoparticles based on poly(lactide-co-caprolactone) and poly(lactide-co-glycolide-co-caprolactone) for prostate cancer treatment: formulation, characterization, and cytotoxicity studies. *Nanoscale Research Letters*, *6*(1), 260. https://doi.org/10.1186/1556-276X-6-260

Sarkar, S., & Das, S. (2016). A Review of Imaging Methods for Prostate Cancer Detection. *Biomedical Engineering and Computational Biology*, *7s1*, BECB.S34255. https://doi.org/10.4137/BECB.S34255

Schatten, H. (Ed.). (2018). *Cell & Molecular Biology of Prostate Cancer* (Vol. 1095). Springer International Publishing. https://doi.org/10.1007/978-3-319-95693-0

Schiavina, R., Chessa, F., Borghesi, M., Gaudiano, C., Bianchi, L., Corcioni, B., Castellucci, P., Ceci, F., Ceravolo, I., Barchetti, G., Del Monte, M., Campa, R., Catalano, C., Panebianco, V., Nanni, C., Fanti, S., Minervini, A., Porreca, A., & Brunocilla, E. (2019). State-of-the-art imaging techniques in the management of preoperative staging and re-staging of prostate cancer. *International Journal of Urology*, *26*(1), 18–30. https://doi.org/10.1111/iju.13797

Siemann, D. W. (2011). The unique characteristics of tumor vasculature and preclinical evidence for its selective disruption by Tumor-Vascular Disrupting Agents. *Cancer Treatment Reviews*, *37*(1), 63–74. https://doi.org/10.1016/j.ctrv.2010.05.001

Sohail, M. F., Rehman, M., Sarwar, H. S., Naveed, S., Qureshi, O. S., Bukhari, N. I., Hussain, I., Webster, T. J., & Shahnaz, G. (2018). Advancements in the oral delivery of Docetaxel: challenges, current state-of-the-art and future trends. *International Journal of Nanomedicine*, *Volume 13*, 3145–3161. https://doi.org/10.2147/IJN.S164518

Taitt, H. E. (2018). Global Trends and Prostate Cancer: A Review of Incidence, Detection, and Mortality as Influenced by Race, Ethnicity, and Geographic Location. *American Journal of Men's Health*, *12*(6), 1807–1823. https://doi.org/10.1177/1557988318798279

Taneja, S. S. (2020). Re: Gold Nanoshell-Localized Photothermal Ablation of Prostate Tumors in a Clinical Pilot Device Study. *Journal of Urology*, *203*(1), 31–31. https://doi.org/10.1097/JU.0000000000000614

Tejwan, N., Saha, S. K., & Das, J. (2020). Multifaceted applications of green carbon dots synthesized from renewable sources. *Advances in Colloid and Interface Science*, *275*, 102046. https://doi.org/10.1016/j.cis.2019.102046

Thangapazham, R., Puri, A., Tele, S., Blumenthal, R., & Maheshwari, R. (2008). Evaluation of a nanotechnology-based carrier for delivery of curcumin in prostate cancer cells. *International Journal of Oncology*. https://doi.org/10.3892/ijo.32.5.1119

Trofimov, A., Ivanova, A., Zyuzin, M., & Timin, A. (2018). Porous Inorganic Carriers Based on Silica, Calcium Carbonate and Calcium Phosphate for Controlled/Modulated Drug Delivery: Fresh Outlook and Future Perspectives. *Pharmaceutics*, *10*(4), 167. https://doi.org/10.3390/pharmaceutics10040167

Unsoy, G., Khodadust, R., Yalcin, S., Mutlu, P., & Gunduz, U. (2014). Synthesis of Doxorubicin loaded magnetic chitosan nanoparticles for pH responsive targeted drug delivery. *European Journal of Pharmaceutical Sciences*, *62*, 243–250. https://doi.org/10.1016/j.ejps.2014.05.021

Vargas, H. A., Akin, O., Franiel, T., Goldman, D. A., Udo, K., Touijer, K. A., Reuter, V. E., & Hricak, H. (2012). Normal central zone of the prostate and central zone involvement by prostate cancer: clinical and MR imaging implications. *Radiology*, *262*(3), 894–902. https://doi.org/10.1148/radiol.11110663

Vernooij, R. W., Lancee, M., Cleves, A., Dahm, P., Bangma, C. H., & Aben, K. K. (2020). Radical prostatectomy versus deferred treatment for localised prostate cancer.

Cochrane Database of Systematic Reviews, *2020*(6). https://doi.org/10.1002/14651858.CD006590.pub3

Wang, L., Lu, B., He, M., Wang, Y., Wang, Z., & Du, L. (2022). Prostate Cancer Incidence and Mortality: Global Status and Temporal Trends in 89 Countries From 2000 to 2019. *Frontiers in Public Health*, *10*. https://doi.org/10.3389/fpubh.2022.811044

Wang, Y., Sun, J., He, B., & Feng, M. (2020). Synthesis and modification of biomass derived carbon dots in ionic liquids and their application: A mini review. *Green Chemical Engineering*, *1*(2), 94–108. https://doi.org/10.1016/j.gce.2020.09.010

Wareing, T. C., Gentile, P., & Phan, A. N. (2021). Biomass-Based Carbon Dots: Current Development and Future Perspectives. *ACS Nano*, *15*(10), 15471–15501. https://doi.org/10.1021/acsnano.1c03886

Xiao, F.-X., Pagliaro, M., Xu, Y.-J., & Liu, B. (2016). Layer-by-layer assembly of versatile nanoarchitectures with diverse dimensionality: a new perspective for rational construction of multilayer assemblies. *Chemical Society Reviews*, *45*(11), 3088–3121. https://doi.org/10.1039/C5CS00781J

Yan, J., Wang, Y., Jia, Y., Liu, S., Tian, C., Pan, W., Liu, X., & Wang, H. (2017). Co-delivery of docetaxel and curcumin prodrug via dual-targeted nanoparticles with synergistic antitumor activity against prostate cancer. *Biomedicine & Pharmacotherapy*, *88*, 374–383. https://doi.org/10.1016/j.biopha.2016.12.138

Yao, Y., Zhou, Y., Liu, L., Xu, Y., Chen, Q., Wang, Y., Wu, S., Deng, Y., Zhang, J., & Shao, A. (2020a). Nanoparticle-Based Drug Delivery in Cancer Therapy and Its Role in Overcoming Drug Resistance. *Frontiers in Molecular Biosciences*, *7*. https://doi.org/10.3389/fmolb.2020.00193

Yao, Y., Zhou, Y., Liu, L., Xu, Y., Chen, Q., Wang, Y., Wu, S., Deng, Y., Zhang, J., & Shao, A. (2020b). Nanoparticle-Based Drug Delivery in Cancer Therapy and Its Role in Overcoming Drug Resistance. *Frontiers in Molecular Biosciences*, *7*. https://doi.org/10.3389/fmolb.2020.00193

Zhang, H., Yee, D., & Wang, C. (2008). Quantum dots for cancer diagnosis and therapy: biological and clinical perspectives. *Nanomedicine*, *3*(1), 83–91. https://doi.org/10.2217/17435889.3.1.83

Zhang, X., Liang, T., & Ma, Q. (2021). Layer-by-Layer assembled nano-drug delivery systems for cancer treatment. *Drug Delivery*, *28*(1), 655–669. https://doi.org/10.1080/10717544.2021.1905748

Zhang, X., Xing, J. Z., Chen, J., Ko, L., Amanie, J., Gulavita, S., Pervez, N., Yee, D., Moore, R., & Roa, W. (2008). Enhanced radiation sensitivity in prostate cancer by gold-nanoparticles. *Clinical & Investigative Medicine*, *31*(3), 160. https://doi.org/10.25011/cim.v31i3.3473

Zhou, J., Rao, L., Yu, G., Cook, T. R., Chen, X., & Huang, F. (2021). Supramolecular cancer nanotheranostics. *Chemical Society Reviews*, *50*(4), 2839–2891. https://doi.org/10.1039/D0CS00011F

WEBSITES

http://www.cancerresearchuk.org/about-cancer/prostate-cancer/types-grades.

https://prostatecanceruk.org/prostate-information/further-help/rare-prostate-cancer.

http://www.cancerresearchuk.org/about-cancer/soft-tissue-sarcoma/about.

https://www.crs-src.ca/page.aspx?pid=1801. Accessed August 12, 2017.

https://www.cancer.gov/types/prostate/prostate-hormone-therapy-fact sheet#:~:text=LHRH%20agonists%2C%20like%20the%20body's,not%20stimulated%20to%20produce%20androgens

https://www.atcc.org/products/crl-2876

https://www.cdc.gov/cancer/prostate/basic_info/what-is-prostate-cancer.htm

https://www.urologymatch.com/node/2638

http://www.cancerresearchuk.org/about-cancer/carcinoid/about